

In presenting this thesis in partial fulfillment of the requirements for an advanced degree at Idaho State University, I agree that the Library shall make it freely available for inspection. I further state that permission to download and/or print my thesis for scholarly purposes may be granted by the Dean of the Graduate School, Dean of my academic division, or by the University Librarian. It is understood that any copying or publication of this thesis for financial gain shall not be allowed without my written permission.

Signature \_\_\_\_\_

Date \_\_\_\_\_

CRETACEOUS RETROARC UNDERTHRUSTING BENEATH THE COAST  
MOUNTAINS BATHOLITH: BRITISH COLUMBIA

by

Douglas Robert MacLeod

A thesis

submitted in partial fulfillment

of the requirements for the degree of

Master of Science in the Department of Geosciences

Idaho State University

Spring 2015

## **Committee Approval**

To the Graduate Faculty:

The members of the committee appointed to examine the thesis of DOUGLAS ROBERT MACLEOD find it satisfactory and recommend that it be accepted.

---

David Pearson  
Major Advisor

---

Michael McCurry  
Committee Member

---

Ann Gironella,  
Graduate Faculty Representative

## **Acknowledgements**

I would like to thank Dr. David Pearson for his excellent guidance and assistance during all portions of this project. I would also like to thank Dr. Michael McCurry for his guidance on thin section interpretations and ideas for partial melting and metamorphic textures, and also Dr. Ann Gironella for helping get my mind around the mathematics and statistics of data analysis.

I would also like to thank my fellow graduate students for assisting in the development of ideas and assisting with laboratory methods. Also John Whiting and Amie Staley for keeping me grounded with some much needed humanity.

Special thanks to NSF-EAR 1338583 for support of the Arizona LaserChron Center, and to those at Arizona who were instrumental at providing assistance for our geochronology results.

Idaho State University and the Department of Geosciences for their help and for allowing me this opportunity.

## Table of Contents:

Table of Figures: .....	vii
Abstract .....	viii
1. Introduction .....	1
2. Geologic Background .....	3
2.1. Mesozoic Tectonic Setting .....	3
2.3. CGC structure and exhumation: .....	5
2.4. Lluvia Peak Area: .....	6
3. Methods .....	8
4. Results .....	9
4.1. Rock units .....	9
4.1.2. Gray gneiss .....	9
4.1.1. Rusty gneiss .....	10
4.1.3. Lluvia Peak pluton .....	11
4.2. Structural geology .....	12
4.2.1. Outcrop scale observations .....	12
4.2.2. Recumbent folding .....	15
4.2.3. Grain-scale crystal-plastic deformation mechanisms .....	16
4.2.4. Overprinting brittle deformation .....	17
4.3. U-Th-Pb zircon geochronology .....	18
4.3.1 Igneous geochronology: .....	18
4.3.2 Sedimentary geochronology: .....	19
5. Discussion .....	21
5.1. History and structural evolution of the field area .....	21
5.1.1. Deposition and protolith constraints .....	21
5.1.2. Structural history and magmatism .....	22
5.1.3. Exhumation .....	26
5.2. Hazelton protolith interpretation .....	27
5.3. Tectonic model .....	29
6. Conclusions .....	33
7. References .....	35
8. Appendix .....	38
8.1. Methods .....	38

8.1.1. Field work .....	38
8.1.2. Thin sections .....	39
9.1.3. U-Th-Pb geochronology .....	39
8.1.4. Lead loss in zircons .....	40
8.2. Thin section descriptions .....	40
8.3 CL descriptions .....	44
8.4. Geochronology .....	46
8.4.1 Mean Square Weighted Deviation .....	46
8.4.2 Igneous statistics .....	47
8.4.3. Sedimentary statistics .....	50
8.5. Figures .....	54
8.6. Zircon data .....	80
8.6.1. Sample 54 .....	80
8.6.2. Sample 48 .....	83
8.6.3. Sample 26 .....	85
8.6.4. Sample 45 .....	87

## Table of Figures:

Figure 1: Regional map.....	54
Figure 2: Basic terrane descriptions.....	55
Figure 3: Schematic W-E terrane lithology ages .....	56
Figure 4: Schematic lower and middle Hazelton stratigraphy.....	57
Figure 5: Map of the Lluvia peak field area .....	58
Figure 6: Field photographs of the gray gneiss.....	59
Figure 7: Field photographs of the gray gneiss.....	60
Figure 8: Field photographs from the rusty gneiss and epidote crag.....	61
Figure 9: Sterogram showing poles to foliations and lineations.....	62
Figure 10: Stereonet of fold axes and axial planes .....	63
Figure 11: Table of mineral phases in thin section .....	64
Figure 12: Quartz microstructures. ....	65
Figure 13: Thin section textures. ....	66
Figure 14: Igneous cathodoluminescence images.....	67
Figure 15: Sample 48 cathodoluminescence images and interpretations. ....	68
Figure 16: Sample 54 cathodoluminescence images and interpretations. ....	69
Figure 17: Distribution of igneous zircon analysis .....	70
Figure 18: Igneous sample weighted mean ages.....	71
Figure 19: Igneous concordia plots.....	72
Figure 20: Sedimentary age histogram .....	73
Figure 21: Probability distribution of sedimentary ages.....	74
Figure 22: Sedimentary sample Concordia.....	75
Figure 23: Schematic cross section of Lluvia Peak .....	76
Figure 24: DeCelles orogenic cyclicity model.....	77
Figure 25: Sr, La/Yb, and magmatic flux .....	78
Figure 26: Model for deformation and underthrusting .....	79

## **Abstract**

The Central Gneiss Complex (CGC) exposes granulite facies equivalent migmatites from the middle and lower crust of a continental magmatic arc. Early Cenozoic high temperature metamorphism during isothermal exhumation overprinted much of the earlier history of the CGC and the protolith of the gneisses remains largely unconstrained. By studying a structurally higher exposure of the CGC, this study uses field methods, structural analysis, and U-Pb geochronology to better define the nature and origin of the protolith as well as the timing of deformation and magmatism within the CGC. Results suggest a correlation of the studied rocks to the lower and middle Hazelton groups exposed ~60 km to the east. Deformation along a shear zone and in kilometer-scale recumbent folds is found to have a top to the east sense of shear that occurred contemporaneously with shortening within the Skeena fold-thrust belt. This correlation and new data require the underthrusting of retroarc material beneath the continental magmatic arc following the accretion of the Insular terrane. The addition of this new material to the lower and middle crust resulted in partial melting and an increase in crustally-derived magmas during an episode of high magmatic addition rate during middle and Late Cretaceous time.



# 1. Introduction

Although continental magmatic arcs are thought to be primary localities for formation of new continental crust, voluminous magmatism characterizing exhumed batholiths involves up to 50% partial melting of existing continental crust [Ducea and Barton, 2007]. However, evaluating the contribution of trench-side or retroarc underthrusting to partial melts in these batholiths is hindered by rare exposures of continental arc roots. The Central Gneiss Complex (CGC) of western British Columbia provides a deep window into the middle crust of a convergent orogenic system that was active during Jurassic to early Cenozoic formation of the Coast Mountains batholith [Gehrels et al., 2009]. However, despite the widespread exposure of granulite and amphibolite facies migmatites that record exhumation during Eocene collapse of the Coast Mountains [Hollister et al., 2006], there are limited data constraining its earlier history due to this high grade metamorphic overprint.

In spite of nearly 50 years of research in the region, the protolith of CGC rocks is unknown [Cecil et al., 2011]. The prevailing hypothesis explaining the mid-crustal burial of rocks within the CGC is that they were buried during collision of the Alexander-Wrangellia terrane with Stikinia [Crawford et al., 1987; Hollister and Andronicos, 2006]. However, >160 km of retroarc underthrusting within the retroarc Skeena fold thrust belt has also been proposed as a burial mechanism for Coast belt rocks [Evenchick et al., 2007]. Coupled with the mainly west vergent thrust belt that accommodated Alexander-Wrangellia and Stikinia collision, this suggests material may have been underthrust from the west or the east beneath the magmatic arc. In an attempt to reduce the effects of the late-stage high temperature metamorphic overprint in deciphering the earlier history, this

study focuses upon a field locality located structurally higher in the CGC. This study strives to define the protolith age, origin, as well as the burial history of the CGC by examining age constraints on deformation styles in context with crustal-scale models for orogenesis, including mechanisms for west or east directed underthrusting of material into the middle and lower crust of a continental magmatic arc.

## **2. Geologic Background**

### **2.1. Mesozoic Tectonic Setting**

The Coast Mountains, located in western British Columbia, preserve a complex history of terrane accretion beginning in Jurassic time, including major crustal shortening, regional metamorphism, as well as the emplacement of the composite Coast Mountains batholith between 180 and 50 Ma: a continuous complex of plutonic rocks exposed along most of the British Columbia coastline and into southern Alaska [Monger et al., 1982; van der Heyden, 1992; Gehrels et al., 2009]. The terranes involved include Alexander-Wrangellia (“Insular” superterrane) exposed to the west of the Central Gneiss Complex as well as the Stikine terrane to the east (Figure 1) [Crawford et al., 1987]. Convergence resulted in two temporally separated magmatic arcs [Gehrels et al., 2009], and final amalgamation ended just after 85 Ma [e.g., Klepeis et al., 1998].

Stikinia to the east of the CGC contains an underlying sequence of Devonian to Triassic volcanic and plutonic rocks that are overlain by lower Hazelton Group volcanic rocks deposited during early Jurassic time [Gagnon et al., 2012]. The lower Hazelton Group consists of felsic volcanic strata and interbedded carbonate overlain by the sedimentary rocks of the middle and upper Hazelton Groups [Gagnon et al., 2012]. The lower Hazelton Group has an exposed width of approximately 450 km – a significant expanse that is difficult to justify as a single arc system. It was thus proposed by Marsden and Thorkelson [1992] that the lower Hazelton Group represents a sequence of volcanic rocks deposited by a dual arc system fed by two opposing subducting slabs prior to the accretion of the terrane with the North American margin. The group is calc-alkaline and characterized by a lack of variability in trace and major elements. The rocks are overlain

by a sequence of Jurassic marine sedimentary rocks deposited in the subsiding Bowser basin during accretion of the Alexander terrane [Evenchick et al., 2010; Gagnon et al., 2012]. Orogenesis and the formation of the Skeena fold-thrust belt between 120 and 140 Ma accompanied this event [Evenchick et al., 2007].

Volcanism and sedimentation along the active margin occurred during terrane accretion from Jurassic to Late Cretaceous time [Evenchick et al., 2007]. This terrane accretion was followed by a period of dextral transpression that occurred from 85 to 60 Ma, when a minimum of 1000 km northward translation is recorded across several major strike-slip faults [Wyld et al., 2006]. Paleomagnetic data suggest that at ~90 Ma, terranes may have been situated as far south as Baja California [Irving, 1996]. Magmatic addition rates in the batholith vary considerably over time, with lulls in magmatism beginning at 140 and 78 Ma [Gehrels et al., 2009] (**Figure 25**). Girardi et al. (2012) correlated periods of increased magmatic addition rates to arc processes and magma generation using elemental data. High magmatic addition rates correlate with increased  $^{87}\text{Sr}/^{86}\text{Sr}$ , which suggest increased lithospheric involvement. Girardi et al. [2012] also argues that the absence of an Eu-anomaly with La/Yb ratios, during the periods of high magmatic addition rates, indicate the magmas were derived from garnet-rich rocks below the depth of plagioclase stability. These variations provide a record for cyclicity in the magmatic addition rates, which is a similar pattern to that seen in other major continental magmatic arcs [DeCelles et al., 2009], and suggests the introduction of felsic material into the lower crust. The source of this material is not constrained, but may be related to retroarc or trench-side underthrusting [Ducea and Barton, 2007; Girardi et al., 2012]. Magmatism ceased around 48 Ma [Gehrels et al., 2009] with the end of rapid exhumation of the CGC

[Hollister, 1982].

### **2.3. CGC structure and exhumation**

The CGC is a >300 km northwest-trending belt of upper amphibolite to granulite facies gneisses and migmatites of both sedimentary and igneous origin [Roddick, 1970; Hollister and Andronicos, 2000]. At the latitude of Prince Rupert, the CGC is bounded to west by the Coast shear zone [Crawford and Hollister, 1982], and to the east by the low-angle Shames River normal fault [Heah, 1991; Andronicos et al., 2003].

The protolith of the CGC is thought to be of mixed volcanic, intrusive, and sedimentary origin, and was underthrust during accretion of the Insular and Intermontane terranes [Hollister & Andronicos, 2000]. Multi-grain U-Pb zircon geochronology of metasedimentary rocks from the core of the complex yielded age populations of 65-68 Ma and 83 Ma, as well as discordant age populations of 105 – 171 Ma [Woodsworth et al., 1983]. 12 km to the NW, Permian or older crinoid fossils were also found preserved in granulite-facies equivalent calc-silicate boudins [Hill, 1985a], suggesting that at least part of the CGC is pre-Mesozoic in age. The protolith of the CGC could be composed of one or a number of the surrounding terranes (Figure 2), and will be discussed in section 5. Discussion.

Deformation within the CGC is preserved as multiple overprinting structures that suggest burial and shortening, formation of the gneissic foliation, followed by cm- to km-scale recumbent folding, as well as extensional boudinage, shearing, and isothermal decompression related to later extension [Rusmore et al., 2005, Crawford et al., 1987, Crawford et al., 1982]. A broader scale folding of the meter scale recumbent folds has been documented in the CGC southwest of Kitimat [Rusmore et al., 2005]. Rocks within

the CGC are largely categorized into two units: a rusty weathering gneiss that is mostly sedimentary in composition and a gray weathering gneiss that is composed of metamorphosed intermediate volcanic or intrusive igneous rocks [Hollister & Andronicos, 2000].

Rocks in the CGC record isothermal decompression between 60 and 52 Ma from 8 to 3 kbars at temperatures as high as 750°C, which requires a rapid exhumation rate of 2 mm/year [Hollister, 1982; Rusmore et al., 2005]. A period of rapid extension and magmatism occurred from 53 to 48 Ma that is temporally concordant with metamorphic growth rims on zircon and slip along major extensional structures such as the Shames River fault [Andronicos et al., 2003].

Granulite-facies equivalent migmatites yield metamorphic pressures of ~4 kbar and attest to extensive melting in the core of the CGC in conjunction with the emplacement of dikes, sills, and plutons during exhumation [Crawford et al., 1987]. At structurally higher levels within the CGC to the east and west, rocks record metamorphic grades equivalent to the lower to middle amphibolite facies [Andronicos et al., 2003]. Metasedimentary rocks outside of the CGC to the east of the Shames River fault record little to no metamorphism, whereas exposed rocks of the Western metamorphic belt to the west of the Coast shear zone preserve greenschist- and amphibolite-facies conditions attributed to accretion of the Alexander-Wrangellia terrane [Crawford and Hollister, 1982; Gehrels et al., 1987].

## **2.4. Lluvia Peak Area**

The region of focus is located near Lluvia peak (Figure 1: and Figure 5:) and was selected for the prior documentation of sedimentary units and relatively lower grade of

overprinting metamorphism [Hill, 1985b] compared to the core of the CGC. These rocks present significant potential for constraining the protolith and early structural history. The field area exposes a rusty weathering pelitic gneiss overlying a gray weathering gneiss [Hill, 1985b]. The gray gneiss characterizes the most dominant lithology in the CGC, and is structurally overlain by areas of rusty gneiss in several other locations [Hutchison, 1970; Hollister and Andronicos, 2000].

Bulk geochemistry, 1-5 m-scale compositional layering, <1 m-scale carbonate beds, and a stretched pebble conglomerate provide evidence for a volcanic and sedimentary protolith of the gray gneiss [Hill, 1985b]. These observations suggest that the protolith of the gray gneiss was a package of felsic to intermediate calc-alkaline volcanic rocks with occasional layers of marine deposits, representing deposition in a coastal emergent arc setting [Hill, 1985b]. The overlying rusty weathering unit varies from calc-silicate to pelitic in composition and contains continuous layers of amphibolite that are 10s of meters thick, suggesting deposition in a shallow marine setting. Both units are highly folded and deformed [Hill, 1985b].

### 3. Methods

This study utilized mapping, structural analysis, and sample collection in the field area with a focus on the contact between the Rusty and Gray weathering units. All field locations were documented with a handheld GPS and all oriented samples were measured in situ before collection. Stereonets (Figure 9) show collected structural data including foliations, fold axes, lineations, and faults.

Samples were also collected for U-Pb geochronology in zircon. Samples were separated using standard crushing techniques. Igneous samples were handpicked under a binocular microscope and detrital samples were randomly poured, followed by imaging using cathodoluminescence at Idaho State University. U-Pb geochronology was performed at the University of Arizona's Laserchron Center, using a Nu HR Laser Ablation Multicollector Inductively Coupled Plasma Mass Spectrometer (LA-MC-ICPMS) coupled to a Photon Machines Analyte G2 Excimer laser. The data were then processed using data reduction methods outlined in Gehrels et al. [2008], followed by the Isoplot Excel plugin [Ludwig, 2001]. Individual analyses with greater than 20% discordance were discarded, as well as several that contained excessively large errors or evidence of inclusion interference. Spot sizes of 25  $\mu\text{m}$  were used for igneous cores, and spot sizes of 12  $\mu\text{m}$  were used for growth rims identified via the CL imaging. Please refer to 8.1. Methods for more detailed information.



## **4. Results**

### **4.1. Rock units**

Near Lluvia Peak, three primary rock units are exposed: 1) rusty gneiss; 2) gray gneiss; and a 3) diorite pluton. The structurally lowest unit is the gray gneiss, which is structurally overlain by the rusty-weathering gneiss. The rusty and gray gneisses are heterogeneously stratified on the outcrop scale. Both units are intruded by granodiorite and correlative dikes of the Lluvia Peak pluton.

#### **4.1.2. Gray gneiss**

The gray gneiss is a thick undifferentiated sequence of stratified rocks of igneous origin with evidence for a partial sedimentary protolith [Hill, 1985b]. It is easily distinguished by its lack of rusty weathering textures in outcrop, and was initially thought to be separated from the rusty gneiss above it by an unconformable contact primarily based upon interpreted folding of the contact near Epidote Crag [Hill, 1985b] (Figure 5). The exposed thickness of gray gneiss is a minimum of 1500 m within the field area and is likely much thicker [Hutchison, 1982].

The gray gneiss features 1-3 m scale laterally and compositionally continuous stratification in addition to the present gneissic foliation. Although deformed, the variation in composition is not metamorphic in origin, and must be sourced from initial compositional differences in deposition [Hill, 1985b]. Composition of much of the gray weathering gneiss is consistent with a mixed felsic volcanic and sedimentary protolith (detailed bulk chemistry of the gray gneiss is described by Hill, 1985b). It is primarily leucocratic metamorphosed volcanic rock containing quartz, feldspar, biotite and minor hornblende. Individual layering within the felsic units is visible texturally and varies from

fine-grained biotite rich layers (10-15%) to much coarser quartzofeldspathic layers with spaced biotite defining the major foliation (~5%). At one outcrop gradational changes in grain size and composition were observed over a distance of 10 cm in a quartzofeldspathic layer, which formed a repeating pattern across several meters. The hornblende documented mostly occurs in a few mafic compositional layers that vary between 0.5 and 1 m in thickness.

In addition to the felsic volcanic package, distinct 10-20 m thick mafic units are present. These units display a salt and pepper texture of hornblende + biotite and plagioclase + quartz. Calcareous units 10s of cm thick are also present in the gray gneiss and form thin, heavily boudinaged layers that are laterally continuous on the outcrop scale. In some larger boudins, epidote, pyroxenes, and garnet form resistant rinds around a crystalline calcite core. In addition to the primary layering, dikes ranging from intermediate to felsic in composition are visible throughout the gray gneiss and the rusty gneiss. These dikes also vary from undeformed to highly folded and boudinaged, suggesting multiple phases of intrusion.

The gray gneiss tends to form flat resistant outcrops where exposed, and generally breaks into blocky chunks along the foliation. Although not exposed within the field area above 4200 feet elevation, it tends to form large cliff faces along valley walls and ice-rounded resistant ridges beneath peaks. The resistant outcrops are more common near the contact with the overlying rusty gneiss.

#### **4.1.1. Rusty gneiss**

The rusty gneiss forms distinct 0.3 – 4 m thick compositionally distinct, stratified layers that vary from an uncommon garnet-biotite-sillimanite-quartz-plagioclase unit, to

calc-silicate and feldspar-rich fine-grained quartzites, and calc-silicate rich metamorphosed carbonates. Three thick, continuous layers of amphibolite up to 30 m thick are also exposed. These units are composed of amphibole, biotite, feldspars, and quartz with minor garnet. More than 700 m of this unit is exposed within the field area atop Lluvia and Niebla peaks, as well as Redcap Mountain [Hill, 1985b] 4 km to the northeast.

The major gneissic foliation throughout the unit is parallel to the compositional layering. Its expression is different in each compositional unit, but is primarily expressed by a 0.5-2 cm thick metamorphic layering. A finely spaced schistose foliation is present in the biotite rich units. In the pelitic units, the gneissic fabric is defined by distinct layers of biotite and sillimanite. In quartzofeldspathic and calc-silicate rich units, continuous quartz-rich layering and thin, discontinuous quartz lenses define the gneissic fabric. With the exception of some the quartz rich lithologies, the rusty weathering gneiss is fine-grained.

The rusty weathering gneiss is most easily identified by its rusty color in outcrop, which is a result of an abundance of pyrite throughout the unit [Hill, 1985b]. It forms steep, blocky, and resistant faces where ice scoured and plucked pieces along bedding planes. Interlayered amphibolite units weather to resistant cliff faces where exposed and form distinct visible layers 10's of meters thick.

#### **4.1.3. Lluvia Peak pluton**

The Lluvia Peak pluton is a sill-shaped granodiorite pluton found within the rusty-weathering unit; it locally crosscuts the contact with the gray gneiss. It composes the top 500 m of Lluvia Peak. Only the bottom portion of the pluton is exposed, so the original

spatial extent of the pluton is unknown. The pluton contains small variations in visible mineral phase distribution and grain size. Primary minerals are coarse and equigranular, and include quartz (~30%), plagioclase (~50%), biotite (~10%), hornblende (~5%), opaques (~5%). Biotite aggregates in the field vary in size from a few mm to several cm across. Potassium feldspar is locally uncommon and makes up less than 10% of the rock. Grain size coarsens locally. Detailed bulk chemistry was completed by Hill [1985b].

The Lluvia Peak pluton produces pronounced ridges and cliffs where exposed. The pluton displays minor to no visible chemical weathering in outcrop. Physical surfaces are either angular or rounded along fractures. The pluton is undeformed and contains no visible foliations.

## **4.2. Structural geology**

### **4.2.1. Outcrop scale observations**

Structural measurements from the gray gneiss include foliations, lineations, fold axial surfaces, and fold axes, and were plotted on a stereonet (Figure 9, Figure 10). The measured foliations dip 10-25 degrees westward, and the poles form a loose cluster. Representative foliation dips at different locations on the map (Figure 5) show subtle variations across the field area. Foliations on the southeastern ridge dip westward at 15-25 degrees, whereas to the north, and near Epidote Crag, foliations have shallower dips ~10° and tend to be rotated more to the south. These measurements represent the visible elongation in the stereonet cluster.

The southeastern ridge off Niebla Peak (Figure 5) contains a well-exposed section of the gray-weathering gneiss and the lower part of the unit that forms the contact between it and the rusty-weathering gneiss.

In the structurally lowest gray gneiss exposed along the ridge rocks exhibit a

pervasive flattening fabric and biotite-defined foliation. Here, dikes commonly crosscut the foliation and are deformed by varying amounts; some are folded into cm-scale isoclinal folds with rootless limbs (Figure 7). Strain was partitioned into felsic layers. Less deformed dikes form meter-scale boudins that were elongated toward the east-west and north-south with rare asymmetry, whereas others were folded into meter-scale recumbent folds whose axes dip ~parallel to the measured stretching and mineral lineations. Fold limbs are often boudinaged when viewed on E-W facing outcrops. Asymmetric strain fabrics are rare in this section, but are found in occasional S-C fabrics and rare clast and boudin asymmetry. All of these asymmetric structures display a top to the east sense of shear (Figure 6).

Structurally above this lowest unit, meter-scale zones of higher shear strain are indicated by the presence of asymmetric boudins, S-C fabrics, and grain size reduction. Meter and centimeter scale recumbent folds as well as areas of extreme flattening become more common in the gray gneiss near the contact. In one location (station 26), a 30 cm thick granodiorite dike crosscuts a meter-scale recumbent fold and contains a distinct foliation-parallel tectonic fabric (Figure 6). This fabric is compositionally variable on a 1 cm scale and exhibits dynamic recrystallization of quartz and up to 1 cm diameter relict plagioclase clasts.

Large felsic dikes and pegmatites are more abundant near the contact, the largest of which are on the scale of 0.5-1 m and largely undeformed. 50 m below the base of the contact with the overlying rusty gneiss is a 20-30 m thick section of amphibolite that displays salt and pepper (plagioclase + hornblende) texture with a strong hornblende-defined foliation. Laterally continuous strings of carbonate boudins are common within

this layer as well as dramatic 10 cm scale folding of cm-thick, foliation-parallel, compositional layering and dikes. A 3 m thick section of intermediate composition gray gneiss within this unit is highly sheared with visible grain size reduction, rotated calc-silicate boudins, and a visible C-fabric. The area structurally above this unit is characterized by areas of increased strain that suggest a top to the east sense of shear (Figure 7), but is mostly obscured by a permanent snow field. ~500 m along strike to the north, a sheared amphibolite unit defines the transition into the shear zone with increasing strain structurally upwards.

At the top of the snow field the contact layer between the rusty and gray gneisses forms a vertical cliff 20-30 m high that transitions to the rusty weathering gneiss near the top. This cliff forming unit continues along-strike beneath Lluvia Peak to Epidote Crag and is visible on Redcap Mountain 4 km to the northeast. In outcrop this unit is characterized by extreme grain size reduction, a pervasive S-C fabric defined by elongated quartz aggregates as well as relict 0.5-2 cm thick transposed layers of mafic composition that lay oblique to the c fabric (Figure 6). This unit was interpreted in the field as a thick zone of ultramylonite. The foliation in the shear zone is parallel to subparallel to the foliations measured structurally beneath it. Along-strike, the composition changes slightly with the absence of transposed mafic layers, an increase in the biotite phase, as well as the presence of garnet (Figure 7). Near Epidote Crag, the thick amphibolite unit is not present within the gray gneiss near the shear zone. The shear zone is crosscut by the undeformed Lluvia Peak pluton at this locality.

On the western edge of the field area near Epidote Crag, a stretched pebble conglomerate is locally exposed (station 48). The pebbles are defined by a more felsic

composition than the more pelitic matrix around them. The pebbles are strained into L=S to L>S tectonites that are distinct from the flattening fabric described structurally lower in the section.

Above the shear zone contact, the rusty weathering gneiss forms a large km-scale recumbent fold preserved near Lluvia Peak where the rusty gneiss is exposed. The axial plane of this fold dips gently to the north, based on field observations and mapped units, and is oblique to the shear zone orientation (Figure 5). The geometry of the fold is visibly traceable from epidote crag via the folded amphibolite units. The shear zone obliquely truncates the units of the rusty weathering gneiss, including this major fold. The Lluvia Peak pluton, in turn, crosscuts the fold and the shear zone.

Smaller scale folding on the order of 10s of centimeters within the rusty unit that was most commonly preserved in calc-silicate and quartzofeldspathic layers (Figure 8). We observed little evidence of folding in the finer grained sillimanite-rich pelites. Evidence for ductile shear and mylonitization of the rusty weathering units is uncommon, and preserved shear fabrics are rarely observed. Major foliations and gneissic banding is parallel to compositional layering in the unit. A schematic E-W cross section of the area across Lluvia Peak and Epidote Crag can be found in Figure 23.

#### **4.2.2. Recumbent folding**

The observed folding in the field area occurs at several different scales, orientations, and styles. In addition to the kilometer scale fold in the rusty gneiss, a set of large (200-300 m wavelength) recumbent folds within the gray gneiss are visible on the east face of Lluvia Peak below the shear zone, and have a similar orientation to the larger fold above them.

Smaller scale folding is abundant throughout the field area, but is most visible in the gray gneiss where the visual contrast between the layers is more apparent. Axial surfaces to these folds are parallel to sub-parallel to the foliation (Figure 9). Fold axes are roughly parallel to the lineation in most cases, dipping gently to the west and southwest with some variability. Fold limbs are commonly boudinaged perpendicular to the flattening direction. In some localities, tightly folded quartz-rich dikes are heavily transposed such that it is not possible to trace individual hinges and limbs across the outcrop (Figure 7). Ptygmatic folds are rare within the gray weathering gneiss.

#### **4.2.3. Grain-scale crystal-plastic deformation mechanisms**

Deformation and microstructures in thin section are similar structurally across the field area. Both the gray and rusty weathering gneisses contain evidence for extensive dynamic recrystallization of quartz. In the gray gneiss, quartz exhibits subgrain formation, interlobate grain boundaries and widespread recovery to 120 degree triple junctions (Figure 12). Undulose extinction is also present in some grains. High-grade crystal-plastic deformation of quartz is thus interpreted to have primarily occurred through grain boundary migration (GBM) [Passchier and Trouw, 2005], and were later recrystallized to form polygonal grain boundaries.

Feldspar is primarily defined by a polygonal granoblastic texture, but locally contains extensive formation of subgrains and rare interlobate boundaries between grains. Kink bands and undulose extinction is rare, but present in some samples. The feldspar is interpreted to have deformed primarily through sub grain rotation (SGR) with local evidence for GBM, followed extensive grain recovery.

Samples from the contact between the rusty and gray weathering gneisses exhibit



a few interlobate grain boundaries of quartz in a fine quartzofeldspathic matrix. The fine grain size is present only in the samples from the shear zone and is almost entirely annealed. Quartz also occurs in elongate ribbons with minor undulose extinction and lobate boundaries.

In the rusty gneiss, recrystallization textures are similar, but are influenced by the mineral composition of the matrix, where biotite, pyroxene, sillimanite, or garnet is present. Biotite is found parallel to the foliation and defines the matrix in some of the more mafic units, and is commonly found around aggregates of quartz and plagioclase. Quartz forms symmetric pressure shadows around porphyroblastic garnet and hornblende that is visible both in thin section and hand sample. Quartz and feldspar both exhibit grain recovery to polygonal boundaries in the hinges of cm-scale folds.

See Figure 11 for phases documented in each sample. Sample locations can be found on the map and are labeled according to their field station. Descriptions for each thin section can be found in section 8.2. Thin section descriptions.

#### **4.2.4. Overprinting brittle deformation**

On the ridge northeast of Lluvia peak, a zone of cataclasite occurs twenty meters above the shear zone, within a biotite-amphibolite layer of the rusty weathering gneiss (Figure 8). The cataclasite is characterized in outcrop by rotated plagioclase porphyroclasts mantled by anastomosing biotite. Transposed dike limbs exhibit increasing simple shear toward the slip plane, suggesting semi-brittle failure. The cataclasite makes up several discrete layers separated by 5-20 cm thick layers of ductilely deformed quartz-rich layers. Biotite is locally altered to chlorite and forms asymmetric fish that also yield a top to the west sense of shear. Across the zone of cataclasite, an otherwise undeformed

felsic dike is offset with a top to the west sense of shear. Increasing strain toward the deformed zone and S-C fabrics in thin section also agree with a top to the west sense of shear (Figure 13).

Several ~60°-dipping, primarily north-south striking normal faults crosscut the field area. These faults vary from several centimeters of displacement to hundreds of meters where the rusty unit is displaced against the zone of ultramylonite. Fault traces are correlated with fractured rock and areas of increased erosion. Epidote mineralization preferentially occurs along the fault faces and locally in the nearby host rock where fractures contain void-filling euhedral crystals up to 3 cm in length. Chlorite alteration is also common along the surfaces along and near fault surfaces

### **4.3. U-Th-Pb zircon geochronology**

Zircon age data for all four samples is compiled in appendix 8.6. Zircon data. See appendix 8.4. Geochronology for detailed descriptions of results, and appendix 8.3 CL descriptions for detailed descriptions of CL images for each sample. Peak temperature conditions are estimated to be  $702 \pm 50^{\circ}\text{C}$  [Hill, 1985b], which is well below the range in which lead diffusion begins to play a significant role for 100  $\mu\text{m}$  scale grains, which is  $\sim 950^{\circ}\text{C}$  at a cooling rate of  $10^{\circ}\text{C}$  per million years [Cherniak and Watson, 2000].

#### **4.3.1 Igneous geochronology:**

At station 26 in the gray gneiss, a foliated felsic dike crosscuts a meter scale recumbent fold. We sampled this dike (sample 26) as well as the Lluvia Peak pluton (sample 45) in order to better constrain the timing of prior deformation (Figure 14). The zircon grains from these samples are euhedral and elongate in form, and contain either a consistent oscillatory zonation pattern throughout, or contain an inner core mantled by a

oscillatory zoned outer rim. The cores tend to be rounded to elongate with irregular zoning patterns, and show evidence for dissolution around the edges. We used zoning patterns in the cathodoluminescence images to guide the location of the laser spot and date different portions of the grain.

Both rim and core ages from the two igneous samples are plotted in Figure 17. In both samples, two age distributions are recognized: ~200 Ma igneous cores, and ~80 Ma rims. Given the clear oscillatory-zoned rims surrounding irregular, relict cores, the rim ages are interpreted to represent pluton crystallization. Despite taking care to sample different age domains in the zircon crystals, following data acquisition several laser spots appear to have slightly overlapped adjacent CL domains. As such, these ages were interpreted to be mixed ages and were excluded from further age analysis. A weighted average for the crystallization age was conducted using only the younger rim ages (Figure 18). This resulted in a calculated age of  $78.5 \pm 2.6$  Ma (MSWD = 6.7) for sample 26 and  $80.2 \pm 1.0$  Ma (MSWD = 0.98) for sample 45. The zircon ages are concordant for both samples and are statistically indistinguishable (Figure 19).

#### **4.3.2 Sedimentary geochronology:**

Samples 48 and 54 were collected from the stretched pebble conglomerate and a quartz-rich calc-silicate layer in the overlying rusty gneiss (Figure 15 and Figure 16). Zircon grains are subhedral to rounded in shape, containing thin homogeneous rims separated from complexly zoned cores by irregular boundaries with evidence for dissolution or corrosion.

Age distributions from the sedimentary samples (Figure 20) show a dominant age population between 180 Ma and 210 Ma for sample 48, with a smaller distribution of

ages around 50 Ma. Sample 54 shows a similar pattern of ages, however it contains a handful of ages between 170 and 180 Ma whereas sample 48 does not. The single larger age peaks were plotted on a histogram to show the probability distributions of the grain cores (Figure 21). Both of these distributions have an approximately Gaussian distribution. The younger ages are all from the zircon rims and represents a late phase of metamorphism based on these visual constraints. The ages from both samples are concordant (Figure 22).

## **5. Discussion**

### **5.1. History and structural evolution of the field area**

#### **5.1.1. Deposition and protolith constraints**

In accordance with Hill [1985b], compositional layering, stretched pebble conglomerate, local carbonate interlayers, rare apparent primary sedimentary structures, and highly aluminous layers suggest a volcanic and sedimentary origin for the gray and rusty weathering gneisses. Interpreted as such, the gray weathering gneiss contains felsic volcanic layers, mafic volcanic rocks, rare carbonate beds, and a pebble conglomerate. This sequence points to a period of felsic volcanism in an aqueous to subaqueous environment. The pebble conglomerate suggests a higher energy episode of deposition during an eruptive event or decrease in sea level. In the Hazelton Group, both aqueous deposition of carbonate beds and subarial volcanics and flows are described [Gagnon et al., 2012].

Finer grained pelites in the rusty weathering unit represent a shift in depositional environment and a decrease in intensity of local volcanism. Lithologic changes from metapelites to carbonate to quartz-dominated lithologies are present over a scale of a couple meters, and are interrupted by the amphibolite units up to 10s of meters thick that sit parallel to composition of the metasediments. The rusty unit exposed at Lluvia Peak is thus interpreted as a sequence of carbonates and fine siliciclastic sediments deposited in a shallow marine environment, interrupted by periods of mafic volcanism or intruded by mafic sills prior to deformation and high grade metamorphism.

Metasedimentary samples collected from the gray weathering gneiss (sample 48) and overlying rusty weathering gneiss (sample 54) contain similar detrital zircon populations. The gray gneiss sample contains a spread of ages between 180 and 210 Ma,

whereas the rusty sample age distribution contains a spread of ages between 170 and 210 Ma. The narrow distribution of detrital zircon ages for both samples may result from a locally derived source or a continuous supply of young zircons during ongoing magmatism.

### **5.1.2. Structural history and magmatism**

The earliest deformation preserved in the field area is a pervasive composition-parallel foliation, which is crosscut by all other structures. Dikes and compositional layers show boudinage with the stretching direction parallel to this plane. Dikes throughout the field area are deformed to varying degrees and must have been intruded throughout progressive strain and folding in the area. Fold axial surfaces are parallel to the foliation (Figure 9, Figure 10), and highly deformed cm-scale recumbent folds also exhibit limbs transposed along the foliation plane. These structures provide evidence for major pure shear throughout the field area.

Large scale recumbent folding and shearing either postdates or occurred concurrently with the widespread flattening fabric. The kilometer-scale fold characterizing much of the rusty-weathering gneiss overturns both the compositional layering and the foliation. This folding event also produced the meter-scale recumbent folding present in both the rusty and the gray weathering gneiss. It is difficult to distinguish the timing of the smaller scale folding located in some of the highly strained rocks, which may represent progressive deformation during shearing.

The contact between the rusty and gray weathering units crosscuts the lower limb of the large recumbent fold in the rusty gneiss. This can be seen in map view where the amphibolite units in the rusty gneiss are truncated by the contact. Below the unit contact,

asymmetric strain fabrics indicate an increasing component of top to the east shear strain upward toward the contact. Everywhere observed, the contact is defined by a ~20-30 m thick zone of fine-grained rock. These observations suggest that the contact is a shear zone with a major component of flattening and that shear occurred after the onset of folding. The presence of asymmetric pre-boudinage structures in some dikes also suggest that some amount of stretching or flattening occurred during the shearing event. Further microstructural analysis indicates that although grain size reduction and dynamic recrystallization of quartz in the form of grain boundary migration is evident, significant post-strain static recrystallization and recovery has overprinted most textures. Extensive strain within the shear zone is only evidenced in thin section by the presence of the elongated quartz ribbons and relict quartz grain boundary textures (Figure 12).

Given the apparent similar ages of units across the shear zone, the displacement magnitude is difficult to constrain. The pelitic and amphibolite layers in the hanging wall that are truncated by the shear have no corollary exposed elsewhere in the footwall, placing minimum constraints of several kilometers of eastward movement of the hanging wall relative to the footwall. One possibility is that the shear zone exploited the mechanical weakness near the boundary of the two units. Alternatively, the shear zone, which dips gently to the west, may have cut previously dipping units. In this particular case, the compositional layering in the gray gneiss dips 20° to the west on average, while the shear zone is nearly horizontal, such that it cuts down section to the west (Figure 23). During slip, this would place the younger rusty gneiss on top of the gray gneiss. Although the movement across the shear zone discussed here is significant, similarities in zircon populations across it place spatial constraints on deposition proximity and thus lateral

movement of the rusty and gray gneisses relative to each other.

The period of shearing and recumbent folding is temporally constrained by a  $78.5 \pm 2.6$  Ma U-Pb zircon age of a foliated, fold-cutting dike (Figure 6). This sample contains some proportion of crustal melt based upon relict zircon cores. In addition, the Lluvia Peak pluton, located in the hinge of the large recumbent fold is undeformed and dated to be  $80.2 \pm 1.0$  Ma. The two ages of the igneous samples are statistically the same, however the dike contains a clear tectonic foliation while the pluton does not. Strain is unlikely to have been preferentially partitioned into the intermediate composition gray gneiss over a lithology dominated by pelites, carbonate, quartzite and a felsic pluton. This implies that the Lluvia peak pluton was emplaced after cooling and strain of the crosscutting dike had ceased. The very close ages of the two samples thus place particular constraints on when major ductile strain and shearing in the field area ended. Progressive shearing and folding would have occurred up until intrusion of the dike where it immediately ended prior to crystallization of the Lluvia peak pluton. Shearing is then constrained to have ended at approximately  $\sim 80$  Ma. This predates the younger exhumation phase of the CGC between 60 and 48 Ma [Andronicos et al., 2003; Rusmore et al., 2005]. The movement along the shear zone coincides temporally with convergence within the Skeena fold-thrust belt to the west [Evenchick, 1991; Evenchick et al., 2007], and may represent a middle crustal expression of the same system. A significant proportion of crustal thickening and shearing may be accommodated in the middle crust through a combination of shear strain and folding [Betka et al, 2015]. This is expressed in the Lluvia Peak area through the presence of widespread recumbent folds in both units. In the gray gneiss, the number of small scale recumbent folds increases toward the shear



zone.

The presence of a crustal component in both the pluton and crosscutting dike, which were intruded near the end of deformation and shortening in the field area, suggest that peak metamorphism occurred during this time. Hill [1985b] also documented migmatites in the field area – although it is unclear whether they are related to this phase, or isothermal decompression of the CGC. The zircon cores preserved from the two igneous samples were found to be between 190 and 230 Ma and do not contain any of the younger ages between 170 and 190 Ma that are present in the surrounding metapelites. The age relationships and the presence of partial melts suggests that the rocks were near the solidus, and that the melt may have been derived from a nearby source – perhaps structurally lower in the section.

Pressure and temperature conditions are better constrained by examining metamorphic recrystallization textures. Most of the samples collected exhibit high-grade dynamic recrystallization of its components under strain, but have since been overprinted by late-stage grain recovery. Evidence for GBM is preserved for quartz in nearly all samples (Figure 12), but is only locally preserved in plagioclase in several samples. Although GBM is the primary deformation mechanism for quartz, the feldspar recrystallized by a mixture of GBM and SGR based upon both textures being preserved. The quartz microstructures are evidence for widespread strain and dynamic recrystallization to have occurred at temperatures greater than  $\sim 550^{\circ}\text{C}$  [Stipp et al., 2002; Passchier and Trouw, 2005]. Plagioclase also exhibits grain boundary migration textures (Figure 13). Plagioclase generally requires higher temperatures than quartz for similar microstructures and increases the minimum temperature estimates for dynamic

recrystallization [Passchier and Trouw, 2005]. Cuspate boundaries between quartz and plagioclase, and between individual plagioclase grains suggest maximum deformation temperatures above 650°C [Rosenburg and Stünitz, 2003]. The static recrystallization and recovery suggests either a second influx of heat, or that metamorphism outlasted deformation.

Pelitic and calc-silicate samples of the rusty-weathering gneiss provide the best-constrained phase equilibria and metamorphic textures. The rocks lie within the sillimanite stability field, as well as within the enstatite-diopside stability fields for calc-silicates. Staurolite is only stable in the matrix near the peak of Redcap Mountain 4 km to the northeast. Given that quartz-staurolite is only stable to ~700°C, it is likely that the rocks in the Lluvia peak area that lack staurolite exceeded this temperature [Hill, 1985b]. Absence of muscovite may also indicate that metamorphic grade exceeded the muscovite + quartz stability field [Day, 1973]. Hill [1985b] also used a garnet-biotite geothermometer and a garnet-plagioclase-sillimanite-quartz barometer to constrain peak metamorphic conditions to  $702 \pm 50^\circ\text{C}$  and  $7.6 \pm 1$  kbar. The conditions thus were near the solidus for these rocks, with a minimum burial depth of ~25 km. At Redcap Mountain 4 km to the northeast within the CGC, kyanite was found preserved as garnet inclusions [Hill, 1985b], and gives evidence for a period of higher pressures during garnet growth where the kyanite is captured and preserved during later metamorphic events.

### **5.1.3. Exhumation**

In the field, cataclasite constrains a period of late top to the west deformation that is overprinted by high-angle faults. These are both interpreted to represent post ~80 Ma extension. Quartz microstructures in the cataclasite samples show several overprinting

textures from within the zone including the formation of subgrains and bulging recrystallization that overprints a relict GBM recrystallization texture (Figure 13: Thin section textures.). This places deformation temperatures to somewhere between 350 and 500°C [Stipp et al., 2002]. Rotated plagioclase porphyroclasts contain limbs of recrystallized quartz. In addition to this are brittle textures and slip surfaces characterized by fine biotite grains. Thus, the transition from high to low temperature extension was partially accommodated by normal faulting.

This phase of deformation may also be connected to metamorphic overgrowths dated between 55 and 48 Ma that are present in both sedimentary samples. These ages, and the apparent dissolution of the relict detrital zircon grains, correlate well with the latest phase of exhumation documented through the CGC [Hollister et al., 1982, Heah et al., 1991] in which exhumation is found to have occurred between 60 and 48 Ma.

Retrograde metamorphism is most commonly expressed by the partial replacement of biotite with chlorite. In the cataclasite, biotite has been nearly completely replaced by chlorite. Sericitic alteration of plagioclase is also common in the igneous samples 14DM45 (Lluvia Peak pluton) and 14DM47 (shear zone cutting dike). Void-filling epidote mineralization relating to the late high angle normal faulting is also present in the field area. This block faulting is the latest phase of exhumation.

## **5.2. Hazelton protolith interpretation**

The Lluvia Peak field area contains Jurassic volcanic and sedimentary rocks that represent both a marine and subaerial environment in the gray gneiss and marine clastic sediments of rusty gneiss. While the amount of movement across the shear zone is poorly constrained, detrital zircons distributions from both units are similar and may represent

either a similar timing of deposition, or a progression from felsic volcanics to a marine clastic dominated lithology.

The exposed lithologic sequence within the Lluvia Peak area is strikingly similar to the Hazelton Group exposed ~60 km to the east. The lower Hazelton Group varies in form, but is generally a sequence of intermediate to felsic lava flows between 5 and 15 m in thickness with arc signatures [Marsden and Thorkelson, 1992]. The flows vary between calc-alkaline and tholeiitic, contain occasional layers of marine sediments, and represent an emerging arc system. The top of the lower Hazelton Group is a locally unconformable surface where a transition to marine clastic sediments occurred. [Gagnon et al., 2012 and sources within].

U-Pb zircon data reported here for the Lluvia Peak area contain a unimodal normal distribution of ages between 210 and 180 Ma, which closely matches the ages compiled by Gagnon et al. [2012] for felsic volcanic and metasedimentary rocks of the lower Hazelton Group. These ages do not correlate nearly as well with the timing of magmatism in other nearby potential protoliths such as the Alexander terrane, where volcanism occurred during and prior to the Paleozoic with a smaller pulse in the Alexander terrane in the late Triassic [Gehrels et al., 1987]. Although the Wrangellia terrane contains Jurassic volcanic rocks, it is unlikely to be the protolith due to its great distance from the Lluvia Peak area and the presence of the Alexander terrane between them. While transportation of young grains is possible, there is evidence for volcanism in the immediate area during sediment deposition.

The Hazelton stratigraphy also correlates well with unit descriptions and protolith interpretations at Lluvia Peak including the contemporaneous deposition of volcanic

rocks and clastic sediments in both units where shallow marine sediments overly the volcanic package (Figure 4) Thick mafic flows in the clastic sediments of the exposed Hazelton group closely resemble the ~30 m thick layers of composition-parallel amphibolite located in the rusty gneiss. In addition to the observation and detrital ages from the Lluvia Peak areas, new ages obtained from the gray gneiss at a locality ~30 kilometers south of the Lluvia Peak area yielded concordant ages of ~314 Ma [MacLeod and Pearson, 2014], which are similar to the documented Stikinia basement atop which the lower Hazelton Group was deposited.

The presence of the Hazelton Group within the eastern extent of the Central Gneiss Complex places the known western boundary of the Stikine terrane and suture with the Insular terrane west of the field area and increases the width of the Hazelton basin by >60 km westward. Identification of the Hazelton Group within the Central Gneiss Complex also requires that these rocks were buried to middle and lower crustal depths of the orogen, undergoing top-to-the-east general shear concurrently with major crustal shortening accommodated by the east-vergent Skeena fold-thrust belt [Evenchick et al., 2007].

### **5.3. Tectonic model**

DeCelles et al. [2009] put forth a simplified model of orogenic cyclicity that proposed retroarc burial beneath the magmatic arc, followed by extensive partial melting and voluminous arc magmatism (Figure 24). The model predicts an increased crustal component to magmatism, which should be observed in increased  $^{87}\text{Sr}/^{86}\text{Sr}$  ratios in the melt. The model proposes that during major crustal melting and partial melting of the mantle wedge, an eclogitic root forms and becomes gravitationally unstable, resulting in

an increase in accommodation space beneath the arc and increasing rates of underthrusting. According to the model, delamination and introduction of new material would coincide with a lull in magmatism which would reboot as the crustal material is reheated – creating a cycle of magmatic addition rates with increased crustal involvement following shortening in the thrust belt.

The variation in magmatic addition rates in the Coast Mountains batholith (Figure 25) as well as the similar timing between it and the  $^{87}\text{Sr}/^{86}\text{Sr}$  ratios points to a correlation between increased addition rates and an increased crustal component of the melt. This follows closely with what is predicted by the DeCelles [2009] orogenic cyclicity model where the high flux events are driven by melting of the crust beneath the magmatic arc.

In the study area, the Lluvia Peak pluton was intruded between 78 and 80 Ma, at the end of peak magmatic addition rates within the Coast Mountains batholith [Gehrels et al., 2009]. This followed major flattening and top-to-the-east shearing, likely related to the concurrent [Evenchick et al., 2007] Skeena fold-thrust belt, interpreted here to have buried rocks to mid-crustal levels. While pulses of deformation throughout the history of the fold thrust belt are not well constrained, the data presented here show that deformation, and therefore shortening, continued until at least 80 Ma. A causal relationship between underthrusting of material along a décollement into the middle and lower crust and partial melting is expected to occur due to the introduction of material into high temperature conditions. Zircon geochronology shows that many of the grains contain relict xenocrystic cores that suggest a crustal melting source, the timing of which matches an episode of increasingly isotopically evolved magmas within the Coast Mountains batholith [Girardi et al., 2012] (Figure 25).

Using the data collected in the Lluvia Peak area, a model for retroarc underthrusting and burial of Stikinia can be constructed. A minimum of 160 km of shortening was accommodated by the Skeena fold-thrust belt during the Cretaceous, and involves underthrusting of supracrustal material beneath the active arc [Evenchick et al., 2007]. Crustal thickening then triggered a period of high flux magmatism related to melting of the lower crust. The high  $^{87}\text{Sr}/^{86}\text{Sr}$  was still present during the 60-50 Ma period of high magmatic addition rate, which coincides with major crustal extension and isothermal exhumation of the Central Gneiss Complex.

Retroarc underthrusting also allows for the progressive deformation seen in the field area. Burial of material beneath the main décollement of the fold thrust belt resulted in the initial period of widespread pure shear and the formation of the primary gneissic foliation. As the material was buried to deep levels in the crust, the main décollement would either step structurally downwards, or would be partially partitioned away from the primary structure and accommodated along smaller shear zones and kilometer-scale recumbent folds (Figure 26). The shear zone located within the field area closely resembles what would be expected of a hanging wall flat on footwall flat relationship in the middle crust, where strain was partitioned into the footwall of the primary décollement.

This suggests a tectonic setting in which accretion at the active convergent margin resulted in the burial of a portion of Stikinia beneath the fold-thrust belt and volcanic arc. Eventual heating of supracrustal material in the middle and lower crust resulted in partial melting of the underthrust material and emplacement of crustally derived plutons. The DeCelles et al. [2009] model for retroarc underthrusting is applicable to the Coast

Mountains batholith, but does not necessarily require cyclicity to have occurred. Only a single period of high flux magmatism is recorded and continues throughout deformation across the Skeena fold thrust belt. Ongoing deformation until 80 Ma in the Lluvia Peak area give further evidence that melts with a significant crustal component formed during ongoing shortening. Further investigation of the nature and timing of deformation is required before a more comprehensive model can be constructed.



## 6. Conclusions

This study contributes to our understanding of the timing and mechanism of burial of rocks of the Central Gneiss Complex, overcoming complications from an overprinting early Eocene granulite-facies metamorphism by focusing on an area structurally higher in the CGC and spatially controlled geochronology.

Results presented here document folded and sheared rocks of a mixed metasedimentary and metavolcanic origin that represent an emergent arc setting. Structural analysis of crosscutting relationships constrain progressive deformation and pure-shear-dominated strain. The Lluvia Peak area records extensive flattening and shearing in the form of widespread boudinage, strain fabrics, and the formation of both centimeter and kilometer scale recumbent folds. A shear zone that forms the contact between the two primary units was crosscut by an undeformed crustally-derived pluton at 80 Ma. Lithologic descriptions and 170-210 Ma detrital zircon ages from metasedimentary units constrain a maximum age of sediment deposition, suggesting a correlation of these units with the lower Hazelton Group exposed on the eastern edge of the CGC. Metamorphic rims correlate in time to 60-48 Ma isothermal exhumation of the Central Gneiss Complex. Overall, results suggest that the western edge of Stikinia was underthrust beneath the continental magmatic arc in the hinterland of the Skeena fold-thrust belt, followed by partial crustal melting, which temporally coincides with an interval of high magmatic addition rates in the Coast Mountains batholith.

These events, including the correlation between high magmatic addition rates and isotopic ratios, are predicted by the DeCelles [2009] orogenic cyclicity model. Analysis of compiled isotopic data from volcanic arcs has shown that no more than 50% of the

material can be derived from the mantle [Ducea and Barton, 2007]. Retroarc underthrusting provides a mechanism for the introduction of material into the lower crust as well as a source for large volumes of crustal melts. The Central Gneiss Complex represents a rare and vast exposure of the middle and lower crust that provides a unique view into the process of retroarc underthrusting and melt generation at a convergent margin.

## 7. References

- Andronicos, C. L., D. H. Chardon, L. S. Hollister, G. E. Gehrels, and G. J. Woodsworth (2003), Strain partitioning in an obliquely convergent orogen, plutonism, and synorogenic collapse: Coast Mountains Batholith, British Columbia, Canada, *Tectonics*, 22(2).
- Armstrong, R. L., and D. Runkle. (1979), Rb-Sr geochronometry of the Ecstall, Kitkiata, and Quottoon plutons and their country rocks, Prince Rupert region, Coast Plutonic Complex, British Columbia, *Canadian Journal of Earth Sciences* 16(3), 387-399.
- Cecil, M. R., G. E. Gehrels, M. N. Ducea, and P.J Patchett (2011), U-Pb-Hf characterization of the central Coast Mountains batholith: Implications for petrogenesis and crustal architecture, *Lithosphere*, 3(4), 247–260.
- Cherniak, D. J., and E. B. Watson (2001), Pb diffusion in zircon. *Chemical Geology* 172(1), 5-24.
- Coney, P. J., D. L. Jones, and J. W. Monger. (1980) Cordilleran suspect terranes, *Nature* (288), 329-333.
- Crawford, M. L., and L. S. Hollister, (1982) Contrast of metamorphic and structural histories across the Work Channel lineament, Coast Plutonic Complex, British Columbia, *Journal of Geophysical Research: Solid Earth*, (87)B5, 3849-3860.
- Crawford, M. L., L. S. Hollister, and G. J. Woodsworth. (1987) Crustal deformation and regional metamorphism across a terrane boundary, Coast Plutonic Complex, British Columbia, *Tectonics* 6(3), 343-361.
- Day, H. W. (1973), The high temperature stability of muscovite plus quartz. *American Mineralogist*, 58, 255-262.
- DeCelles, P. G., M. N. Ducea, P. Kapp, G. Zandt (2009), Cyclicality in Cordilleran orogenic systems, *Nature Geoscience*, 2(4), 251-257.
- Ducea, M. N., and M. D. Barton (2007), Igniting flare-up events in Cordilleran arcs, *Geology*, 35(11), 1047–1050.
- Evenchick, C. A. (1991) Structural relationships of the Skeena fold belt west of the Bowser Basin, northwest British Columbia, *Canadian Journal of Earth Sciences* 28(6), 973-983.
- Evenchick, C. A., M. E. McMechan, V. J. McNicoll, and S. D. Carr (2007), A synthesis of the Jurassic–Cretaceous tectonic evolution of the central and southeastern Canadian Cordillera: Exploring links across the orogeny, *Geological Society of America Special Papers*, 433, 117-145.
- Evenchick, C. A., T. P. Poulton, and V. J. McNicoll (2010), Nature and significance of the diachronous contact between the Hazelton and Bowser Lake groups (Jurassic), north-central British Columbia, *Bulletin of Canadian Petroleum Geology*, (58)3, 235-267.
- Gagnon, J. F., T. Barresi, J. W. Waldron, J. L. Nelson, T. P. Poulton, F. Cordeye (2012),

- Stratigraphy of the upper Hazelton Group and the Jurassic evolution of the Stikine terrane, British Columbia 11 ESS Contribution 20120051, *Canadian Journal of Earth Sciences*, 49(9), 1027-1052.
- Gehrels, G. E., and J. B. Saleeby, (1987), Geologic framework, tectonic evolution, and displacement history of the Alexander terrane, *Tectonics*, (6)2, 151-173.
- Gehrels, G. E., V. A. Valencia, and J. Ruiz (2008), Enhanced precision, accuracy, efficiency, and spatial resolution of U - Pb ages by laser ablation - multicollector - inductively coupled plasma - mass spectrometry, *Geochemistry, Geophysics, Geosystems*, 9(3).
- Gehrels, G. E., et al. (2009), U-Th-Pb geochronology of the Coast Mountains batholith in north-coastal British Columbia: Constraints on age and tectonic evolution, *Geological Society of America Bulletin*, 121(9-10), 1341-1361.
- Girardi, J. D., P. J. Patchett, M. N. Ducea, G. E. Gehrels, M. R. Cecil, M. E. Rusmore, G. J. Woodsworth, D. M. Pearson, C. Manthei and P. Wetmore (2012), Elemental and isotopic evidence for granitoid genesis from deep-seated sources in the Coast Mountains Batholith, British Columbia, *Journal of Petrology*, 53(7), 1505-1536.
- Heah, T. ST. (1991), Mesozoic ductile shear and Paleogene extension along the eastern margin of the Central Gneiss Complex, Coast belt, Shames River area, near Terrace, British Columbia, *University of British Columbia Masters thesis*.
- Hill, M. L. (1985), Geology of the Redcap Mountain area, Coast Plutonic Complex, British Columbia, *Princeton Univ., Ph.D dissertation*.
- Hill, M. L. (1985), Remarkable fossil locality: Crinoid stems from migmatite of the Coast Plutonic Complex, British Columbia, *Geology*, 13(11), 825-826.
- Hollister, L. S. (1982), Metamorphic evidence for rapid (2 mm/yr) uplift of a portion of the Central Gneiss Complex, Coast Mountains, BC, *The Canadian Mineralogist* 20(3), 319-332.
- Hollister, L. S., and C. L. Andronicos (2000), The Central Gneiss Complex, Coast Mountains, British Columbia, *Geological Society of America Special Papers*, 343, 45-60.
- Hollister, L. S., and C. L. Andronicos. (2006), Formation of new continental crust in Western British Columbia during transpression and transtension, *Earth and Planetary Science Letters* 249(1), 29-38.
- Irving, E., P. J. Wynne, D. J. Thorkelson, P. Schiarizza. (1996), Large (1000 to 4000 km) northward movements of tectonic domains in the northern Cordillera, 83 to 45 Ma, *Journal of Geophysical Research: Solid Earth*, 101(B8), 17901-17916.
- Klepeis, K. A., M. L. Crawford, and G. E. Gehrels. (1998), Structural history of the crustal-scale Coast shear zone north of Portland Canal, southeast Alaska and British Columbia, *Journal of Structural Geology*, 20(7), 883-904.
- Ludwig, K. (2001), Isoplot/Ex 2.49, A geochronological toolkit for Microsoft Excel, *Berkeley Geochronology Center, Berkeley, CA. Special Publication*.

- MacLeod, D.M., and Pearson, D.M., 2014, Protolith age of metamorphic rocks in the roots of a continental magmatic arc link retroarc lithosphere underthrusting to high flux magmatism: the Central Gneiss Complex, British Columbia, Canada, *American Geophysical Union Abstracts*, #V33B-4848.
- Marsden, H, and D. J. Thorkelson (1992), Geology of the Hazelton volcanic belt in British Columbia: implications for the Early to Middle Jurassic evolution of Stikinia, *Tectonics* 11(6), 1266-1287.
- Monger, J. W., R. A. Price, and D. J. Tempelman-Kluit (1982), Tectonic accretion and the origin of the two major metamorphic and plutonic belts in the Canadian Cordillera, *Geology*, 10(2), 70-75.
- Passchier, C. W., and R. A. Trouw (2005), Microtectonics, *Springer Science and Business Media*.
- Roddick, J. A. (1970), Douglas Channel-Hecate Strait map-area, *British Columbia: Geological Survey of Canada Paper*, 70-41.
- Rosenberg, C. L., and H. Stünitz (2003), Deformation and recrystallization of plagioclase along a temperature gradient: an example from the Bergell tonalite, *Journal of Structural Geology*, 25(3), 389-408.
- Rusmore, M. E., G. J. Woodsworth, and G. E. Gehrels (2005), Two-stage exhumation of midcrustal arc rocks, Coast Mountains, British Columbia, *Tectonics*, 24(5).
- Spear, F. S., and J. T. Cheney (1989), A petrogenetic grid for pelitic schists in the system SiO<sub>2</sub>-Al<sub>2</sub>O<sub>3</sub>-FeO-MgO-K<sub>2</sub>O-H<sub>2</sub>O, *Contributions to Mineralogy and Petrology*, 101(2), 149-164.
- Stipp, M., H. Stünitz, R. Heilbronner, S. M. Schmid (2002), The eastern Tonale fault zone: a 'natural laboratory' for crystal plastic deformation of quartz over a temperature range from 250 to 700 C, *Journal of Structural Geology*, 24(12), 1861-1884.
- Van der Heyden, P. (1992), A Middle Jurassic to early Tertiary Andean-Sierran arc model for the Coast Belt of British Columbia, *Tectonics*, 11(1), 82-97.
- Woodsworth, G. J., W. D. Loveridge, R. R. Parrish, and R. W. Sullivan (1983), Uranium-lead dates from the Central Gneiss Complex and Ecstall pluton, Prince Rupert map area, British Columbia, *Canadian Journal of Earth Sciences*, 20(9), 1475-1483

## **8. Appendix**

### **8.1. Methods**

#### **8.1.1. Field work**

The field location is both remote and rugged such that it is only accessible via helicopter and with mountaineering equipment suitable for ascending or descending excessively steep terrain as well as completing traverses across glacial terrain. We completed all field work above the treeline in order to avoid outcrop-obscuring vegetables and other complications relating to the temperate rainforest. This includes preparing for and avoiding potentially hostile wildlife. All observations therefore are based on exposures above 3000 feet in elevation.

We undertook mapping, structural analysis, and sample collection in the field area with a focus on the contact between the Rusty and Gray weathering units. This included a detailed analysis of a section of the gray weathering gneiss from the lower elevations to the base of the contact. All field locations are numbered and documented with their GPS coordinates. We collected hand samples from 13 different locations for a mixture of U-Pb zircon geochronology, microstructure analysis, and phase composition. Oriented samples were measured and documented in situ before being removed.

All field measurements are displayed in strike and dip format and are documented in the attached table. We plotted structural data including foliation orientations, fold axis, lineations, and foliations on a stereonet (Figure 9, Figure 10). Planar measurements were converted to poles to assist interpretations and to reduce clutter. Representative measurements and unit boundaries are displayed on a map of the field area modified from Hill (1985) PhD (Figure 5).

### **8.1.2. Thin sections**

Thin sections were prepared from collected samples and used to document and confirm field identification and interpretations. Oriented samples for microstructural analysis were cut parallel to lineation and perpendicular to foliation in order to best assess shear structures and other fabrics. Arrows were etched onto the slides to preserve orientations. We estimated temperatures of deformation in quartz and feldspar using descriptions of solid-state deformation temperatures, documented in Passchier and Trouw, (1996) and Stipp et al. (2002), and compared mineral assemblages to previous research published by Hill (1985) PhD dissertation.

### **9.1.3. U-Th-Pb geochronology**

We applied Laser Ablation Inductively Coupled Plasma Mass Spectrometry (LA-ICP-MS) to analyze the geochronology of four samples from the field area using methods described by Gehrels et al, (2008). These samples were obtained and documented in the field, as well as examined in thin section to aide in the interpretations. Zircons were separated from their host rocks at Idaho State University using a Braun Chipmunk jaw crusher and disc mill, Wilfley shaking table, Frantz magnetic separator, and methylene iodide. Zircons were hand picked and mounted for igneous samples and randomly selected for detrital mounts. We then used a Gatan miniCL Cathodoluminescence (CL) detector attached to a scanning electron microscope to produce detailed images of grain textures that were later used for spot placement and interpretations. We analyzed and displayed data using the Isoplot program developed by Ludwig (2001). We rejected analyses when laser pits were suspected to sample multiple age domains observed using CL imagery, or contains contamination from possible inclusions. Data from the clastic

sedimentary samples is displayed on probability density plots. Metamorphic and detrital ages are distinguished by plotting the laser ablated spot on the CL images and comparing them to both the measured age and the Uranium-Thorium ratio. The igneous sample results are displayed with the age and error bars from individual measurements as well as an age calculated from their distribution. We distinguished and removed mixed ages that included inherited cores or metamorphic rims by comparing the measured data with the CL images.

#### **8.1.4. Lead loss in zircons**

The rocks in the Central Gneiss Complex underwent granulite facies equivalent conditions and thus the role of lead diffusion in zircon may be called into question. The rate of Pb loss in zircon is discussed in [Cherniak and Watson, 2000]. The diffusion rate of lead in zircon is dependent both on the length of the time certain conditions were observed and, to a greater extent, the temperatures those rocks underwent. Significant lead loss in zircon in the outer several microns of the grain, and with a time scale of tens of millions of years, begins somewhere between 800 and 850°C. Below these temperatures, lead diffusion in zircon is negligible. While this may be a factor in a few select locations, the peak metamorphic conditions recorded in the before-mentioned samples is between 750 and 800°C. The significant variation between the samples is more likely caused by an undocumented stratigraphic or structural contact between the two localities.

#### **8.2. Thin section descriptions**

See Figure 12 and Figure 13 for thin section textures.

Sample 03: (54.730733, -129.726017) We recovered this sample from a location



of the gray gneiss that we field identified to have a graded bed structure. Medium grained, equigranular, quartzo-feldspathic gneiss containing ~50% 0.2-0.5 mm quartz, 35-40% 0.2-0.5 mm plagioclase, 5-10% biotite which defines the foliation, and <5% potassium feldspar. Quartz shows evidence of crystal-plastic deformation through Grain Boundary Migration (GBM) and is partially reset to 120 degree triple junctions.

**Sample 26:** (54.73155, -129.7332) This sample was collected from a foliated dike that visibly crosscuts a meter-scale recumbent fold. Quartzo-feldspathic gneiss with relict plagioclase porphyroclasts up to 5 mm in diameter with igneous zoning textures in a finer matrix of 40% quartz, 3-5% biotite, and 45-50% plagioclase. Biotite defines the foliation. Visible GBM of quartz suggests strain and recrystallization temperatures greater than 550°C [Stipp et al., 2002] and is overprinted by a partial resetting texture. Biotite orientations within the finer matrix, undulose extinction of quartz, and dynamic recrystallization points to a tectonic origin of the fabric.

**Sample 32:** (54.72585, -129.74105) This sample was collected from the shear zone. Fine grained quartzofeldspathic gneiss with evidence for recrystallization and recovery to 120 degree triple junctions. Undulose extinction in quartz is seen in coarse, elongated ribbons that exhibit GBM. Some biotite is present in the matrix. The foliation orientation is identified through the quartz textures. 50% Quartz, 45-50% plagioclase, 1-3% biotite, 1% > hornblende.

**Sample 44A/B:** (54.749567, -129.769983) This sample was collected from the cataclasite found in the amphibolite layer of the rusty-weathering gneiss. Deformed biotite – quartz, plagioclase, cataclasite containing 30% 0.01 – 3mm biotite, 45% 0.1-0.4 mm quartz, 0.1 – 0.5 mm plagioclase, 2-8% chlorite. Quartz is found in 0.5-1 centimeter

thick layers that contain elongated coarse grained ribbons which exhibits Sub Grain Rotation (SGR) as the primary method of dynamic recrystallization. These layers contain biotite spaced throughout them that defines the foliation. Deformed biotite also mantles rotated plagioclase clasts, forming an S-C fabric and mica fish. In specific locations, discrete plains of very fine biotite form a continuous layer across the sample parallel to the foliation. In some locations, biotite is partially to completely altered to chlorite. The fabric points to a top the west sense of shear. Plagioclase has localized evidence of dynamic recrystallization.

**Sample 45:** (54.747417, -129.770133) This sample was collected from the eastern edge of the Lluvia Peak pluton. Coarse-grained granoblastic granodiorite with minor sericitic alteration of plagioclase (albite). 50-60% 1-3mm plagioclase, 20-30% 1-2.5mm quartz, 5-10% 1-10mm biotite, 10% > potassium feldspar and hornblende.

**Sample 47:** (54.75005, -129.771617) This sample was collected from a felsic dike that crosscuts the shear zone. Medium grained granoblastic granodiorite containing 25% 0.5-1.5mm quartz, 50% 0.5-1.5 mm plagioclase (albite), 5-10% 1-2mm hornblende. Biotite is present, but makes up less than 1% of the sample. Minor sericitic alteration of the plagioclase is present.

**Sample 48:** (54.737433, -129.8112) This sample was collected from a strained pebble conglomerate from the gray gneiss. Medium grained equigranular, Quartzofeldspathic metamorphosed pebbled conglomerate, containing ~ 10-15% biotite, ~70% quartz, ~10% plagioclase in the matrix. The clasts are distinguished visibly by its larger grain size, and containing only ~5% biotite, but similar proportions of other phases. Quartz exhibits GBM and partial resetting to 120 triple junctions.

**Sample 50:** (54.74265, -129.787133) This sample was collected from a garnet-bearing section of the shear zone exposed on the north face of Lluvia Peak. Fine grained quartzo-feldspathic gneiss with 2-6mm garnet porphyroblasts and 5-10 mm thick coarse grained quartz ribbons. Contains 45% quartz, 3-5% biotite, 40-45% plagioclase, 4% > garnet. Biotite is fine-grained and aligned with the foliation. Minor pressure shadows are preserved on one edge of the garnet, but is otherwise recrystallized.

**Sample 52:** (54.747367, -129.76985) This sample was collected from the lower amphibolite unit in the rusty weathering gneiss. Quartz-biotite-plagioclase gneiss with porphyroblastic garnets up to 10mm in diameter. Contains ~ 60% 0.5-1 mm quartz, 25% 1-2mm biotite, 5-10% 0.5-1 mm plagioclase, 5% > garnet. The foliation is defined by aligned biotite up to 2 mm across. The quartz-feldspar matrix is partially to completely recovered to form a granoblastic texture.

**Sample 53:** (54.7454, -129.769667) We collected this sample from pelitic layer within the rusty weathering gneiss and contains a microprobe polish that may be utilized for future work. The sample is a medium grained porphyroblastic quartz – sillimanite - biotite, garnet gneiss with up to 5% plagioclase. Tabular sillimanite and biotite define the foliation and wrap 1-3mm inclusion – rich garnets. The sillimanite is not associated with any identifiable potassium feldspar, and there is no visual evidence for partial melting in the hand sample or in thin section. The sillimanite is not seen as inclusions in the garnet.

In reflected light, opaque minerals have a coppery core with a tan metamorphic rim of ilmenite. These rims are present within the garnet inclusions as well as the matrix.

**Sample 54:** (54.745567, -129.7693) This sample was collected from a coarse quartz-rich sample within the Rusty Gneiss. Medium-grained granoblastic calcareous

quartzite with gneissic banding defined by enstatite and diopside. ~ 35% quartz, 20% plagioclase, 35% enstatite + diopside, and up to 3% titanite. Centimeter scale folds are present on the slide, but are not texturally distinguishable under magnification. The quartz and feldspar have been recovered with little to no metamorphic texture preservation. Grain size of each mineral varies from 1-3mm in diameter.

### **8.3 CL descriptions**

**Sample 26:** This sample was retrieved from a deformed felsic dike that crosscut a meter-scale recumbent fold. The grains are euhedral, with no evidence of fracturing or rounding. The images show a zoned igneous growth pattern that forms most of the grains interior (Figure 14). Grain shape varies from squat zoned forms to elongate grains that contain a distinct linear zoning pattern at their center and a more homogeneous pattern at their tips and sides. Grain size is generally between 100 and 150 microns in length, with a few smaller outliers.

The igneous zoning is commonly split up into two distinct domains: the core and rims. The cores are distinguishable texturally from rims by brightness, changes in zoning pattern, and truncation of specific zones. I identified no distinguishing characteristics common across the cores. The cores make up some portion of the sample and are sometimes euhedral in shape, but often are rounded as if from dissolution prior to growth. The sample rims tend to be composed of a single outer zoned layer that distinctly defines the euhedral shape. The visibility of the igneous zones is limited by contrast changes between the layers and thickness of the rim. A few of them have no visible igneous zoning pattern at all. In some grains the boundary between the rim and core is difficult to identify, and in some of the smaller grains, is not present at all.

**Sample 45:** We retrieved this sample from the Lluvia Peak pluton on the northeast dipping ridge ~ 20 m from the pluton edge. This sample is similar in appearance to sample 26, and contain large euhedral grains, each with a distinct igneous zoning pattern and have little evidence for rounding or dissolution of the outer grain boundaries. More elongate grains are common and contain visibly distinguishable core-rim domains. The cores tend to be rounded in shape with more significant dissolution textures occurring on the ends of the grain and less dissolution or growth along the sides. Cores also tend to be smaller in relation to the rims, but vary significantly from grain to grain. In some grains the igneous growth pattern is continuous to the edges with no visible core-boundary relationship. Grain size varies from 100-150 microns in length.

**Sample 48:** We retrieved this sample from a stretched pebbled conglomerate unit directly beneath the shear zone of the rusty weathering gneiss. The zircon grains in this sample are immediately distinguishable by their complex irregular form and from their internal compositional structure. Grains tend to lack the elongate shape and distinct igneous zoning of samples 26 and 45, as well as contain a more varied grain size. The largest grains are on the order of 150 microns, but are wider than the elongate grains of the igneous samples, while the smallest are on the order of ~50 microns and sometimes contain a banded igneous zonation pattern that is otherwise overprinted and missing from the rest of the grains.

Complex dissolution, zoning, and growth can be seen in (Figure 14). In nearly all the samples, a clearly visible, but otherwise complex core is present. The grains commonly display sector zoning, patchy zoning, and extensive visible dissolution of grain boundaries. While interpretations on how exactly these textures form is debated

[Corfu et al., 2003], they are likely related to exposure and growth during high-grade metamorphic events or exposure to partial melts. In many of these grains, we observed up to three layers with truncated growth zones and dissolution. The cores with the pitted dissolution textures are almost always overprinted by a later domain of homogeneously textured growth that forms straight grain boundaries and edges. While the grains themselves tend not to be rounded in appearance, the shape and overall form of the grain is defined by extent and shape of the irregular core.

**Sample 54:** This sample was taken from a coarse grained, calc-silicate-rich quartzite within the rusty weathering gneiss. The zircon grains and form are very similar to that of sample 48 with largely variable grain size (50-150  $\mu\text{m}$ ), odd shapes, complex zoning and common heavy dissolution patterns. The number of zircons we recovered, retrieved and measured was significantly more than that of the pebble conglomerate. While individual periods of growth and dissolution is difficult to identify within the cores of the grains, many of the grains exhibit a thin homogeneous rim that is distinct and otherwise unaltered. Sector zoning and patchy zoning is present throughout most of the grains and across various domains.

## **8.4. Geochronology**

### **8.4.1 Mean Square Weighted Deviation**

The Mean Square Weighted Deviation (MSWD) is used to provide a numerical value for closeness of fit to a standardized unimodal distribution of ages and is based on the measured instrumental error for each sample. A MSWD of 1 represents a good fit within the calculated ages ranges. A MSWD of  $<1$  means that the scatter of data points is small in relation to the analytical uncertainties, such that the error bars on each measurement are much larger than what the scatter of points may suggest. The

uncertainties of the measurements are likely to be overestimated. A MSWD of  $>1$  means that the scatter of the data points is much larger than what would be possible within the individual error bars. This means that either the errors for each measurement were underestimated, or the data points do not represent the error scatter of a single value or age, but rather a distribution of ages themselves. The MSWD is therefore a method that assumes a unimodal distribution and can be used to assess error estimates or the applicability of an igneous origin to an uncertain protolith.

#### **8.4.2 Igneous statistics**

For the igneous samples the data averages for the igneous samples were plotted using the Isoplot program plugin for Microsoft Excel 2003. All age ranges are drawn with a two standard deviation error sensitivity. Error bars range significantly for each age and is related to changes of elemental compositions both within and between samples. We chose each spot to receive the clearest result from each grain, and as previously mentioned, removed data points that contained significant measuring errors or impossible ages.

**Sample 26:** We plotted the zircon ages with their respective spot size and grain location for each analysis to aide in interpretations. For this sample, we imaged the cores using the 25um spot size. The zircon cores, were present, vary between 180 and 220 Ma in age and are significantly older than the zoned rims. This is evidence for the cores to be xenocrystic – and were derived from some form of crustal melt. The dissolution textures evidence by the rims of these grain boundaries provides further evidence for this process as existing grains interact with the surrounding melt. The rims with the igneous zonation pattern therefore reflect cooling of the dike. The smaller rim size in comparison to the

pluton may either be a result of cooling rates, or melt composition. Ages we retrieved for the rim domains of this sample tend to be between 76 and 83 Ma and likely reflect a crystallization age for the melt.

I plotted the ages for sample 26 using the Isoplot program (Figure 18) by separating out core and mixed ages from the data set in order to calculate an accurate value for the timing of melt crystallization. The age calculated from this sample is  $78.5 \pm 2.6$  Ma with a Mean Square Weighted Deviation (MSWD) of 6.7. This age represents the crystallization age of the grain rims, and therefore cooling of the melt - as is suggested by textural data from the CL images. The MSWD of 6.7 is much higher than expected and suggests that the calculated errors are either significantly underestimated, or that some of the ages may contain a small amount of domain mixing which would either increase or decrease the calculated age. This mixing will be magnified by the few ages measured ( $n = 15$ ), and may reflect previously unidentified growth domains. The presence of a  $64.1 \pm 4.9$  Ma mixed age from the very outer rim of one of the grains points to the presence of a very weak, late period of zircon growth. 48-52 Ma metamorphic rims are common in the metasedimentary samples (see the metasedimentary sample statistics section) and may be the culprit. Either way, the overall change in the calculated age is minimal, and the increased error is seen in the 2.6 Ma error bars. In addition, all of the ages used for the age calculation are concordant.

There were not enough core ages to produce an accurate probability density plot for sample 26, however most of the ages measured were found to form a normal distribution around 200 Ma. U/Th ratios of the different grains vary significantly when measured within the rims, and range from as low as 0.7 up to as high as 23.7. There is no



other obvious spatial relationship or correlation to this pattern. The cores, however, contain consistently low U/Th ratios of  $<2.0$ , with the exception of the upper age outlier of 276 Ma, at 3.6. This may represent fluctuations of uranium and thorium availability during melting of the host rock and crystallization of the grain.

**Sample 45:** Sample 45 cores provide a similar age distribution to those found in the felsic dike. Core ages vary between 170 and 260 Ma and likely represent relict xenocrystic cores that experienced early dissolution during melting of the sample, followed by a period of later crystallization. The rims were dated to be between 76 and 86 ma. There are several ages that lie between the younger rim and older core age populations and are interpreted from analysis of the cl images to be mixed ages. The younger grain ages are attributed to mixing with a thin metamorphic rim where the ablation spot overlapped the two domains either spatially, or through the grain.

The age and error range for each data point was plotted using the Isoplot plugin. I omitted ages identified from the age data and from the CL images as being from the grain cores, mixed ages, or containing excessive error on the measurement. I then calculated the average age from these remaining grains in order to reflect the crystallization age of the zircon rims. The final age calculated is  $80.2 \pm 1.0$  Ma, with a MSWD of 0.98. The MSWD of 0.98 means that the data points fit a distribution that agrees with the calculated errors for the sample. It provides a good fit for error distributions around a single age. The errors and measurements for both 26 and 45 were done concurrently and represent the same calibration and method for determining errors in measured ages. The errors of the two samples are therefore similar. For future work, collecting additional samples from the field for a more robust age of the dike may be useful, but the age and related error of

$78.5 \pm 2.6$  Ma for sample 26 is sufficient for this discussion. It is important to note that the ages of  $80.2 \pm 1.0$ , and  $78.5 \pm 2.6$  are indistinguishable from each other.

Zircon core ages for sample 45 follow a similar normal distribution to what we observed in sample 26, and their distribution lies between 180 and 230 Ma in age. It was likely sourced from a similar unit or lithology. U/Th ratios for this sample are generally higher in the rims and vary significantly from measurement to measurement. Most lie within the range of 5 to 15, with a few outliers above this. Core U/Th ratios are uniformly lower and vary between 0.4 and 2.5. The higher ratio may be a result of mineral growth and melting during migmatization and crystallization of the melt.

#### **8.4.3. Sedimentary statistics**

The cores of the individual grains were systematically analyzed to remove as much measurement bias as possible, however the complexity of the grains and domains therein force some amount of intrinsic bias related to choosing the spot location. For the purpose of the discussion, and from analysis of the spots, the grain cores are assumed to consist of a single domain and will represent grain age and interpreted sourcing. Other methods such as the concordia diagrams, and plots of the averages are used in the results and interpretations of the two samples. This includes the MSWD of the age distribution and comparison to unimodal igneous sources.

**Sample 48:** We dated sample 48 exclusively with the 12micron spot size for greater accuracy within the smaller domains. The homogeneous rims of the zircons gave us consistent ages of between 48 and 55 ma that lie within standard error of each other and can be compared to the 80 Ma rims seen in the igneous samples. These rims contrast with the cores which vary between 180 and 210 years of age. Individual measurements

within specific, complicated cores most commonly contain indistinguishable ages from each other, although some exceptions do occur. All of these exceptions, however, are older than the 170 Ma measurements and may either represent contamination of results due to minor inclusions, or an early event experienced by those grains prior to cooling and erosion into the conglomerate.

A histogram of the measured age distributions are plotted in (Figure 20) and contains all of the ages of the grains and the rims. The most significant peak of ages falling between the 180 and 210 range are the ones taken from the interior of the altered grains, while the secondary peak at 50 Ma represents the measurements from the homogenous rims. The few ages that fall between them are likely mixed ages, and closer examination of the CL images suggests that this is indeed the case. All of the ages with a few exceptions are concordant (Figure 22) and contain a reasonable uncertainty - giving no evidence for lead loss through diffusion due to high grade conditions.

I also plotted a probability density plot of the largest peak of ages from between 180 and 210 Ma (Figure 21). First glance suggests that this is indeed a normal distribution of ages expected from a single grain age or source. However, a closer examination of individual errors shows that the unimodal spread of ages is much larger than the error bars would allow for a single age population. To further show this, the MSWD calculation for these ages provided a value of 13. This means that either the sample did not originate from a single population, or the errors for each measurement are greatly underestimated. Field observations of a stretched pebble conglomerate point to the former being correct. It's more likely that the conglomerate was instead locally sourced (see protolith discussion section of manuscript)

All of the rims give ages of 48-55 Ma, with ages of 80 Ma not present at all. U/Th ratios vary between 17.5 and 250 for these ages, while the cores contain ratios between 1 and 5, and likely represent changes in element availability during growth. Further evidence for these as metamorphic rims stem from their anomalous, homogeneous form, and the overall subhedral appearance of the grains.

**Sample 54:** We also dated sample 54 exclusively with the 12 um spot size for more accurate positioning of the ablation spots. The zircons gave varying ages based on spot location, and similar to sample 48, can be broken up into the main core and the rim domains. The homogeneous rims gave ages between 48 and 55 Ma, and the grain cores gave ages that vary from 170 to 210. On several grains, multiple measurements were made of the same core where we observed textural variations within them. In all cases this textural differences resulted in the same age, with one exception where the center and outside of the grain yielded an age of 193 Ma, while the middle rim yielded an age of 247.6. Unless the older age represents the skeletal husk of a mostly dissolved grain prior to the zoned zircon growth, the older age is likely a result of a small inclusion or other interference with the age – although the error range is still reasonable.

Figure 20 represents a histogram of the ages from each measurement. A single large peak is visible between 170 and 210 Ma, while the rest of the ages are spread between this and around 50 Ma where a second smaller peak is visible. The unimodal peak between 170 and 210 is similar in appearance to the one described in sample 48, but is distinctly shifted to the left (younger) by several million years. This is more evident in the probability distribution plot across the peak. This sample contains a small yet significant population of ages that lie between 170 and 180 Ma not visible in the previous one. The

ages for this sample are mostly concordant (Figure 22), and are unlikely to have experienced significant lead loss through diffusion.

I plotted the probability density for the large peak of sample 54 in (Figure 21). This distribution follows a near-unimodal peak with a small secondary peak between 170 and 185 Ma. This small increase in probability does not appear in the sample 48. This smaller peak may be dismissed to chance - as the main peak still follows a normal distribution - however the younger population does exist uniquely. The MSWD for this normal distribution is on the order of 15, such that it is unlikely that this sample represents a single age population, but a spread as would be expected from a deformed quartzite. There is a lack of older ages in this sample which gives some implication for its broader depositional environment.

Similar to sample 48, all of the rims give ages between 48 and 55 and are marked by an increase in their U/Th ratios. These ages, or rims, from the two samples are likely related to the same event.

## 8.5. Figures

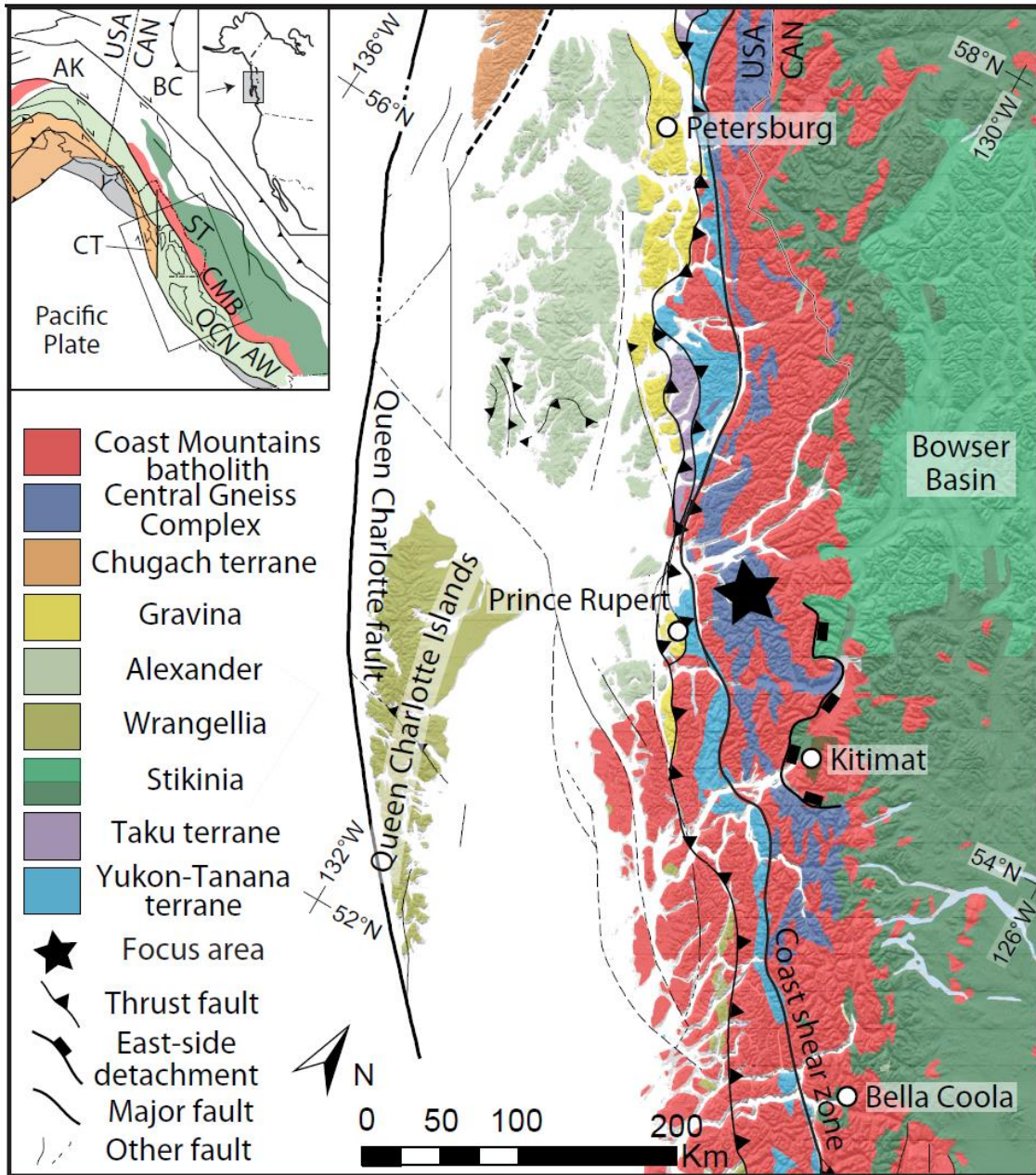


Figure 1: Index map of western British Columbia showing study area in the context of major terrane boundaries and faults [modified from Wheeler and McFeely, 1991 and Gehrels et al., 2009]

<p style="text-align: center;"><b>Stikinia</b></p>	<p>Stikinia is located to the east of the Central Gneiss Complex and is separated from the latter by the Shames River mylonite. Stikinia includes a composite of Paleozoic and early Mesozoic volcanic rocks that are overlain by Jurassic volcanic rocks of the lower Hazelton Group, siliciclastic rocks of the middle and upper Hazelton groups, and Cretaceous marine sediments of the Bowser basin [Marsden and Thorkelson, 1992]. Shortening in the Skeena fold-thrust belt in these sediments requires a minimum of 160 km of retroarc underthrusting beneath the batholith [Evenchick et al., 2007].</p>
<p style="text-align: center;"><b>Alexander terrane</b></p>	<p>The Alexander terrane is located directly to the west of the Central Gneiss Complex where the Coast shear zone forms the contact between the two near the latitude of Prince Rupert. The Alexander terrane consists of Proterozoic and Paleozoic rocks as well as Triassic-early Jurassic sediments [Gehrels et al., 1987]. Paleomagnetic data suggest that many of the rocks were deposited near the equator where it collided with Wrangellia during the late Paleozoic to form the Insular superterrane. This terrane comprises a large portion of western British Columbia and Alaska. Accretion of this terrane with western North America occurred during the Cretaceous.</p>
<p style="text-align: center;"><b>Yukon-Tanana terrane</b></p>	<p>The Yukon-Tanana terrane is located in northern British Columbia, east-central Alaska, and western and central Yukon [Mortensen et al., 1992]. It is composed of continental volcanic arc sediments that were deposited in three pulses during the Devonian-Mississippian, Permian, and Triassic-early Jurassic. It also contains marine sedimentary rocks deposited at the margin. Triassic and Permian magmatism and deformation is correlated to terrane and collisional events at an active convergent margin.</p>

Figure 2: The context of each terrane is described in consideration as a possible protolith of the Central Gneiss Complex. See Figure 1: for terrane locations in map view.

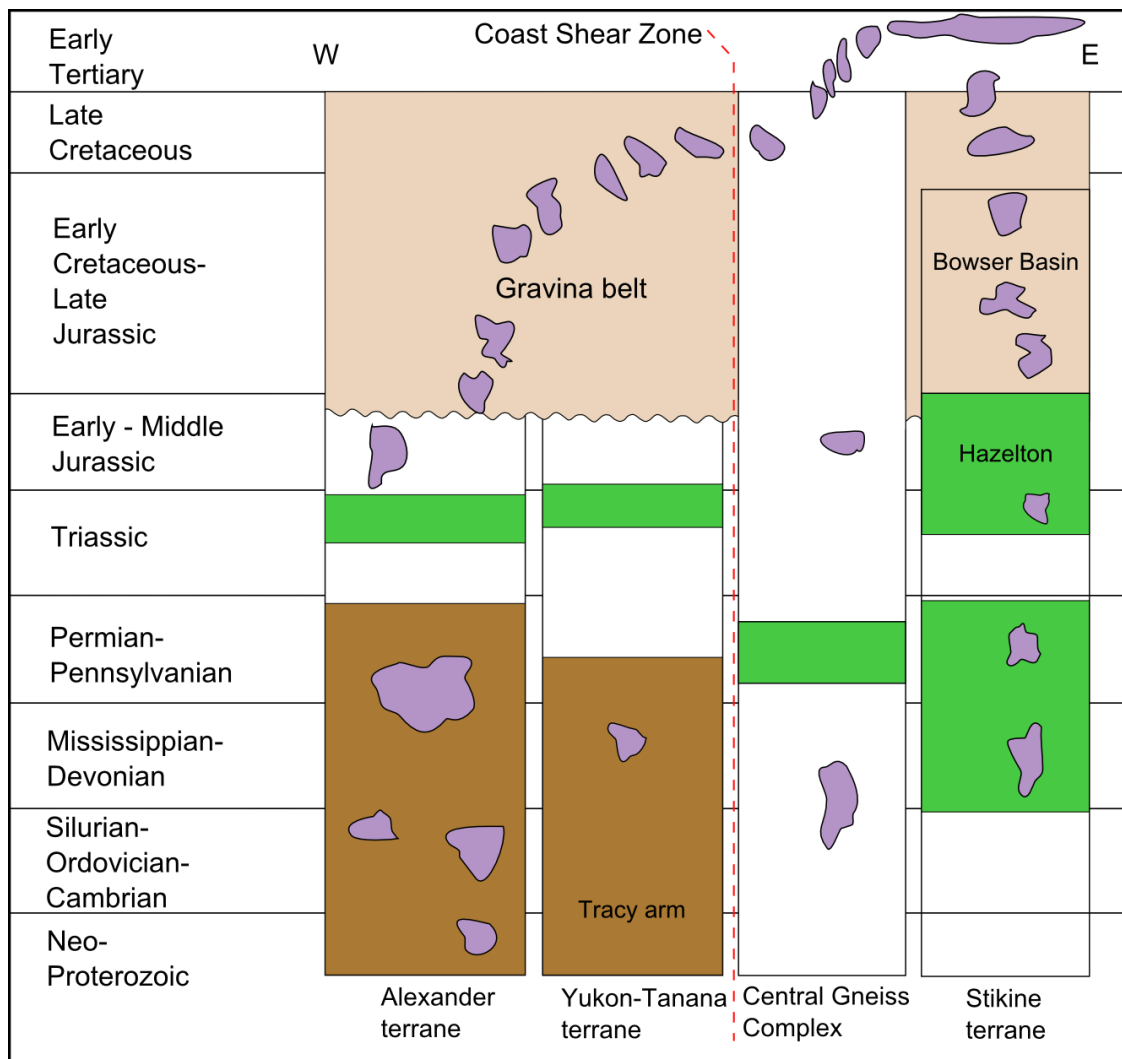


Figure 3: Schematic W-E view showing terrane lithologies and ages. From Gehrels et al. [2009], this figure shows the lithologies of the Insular, Yukon-Tanana, and Stikine terranes and associated structures. See Figure 2 for descriptions.



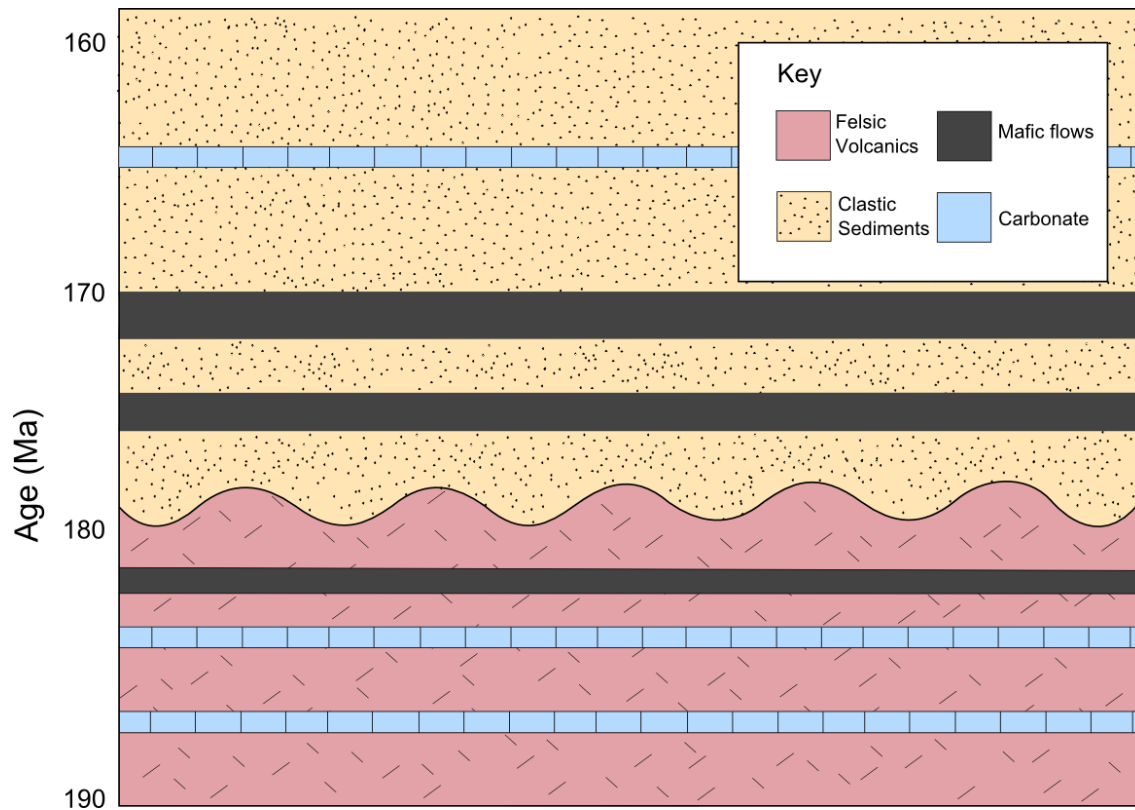


Figure 4: Schematic lower and middle Hazelton Group stratigraphy. The lower Hazelton Group is an isotopically homogeneous sequence of felsic volcanic rocks with thin carbonate interbeds and occasional mafic lava flows. The middle Hazelton Groups overly the lower Hazelton and consist of clastic sediments, thick mafic flows, and some carbonate units. The middle Hazelton Group is variable in timing and composition along-strike, and represents a trough between two volcanic arcs [Gagnon et al., 2012].

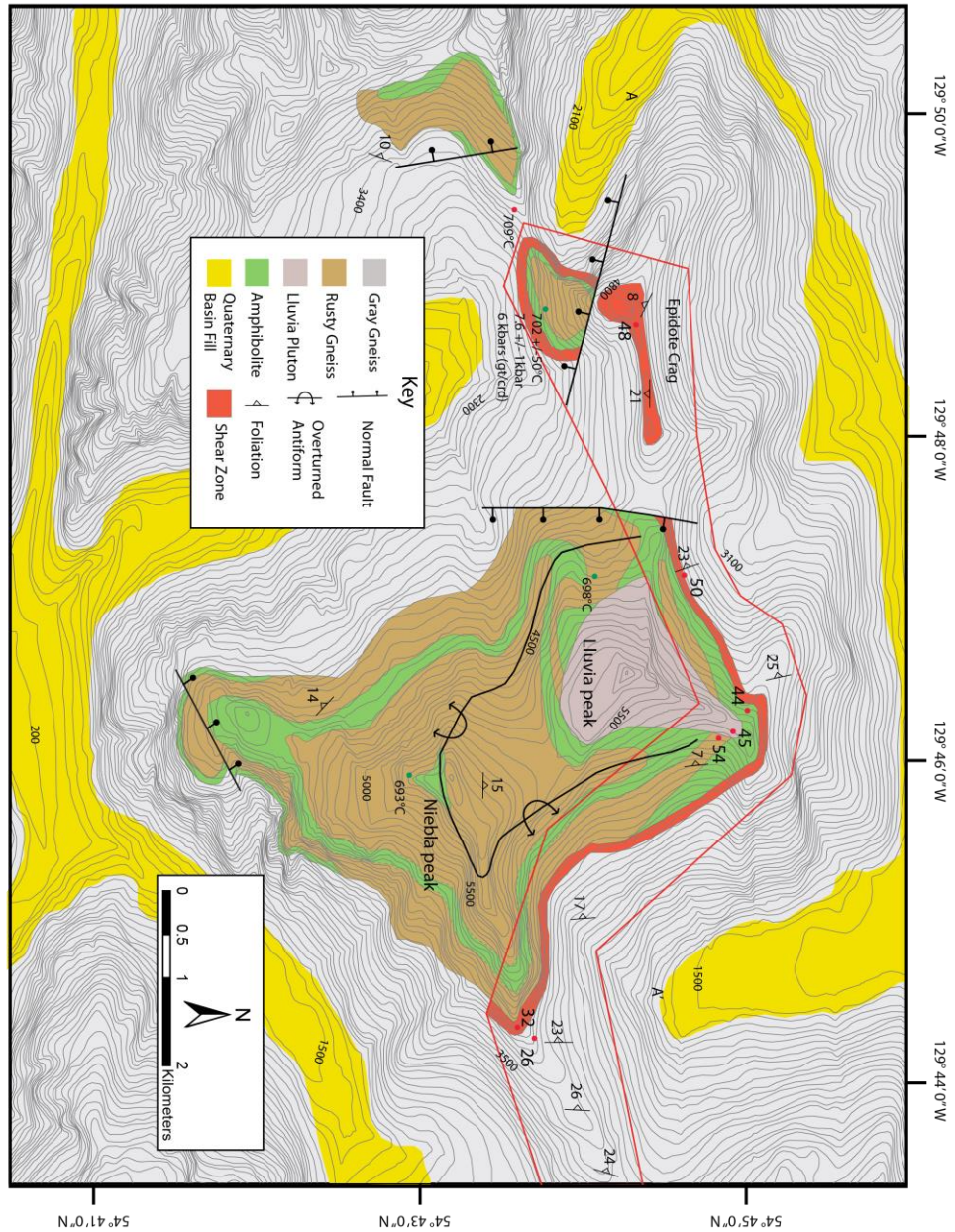


Figure 5: Bedrock map showing foliations, normal faults, and large folds within the Lluvia Peak field area. The gray gneiss is undifferentiated in this area. The red line represents the boundary of the area described by this manuscript. Relevant field stations discussed in the text are labeled.

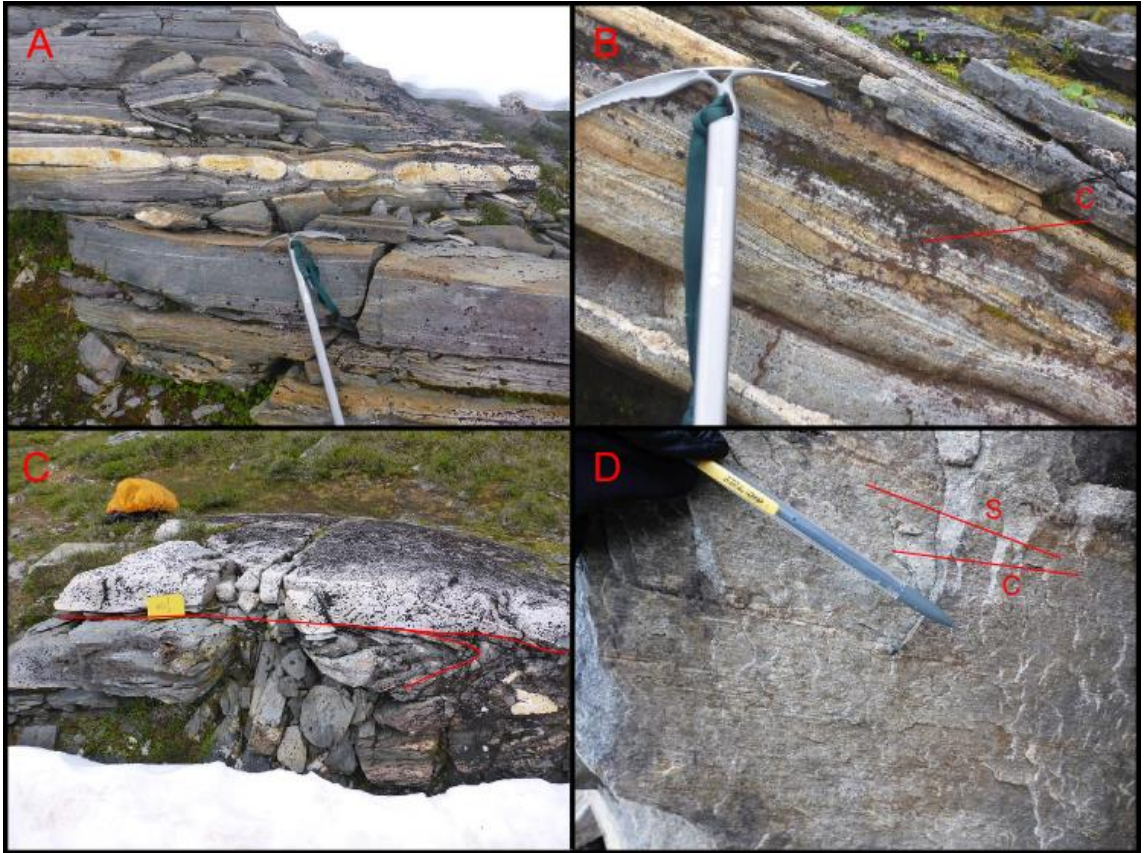


Figure 6: Examples of structures from the gray weathering gneiss on the eastern side of Lluvia Peak. A) Boudinage of a weakly foliated felsic dike. B) S-C shear bands in the lowest exposed portion of the gray gneiss. C) A foliated felsic dike crosscuts a tight recumbent fold at field station 26. D) S-C fabric visible in the shear zone.





Figure 7: Examples of common structures exposed in the gray gneiss include: A) deformed amphibolite unit 20 m beneath the shear zone; B) cm-scale isoclinal folds with transposed limbs; C) boudinage of thick felsic dikes and compositional layers; and D) parasitic folds commonly found near the hinge of the larger recumbent structures.



Figure 8: Field photographs from the rusty gneiss and epidote crag. A) Dextral (top to the west) slip within the cataclasite zone is evidenced by an offset felsic dike. B) Stretched pebble conglomerate from the base of the shear zone. C) Complex folding in a calcsilicate layer of the rusty weathering gneiss. D) Contact between the Lluvia Peak pluton and a biotite rich layer of the rusty gneiss.

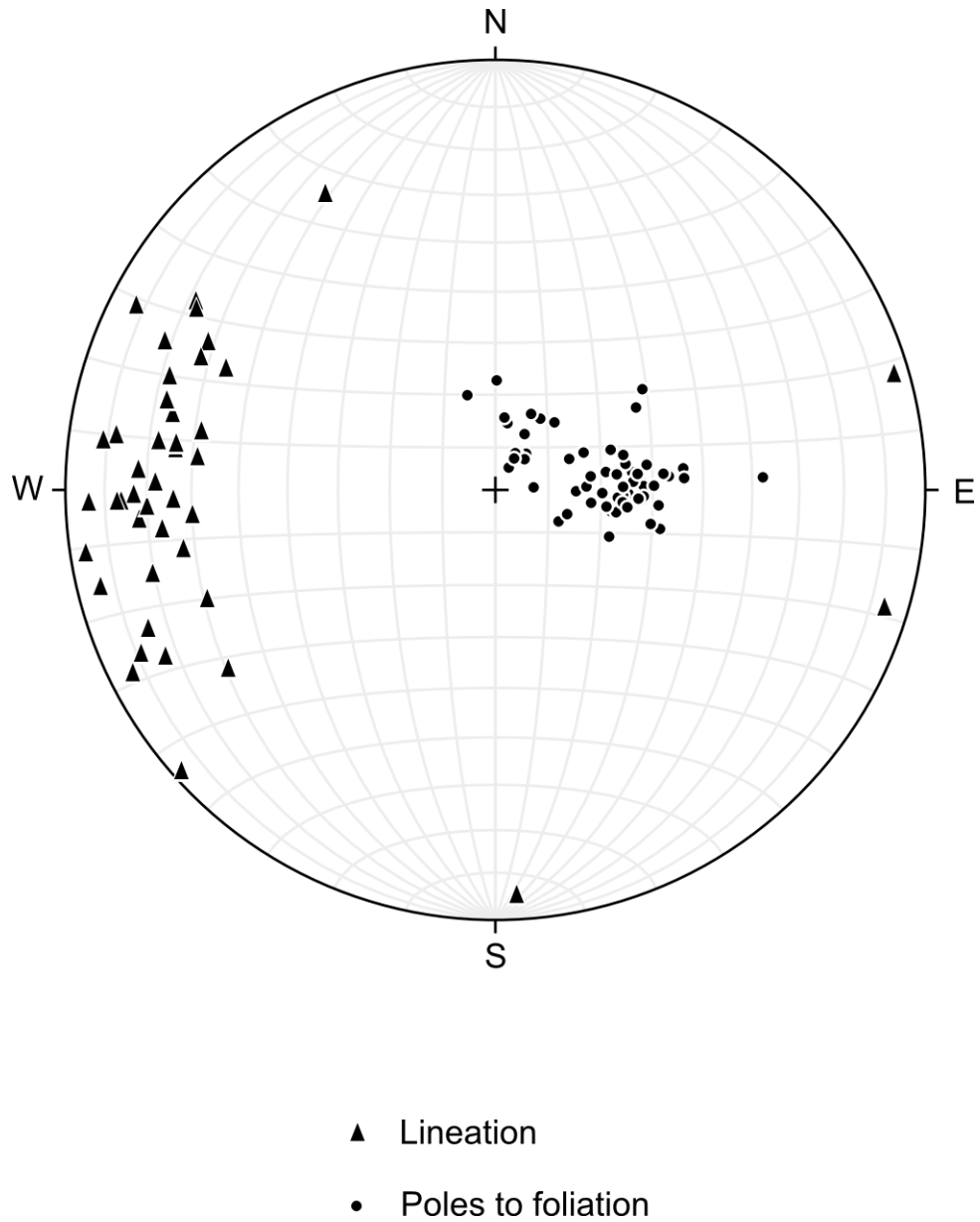


Figure 9: Stereonet showing poles to foliations and lineations. Foliations generally dip  $\sim 20^\circ$  to the west, and flatten to a more south dipping orientation near Epidote Crag. In some locations, multiple sub parallel stretching and mineral lineations were documented on the same foliation parallel surface.



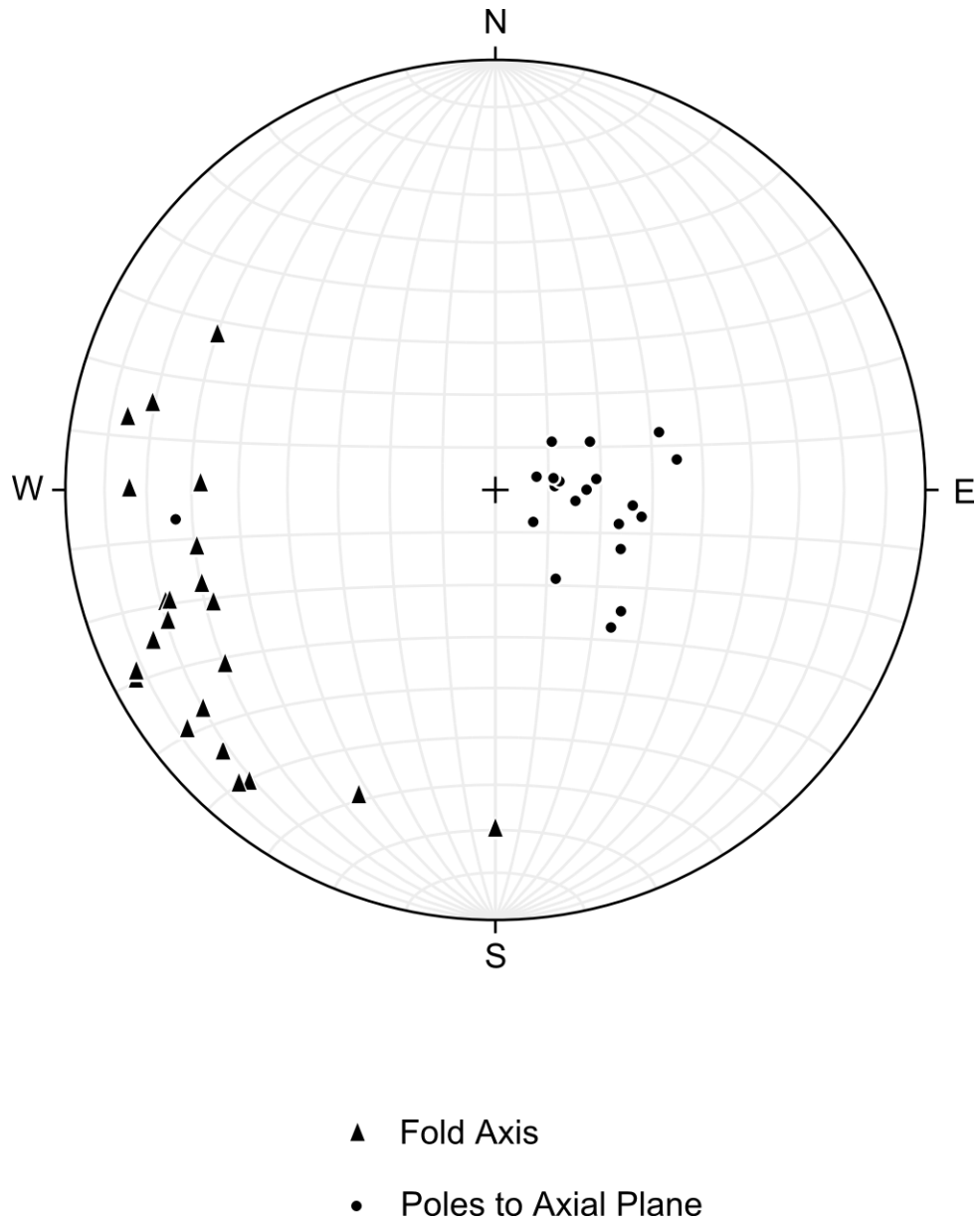


Figure 10: Stereonet of fold axes and axial planes. The axial planes of the measured folds are parallel to the foliation, with the only exception being some of the small parasitic folds documented in the hinge of the larger structures. The fold axes plunge to the south and west. The smaller wavelength folds with transposed limbs tend to dip more towards the west.

Sample#	Qtz	Ksp	Pl	Bt	Cl	Gt	Hbl	En	Di	Sil	Other
14DM03	x	/	x	x	/						apatite
14DM26	x		x	v							apatite, sericite, zircon
14DM32	x	/	x	v			/				
14DM44A	x	/	x	x	/						sericite
14DM44B	x	/	x	x	x						sericite
14DM45	x		x	x			v				apatite, titanite, sericite
14DM47	x	/	x	/	x		x				
14DM48B	x	v	x	x	/						apatite, zircon
14DM50	x	/	x	x		v					
14DM52	x	x	x	x							
14DM53	x		v	x	/	x				x	apatite, rutile
14DM54	x	/	x					x	x		titanite, zircon

Figure 11: Table of mineral phases in thin section. Table of major rock-forming minerals documented in thin section for each sample collected. Minor phases are only listed where they have been identified with confidence. Opaque minerals (not listed) show complex growth and reaction textures in reflected light, however ilmenite, magnetite, and pyrite are common. (Symbols: (x > 10%), (5% < v < 10%), (/ < 5%))



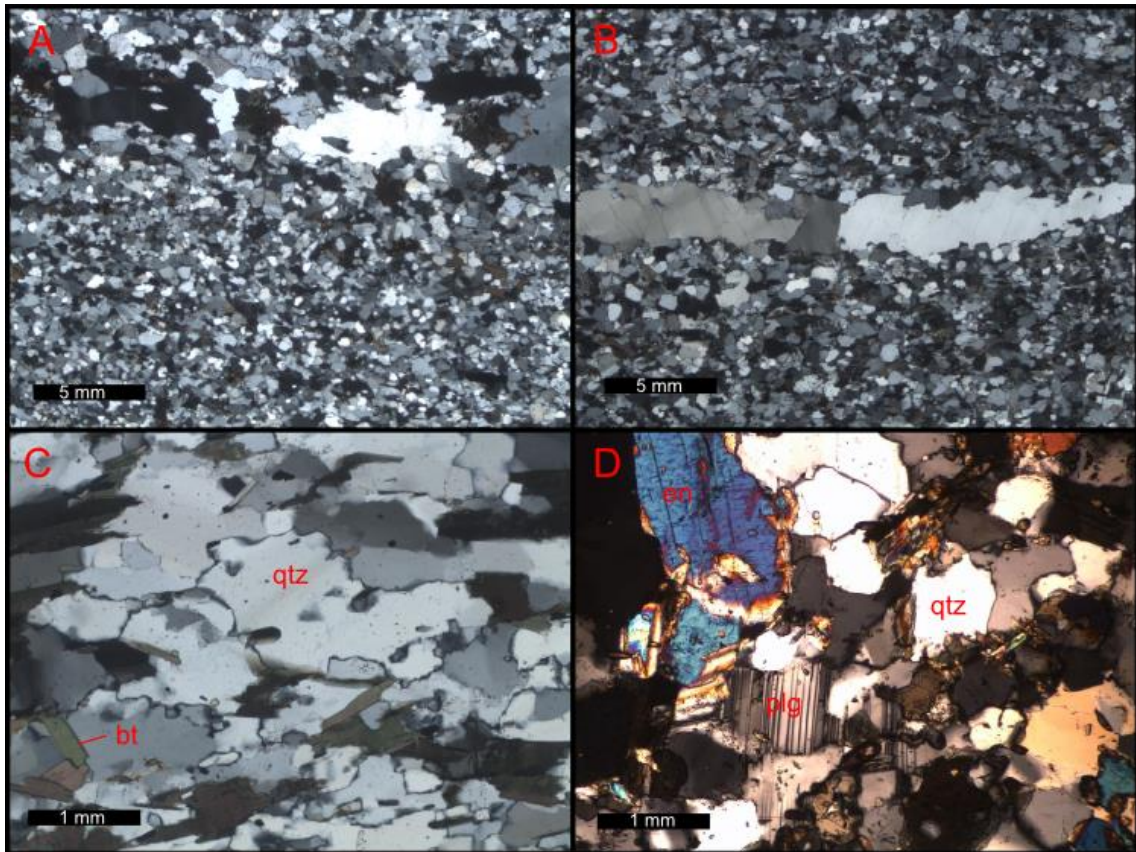


Figure 12: Quartz microstructures. A-B) Photomicrographs of the ultramylonite from exposures east and west of Lluvia Peak. Quartz shows significant grain recovery post deformation. C) Undulose extinction and bulging recrystallization overprints relict grain boundary migration fabric. D) Quartz, plagioclase, and enstatite textures from sample 54, a calc-silicate layer in the rusty gneiss.

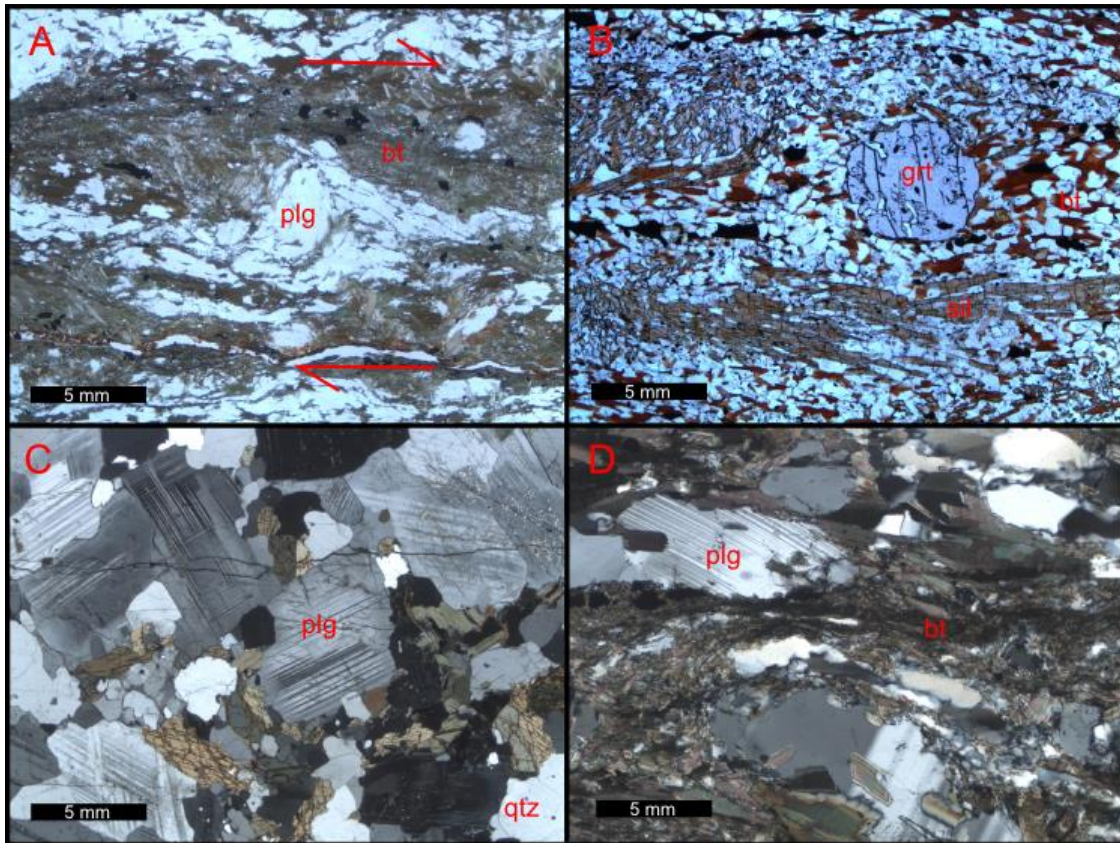


Figure 13: Thin section textures. A) Plagioclase with asymmetric pressure shadows. B) Biotite, garnet, sillimanite, quartz textures from a metapelite unit in the rusty gneiss. No potassium feldspar or muscovite is present. C) Underformed Lluvia Peak pluton with minor sericitic alteration of plagioclase. D) A plane of ultra-fine biotite from within the zone of cataclasite.

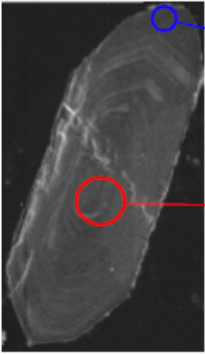
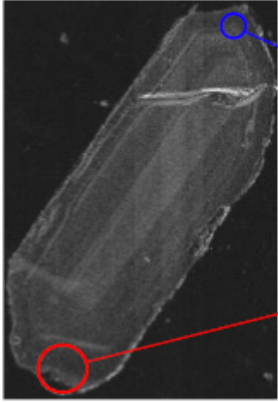
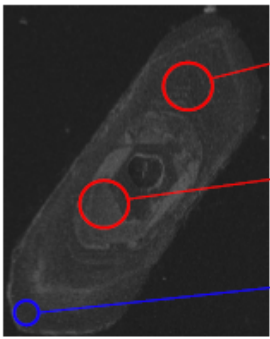
 <p>79 +/- 1.6</p> <p>78 +/- 4.0</p>	<p>Zoned igneous zircon from sample 45. Concentric layers form an elongate shape. No relict core is present in this sample. The blue and red circles represent a 12 and 25 nm laser ablation spot size and location.</p>
 <p>81.3 +/- 2.6</p> <p>90.0 +/- 5.8</p>	<p>Zoned igneous zircon from sample 26. A dissolution texture is present between the inner and outermost layers.</p>
 <p>80.9 +/- 1.6</p> <p>187.4 +/- 3.8</p> <p>82.7 +/- 1.1</p>	<p>Zoned igneous zircon from sample 45. 80-82 ma zoned rims have grown around a relict core with an age of 187.4 ma. A clear dissolution texture is visible.</p>

Figure 14: Igneous cathodoluminescence images.



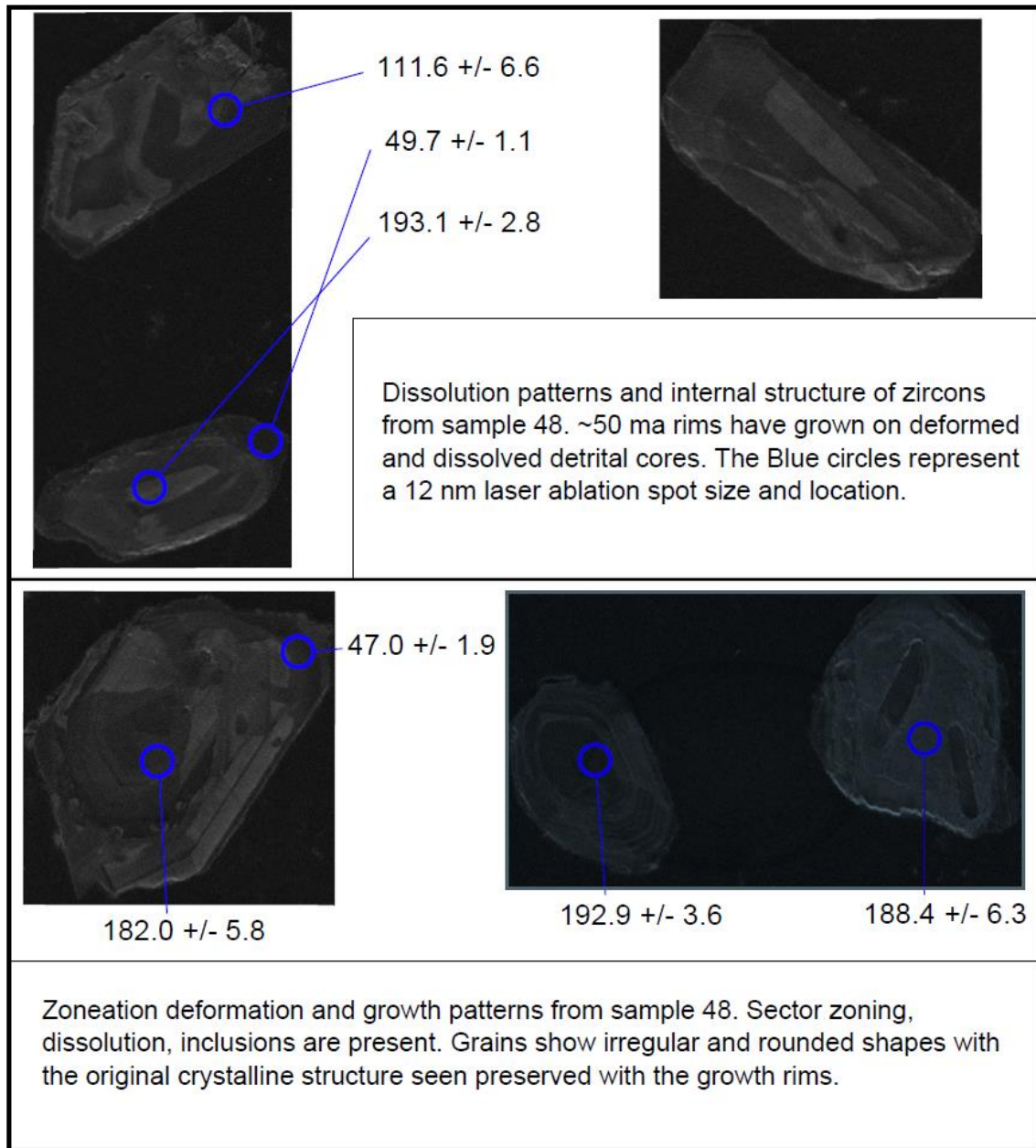


Figure 15: Sample 48 cathodoluminescence images and interpretations.

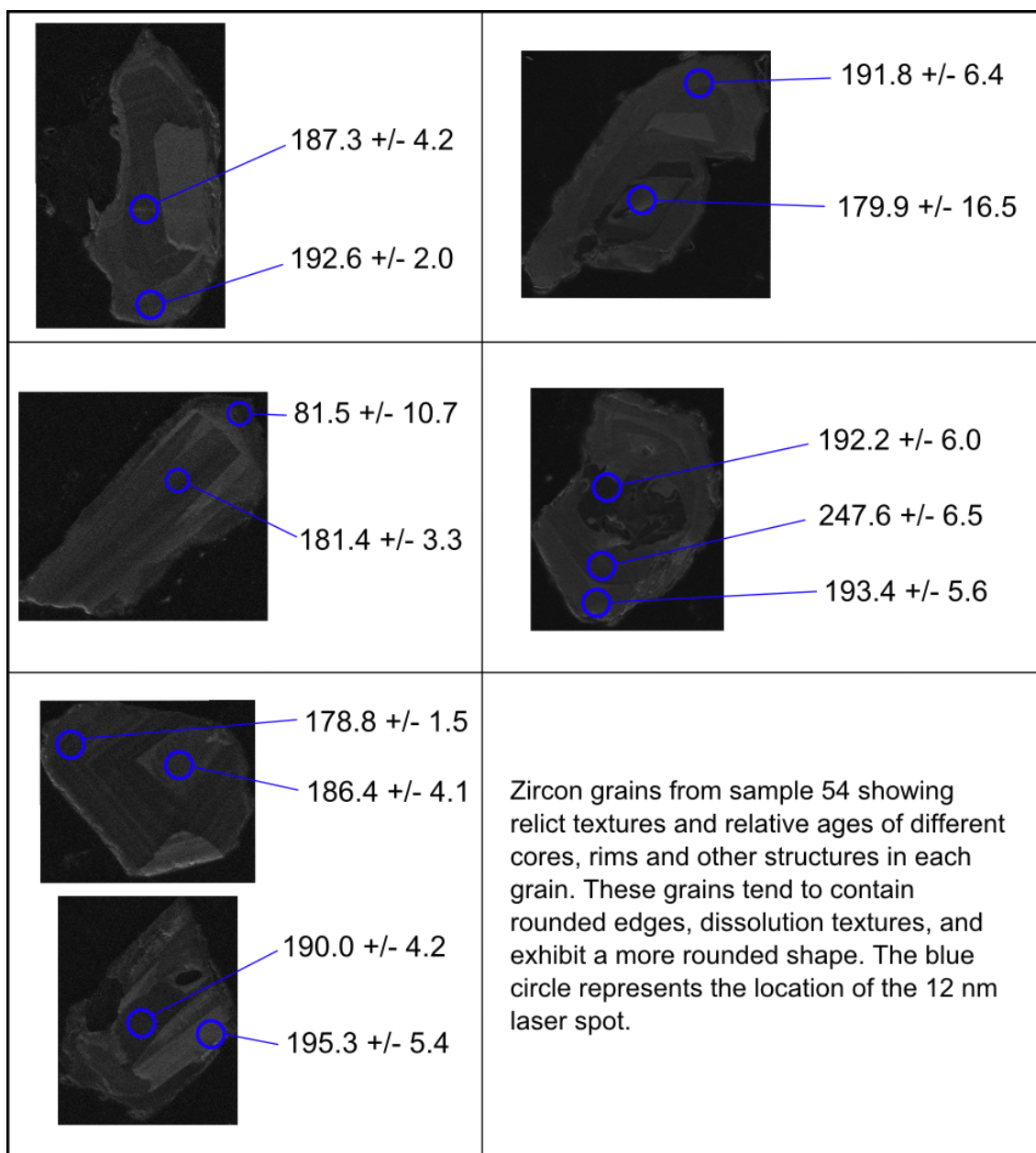


Figure 16: Sample 54 cathodoluminescence images and interpretations.

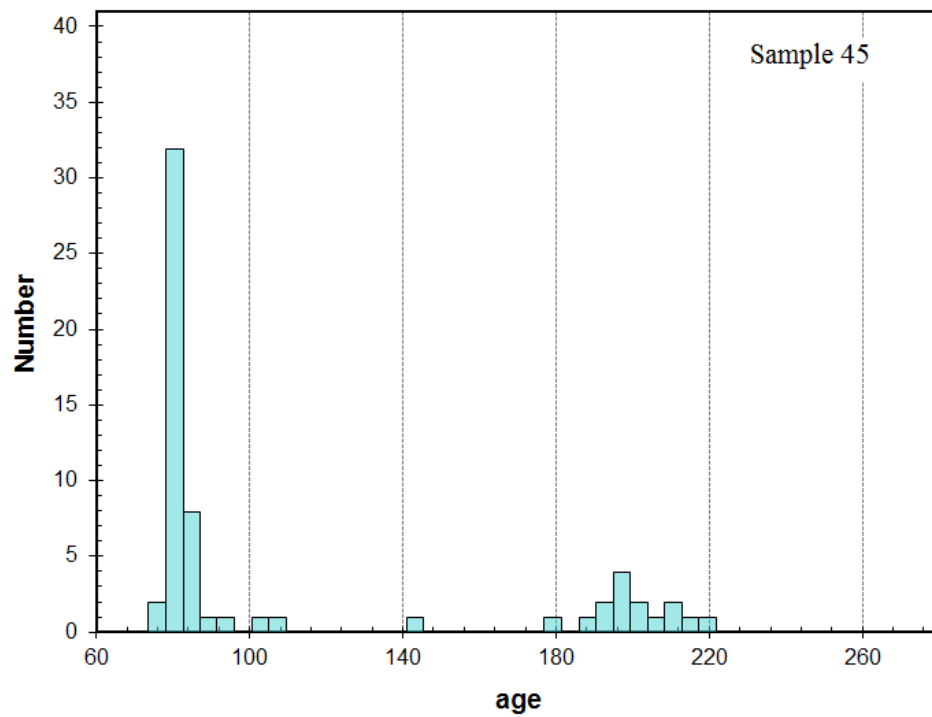
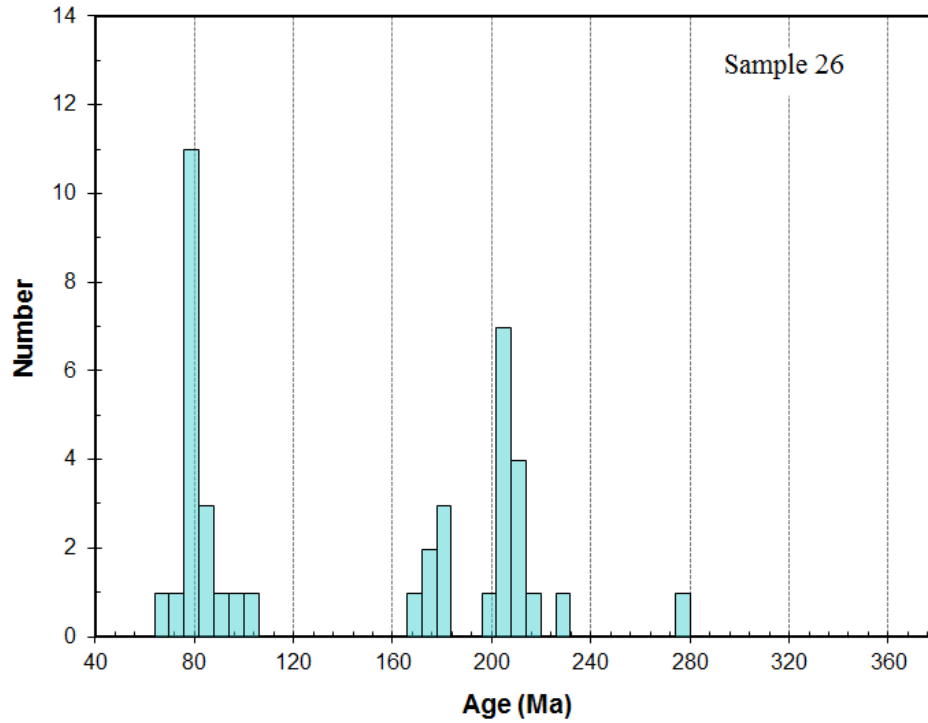


Figure 17: Distribution of igneous zircon analysis. Sample 26 from the crosscutting dike and sample 45 from the Lluvia Peak pluton show distributions around 80 Ma that represents the age of magma cooling as well as an older population of relict cores.

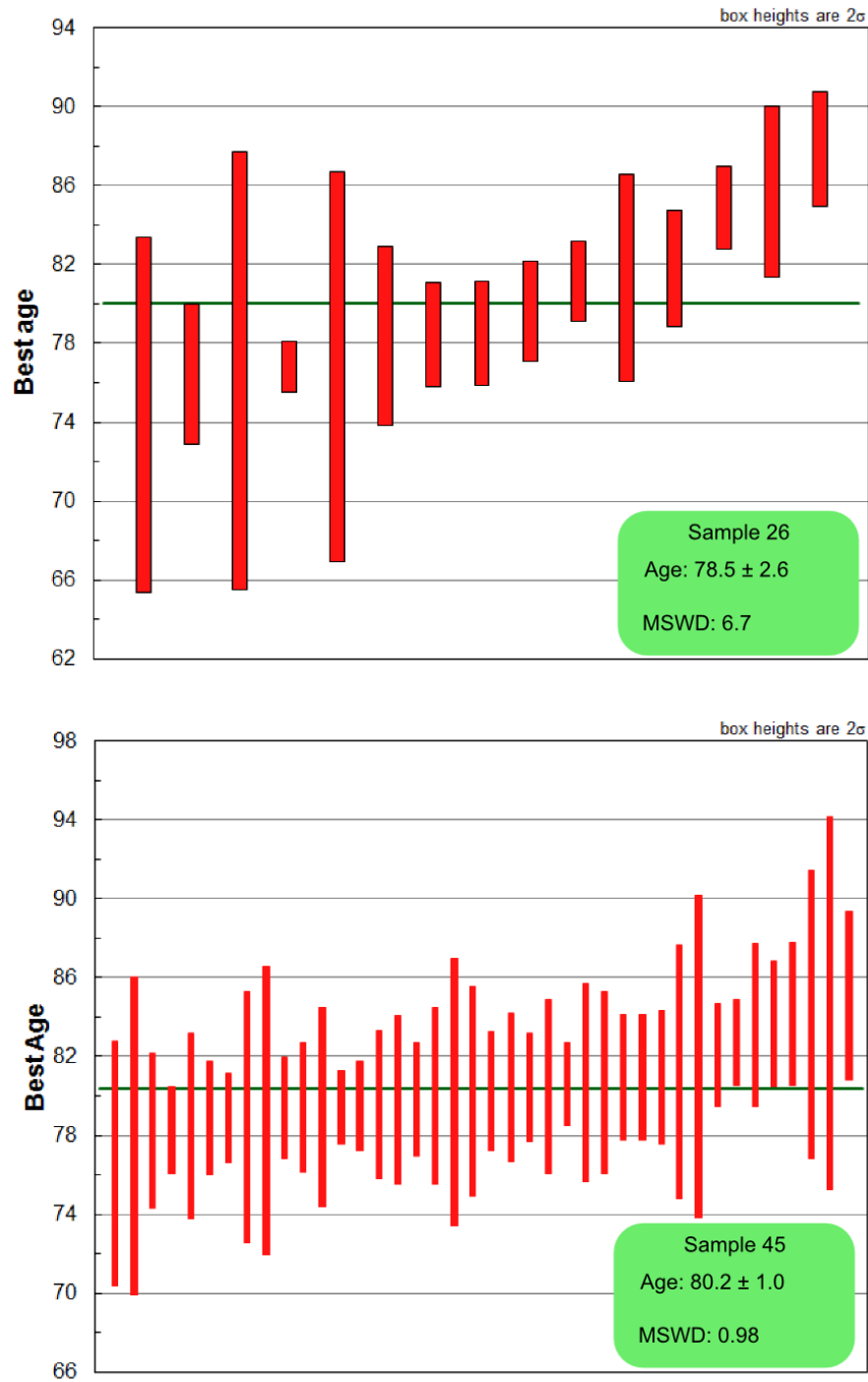


Figure 18: These plots show each age measurement from the zircon rims and their respective errors. The green line is the best calculated age for the sample. Sample 26 has a high MSWD, suggesting underestimated errors, or a small contribution from other domains in a few of the measurements.

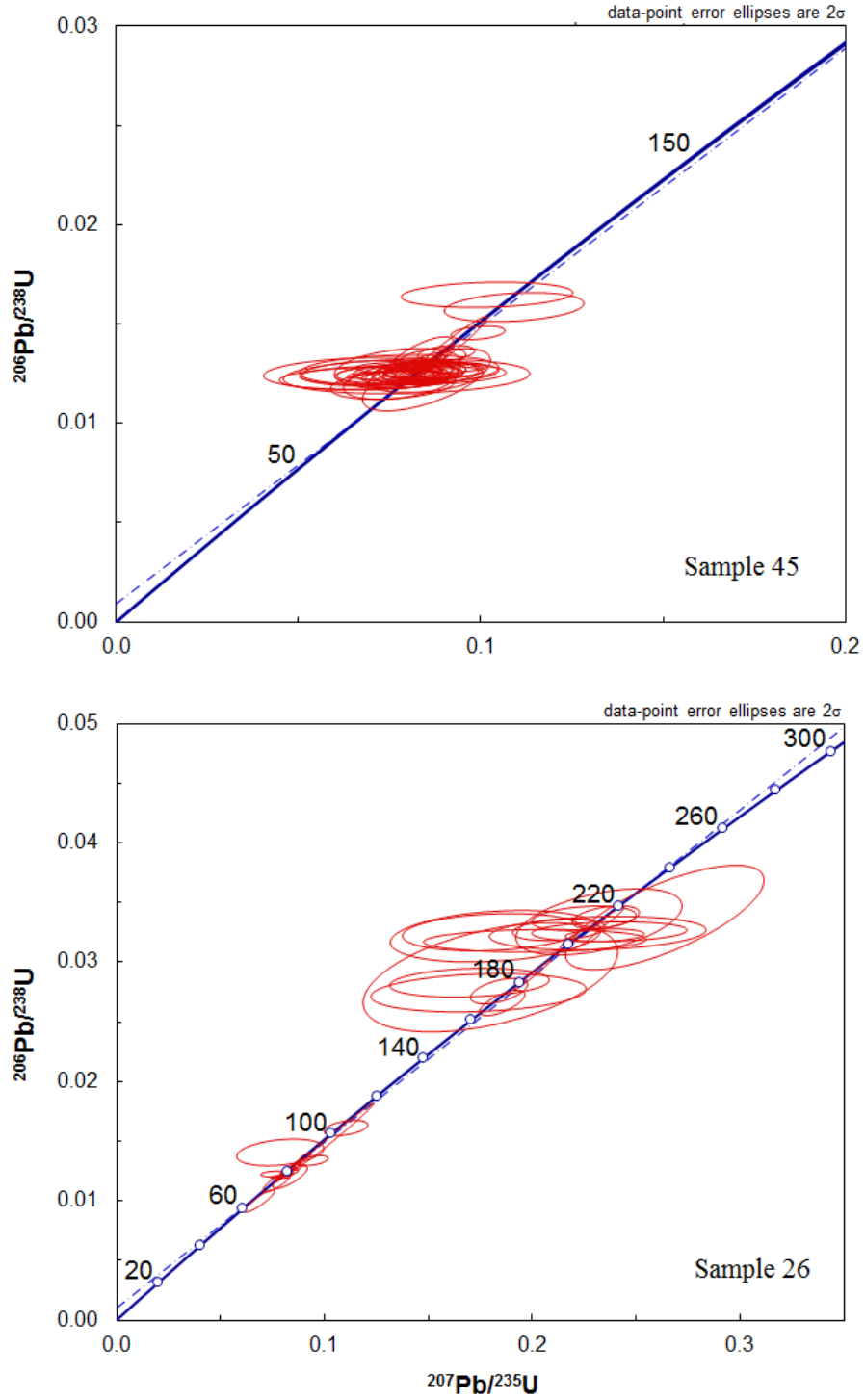


Figure 19: Igneous Concordia plots. Sample 45 (top) and Sample 26 (Bottom) are concordant around 80 Ma. The inherited cores appear concordant, but have larger associated error.



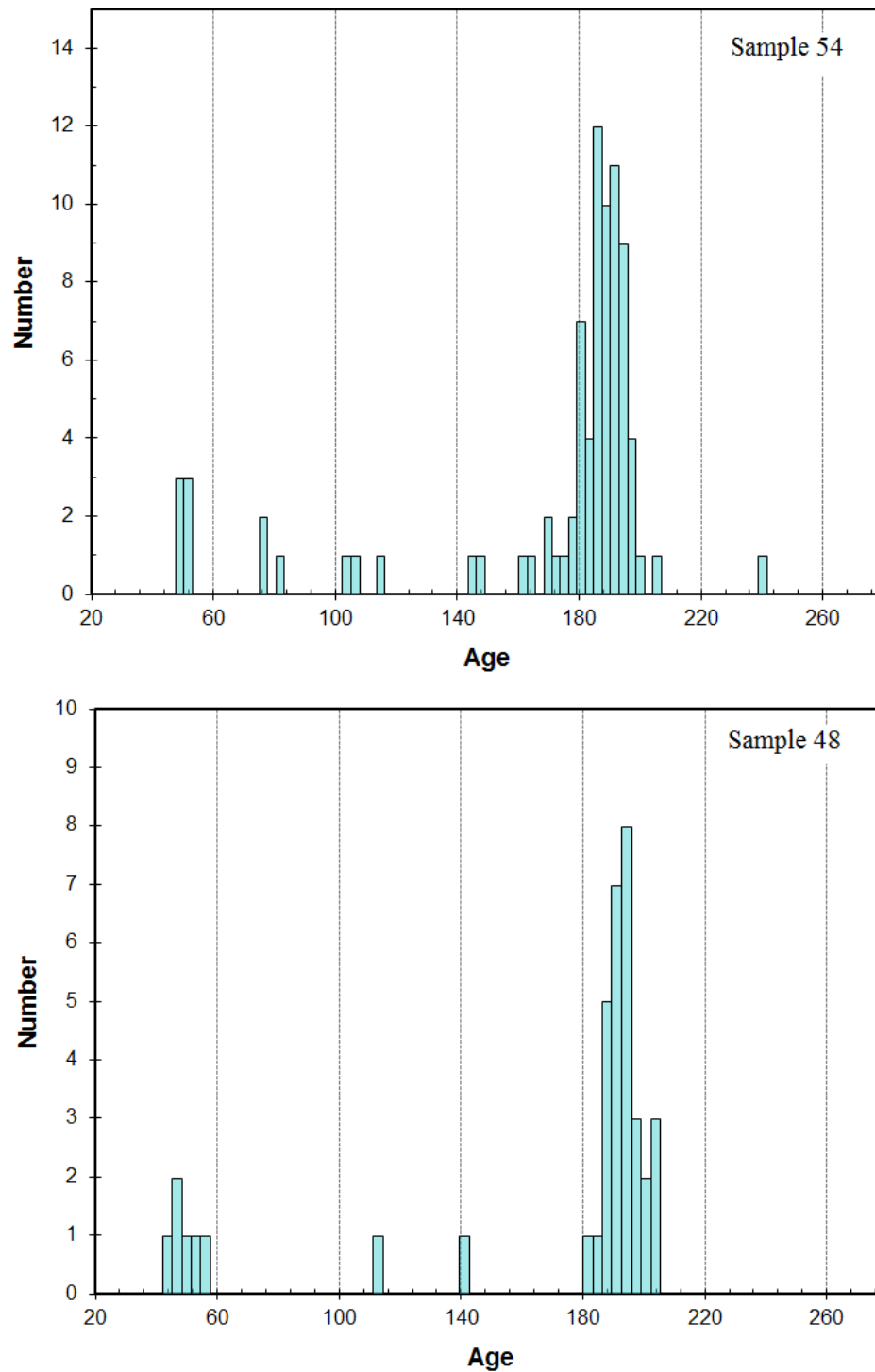


Figure 20: Sedimentary age histogram. The histograms above contain all of the different analysis obtained for samples 48 from the conglomerate, and sample 54 from the rusty gneiss. These graphs contain multiple ages from some grains and do not represent a probability distribution.

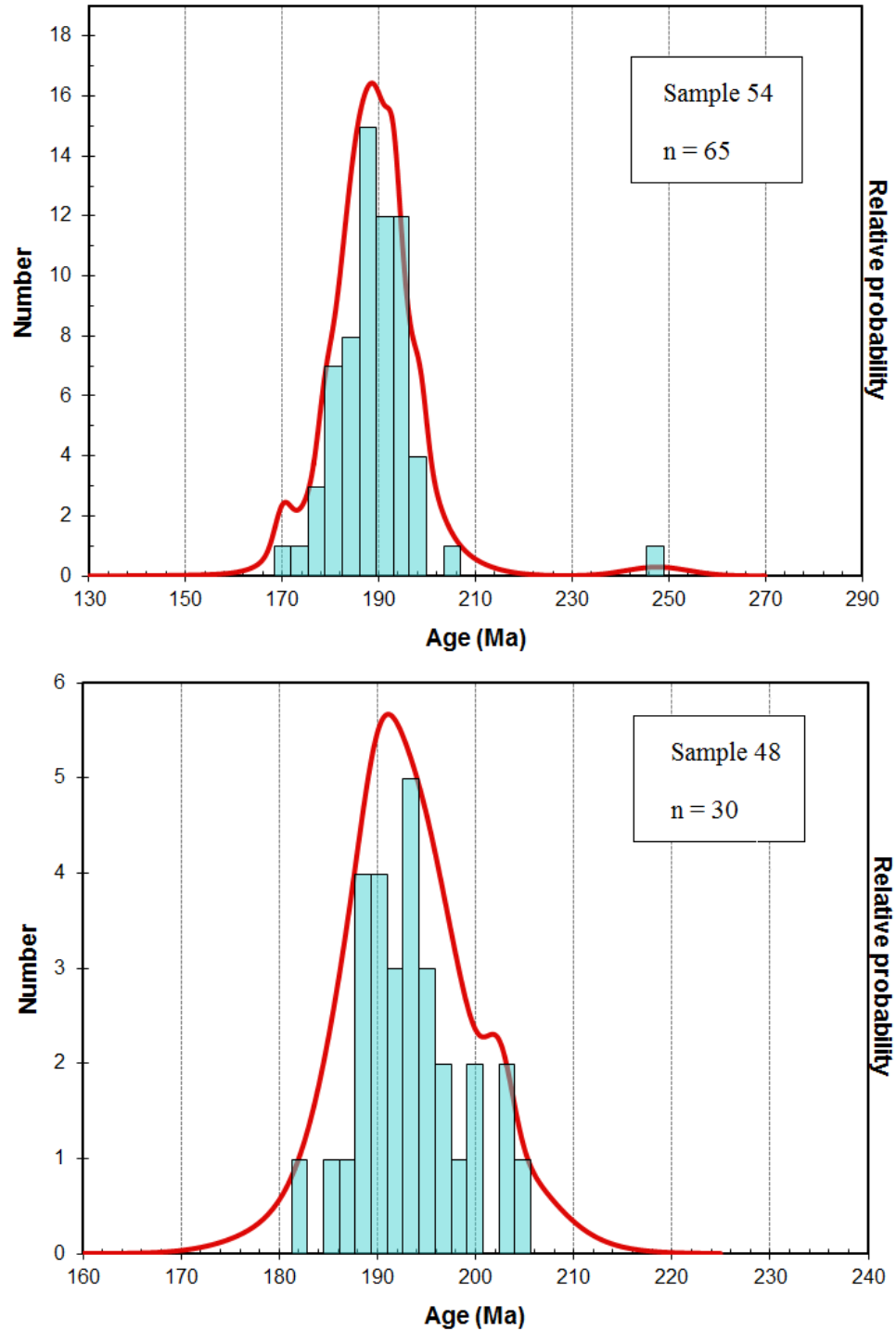


Figure 21: Probability distribution of sedimentary ages. Similar age distributions can be seen between the two samples. Sample 54, from the rusty gneiss, contains several grains between the ages of 170 and 180 Ma that are absent from sample 48 from the conglomerate unit. The peak of 54 is skewed more towards the younger ages.

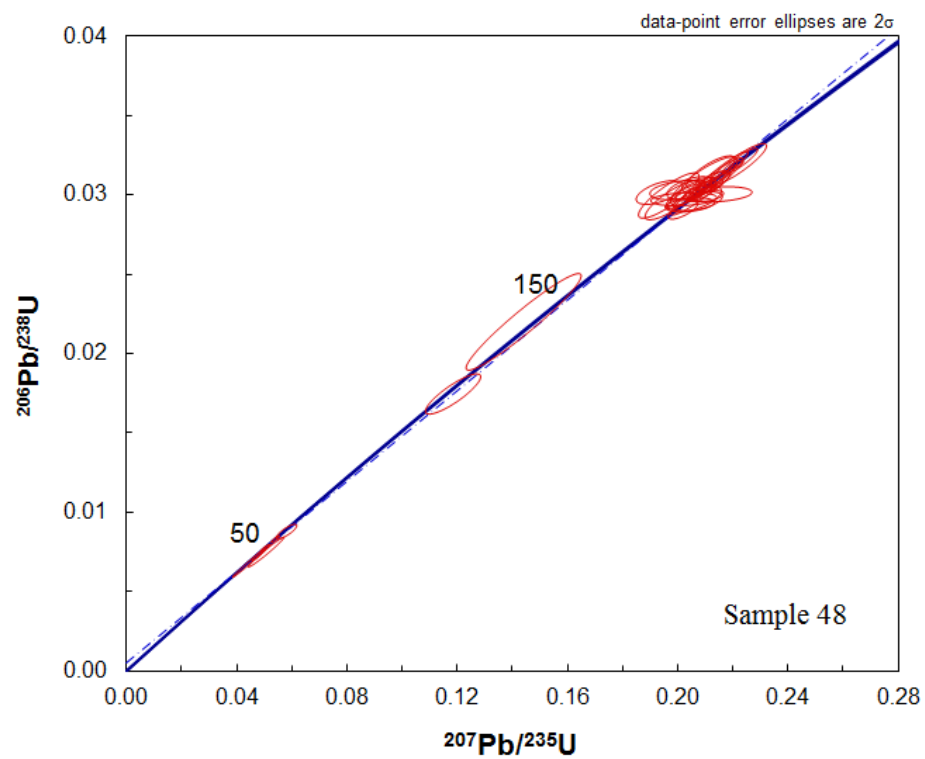
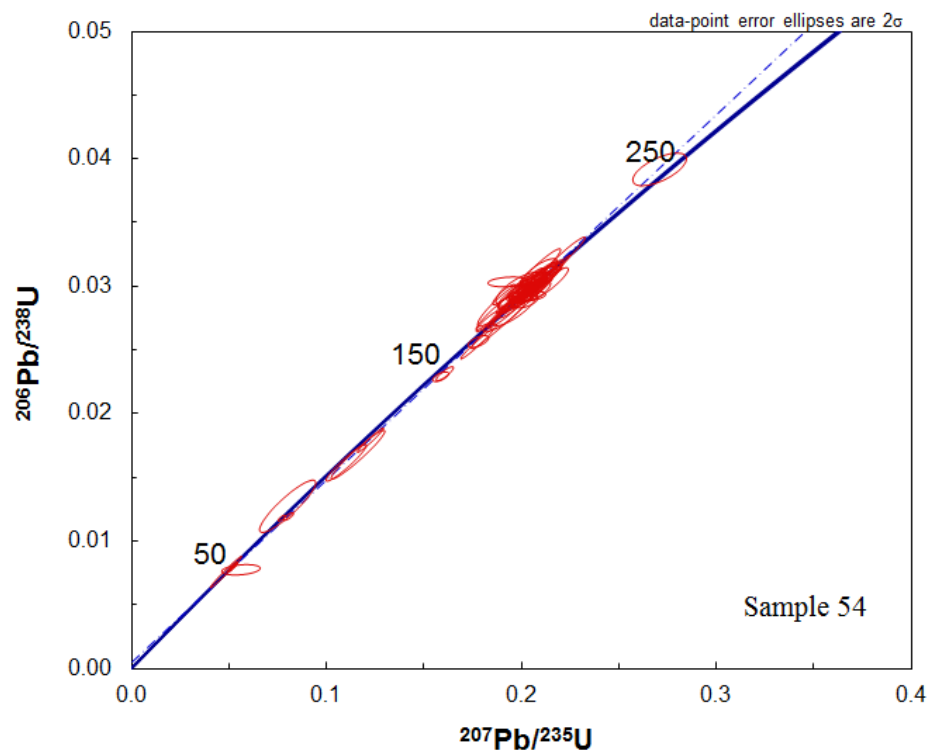


Figure 22: Concordia diagram for metasedimentary sample zircons.

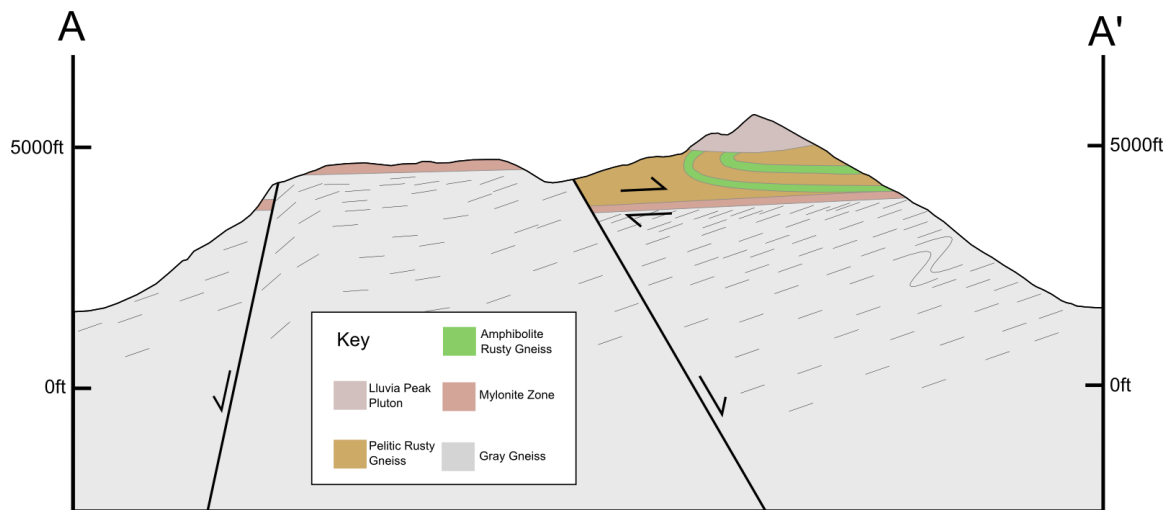


Figure 23: Schematic cross section of Lluvia Peak area showing the different units and apparent foliation dip between points A and A' labeled on the map (Figure 5:), and with no vertical exaggeration. The Lluvia Peak pluton is located above the shear zone at this location, but slopes down to intersect it to the northwest.

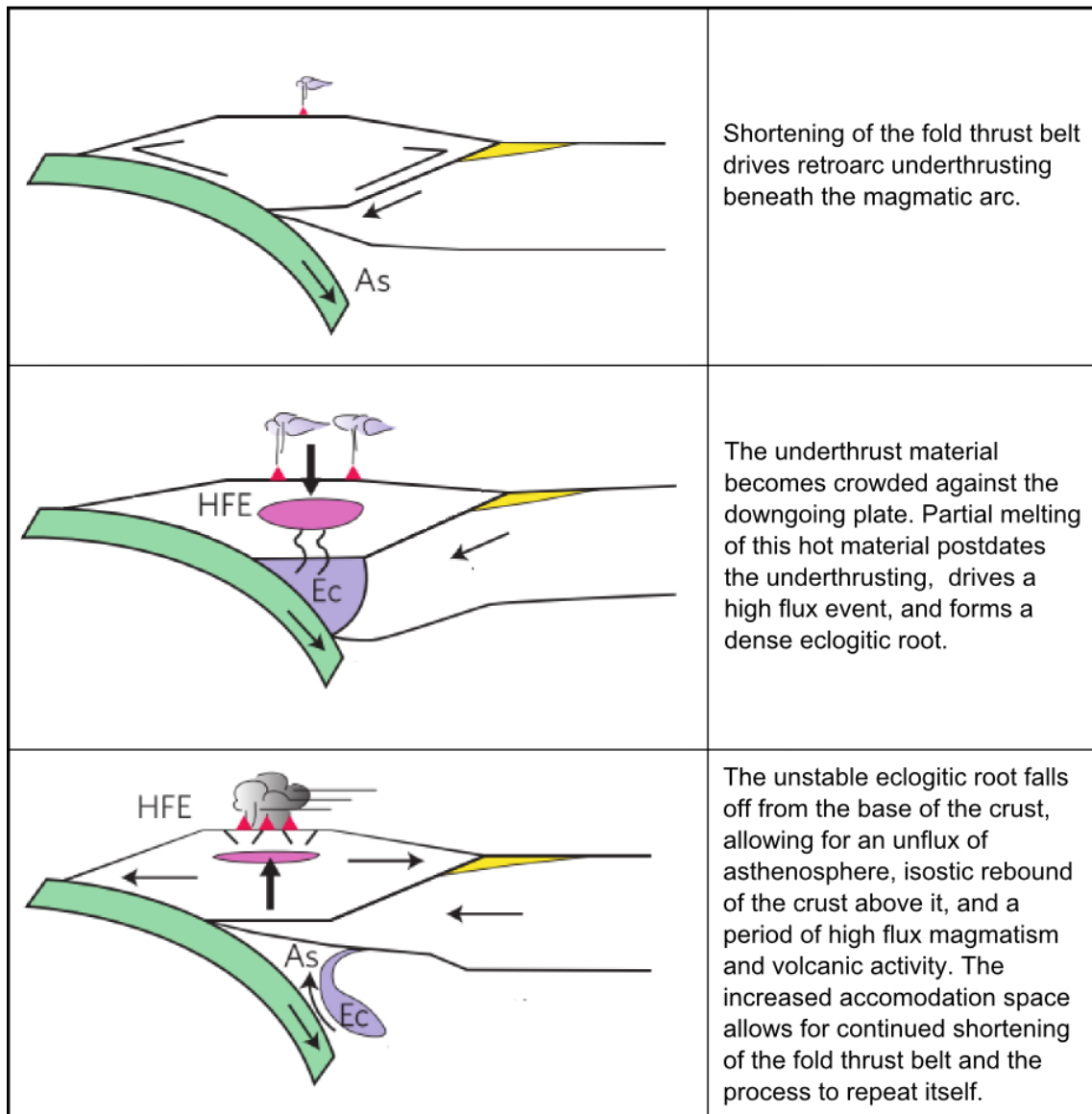


Figure 24: DeCelles orogenic cyclicity model. [Modified from DeCelles et al., 2009]

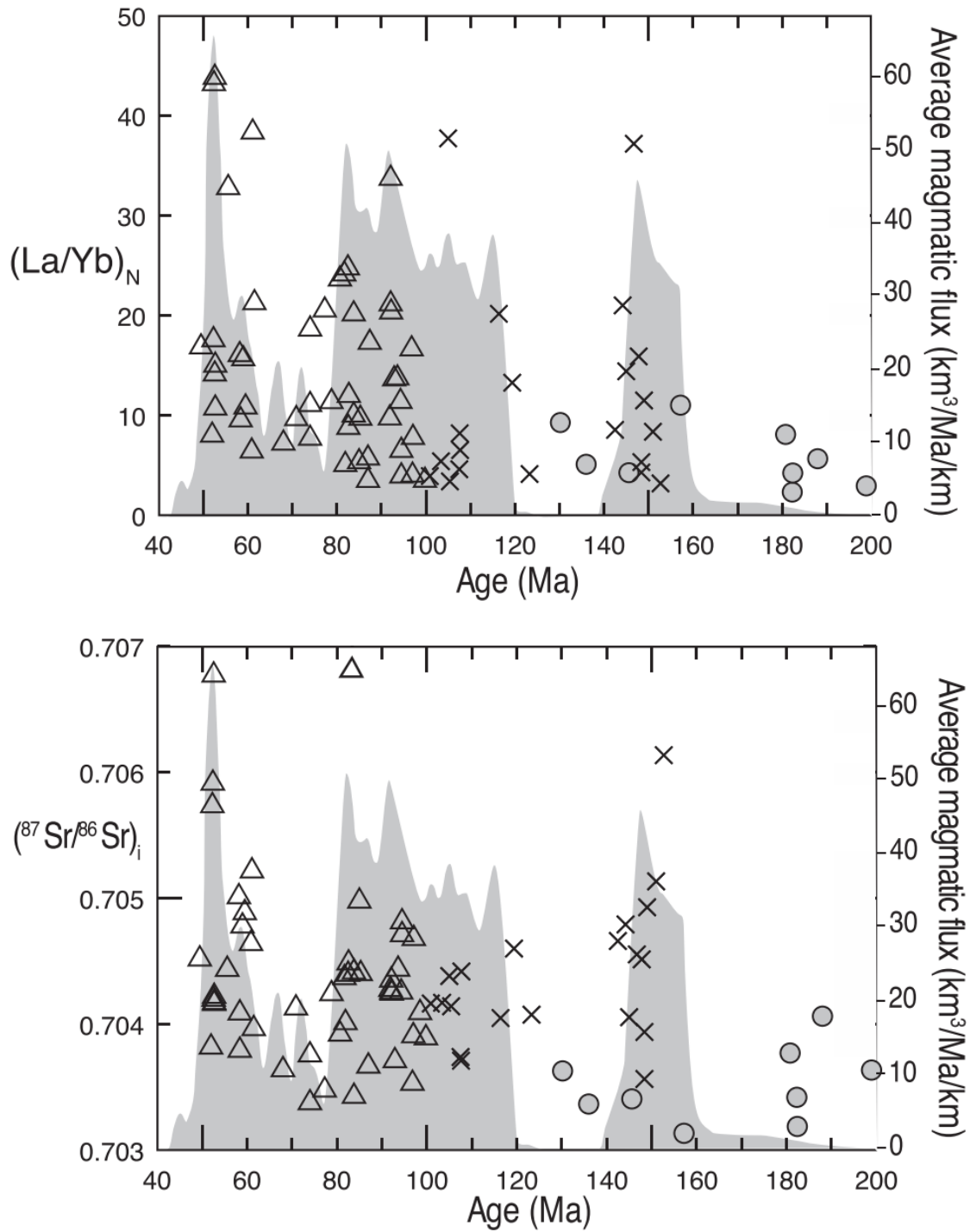


Figure 25: Sr, La/Yb, and magmatic flux (gray shading) [Girardi et al., 2012]. The upper plot of La/Yb, magmatic flux, and age shows a correlation between high rates of magmatic addition and crustal thickness. The lower plot of Sr and magmatic flux suggests an increased crustal contribution to magmas during the high flux events.

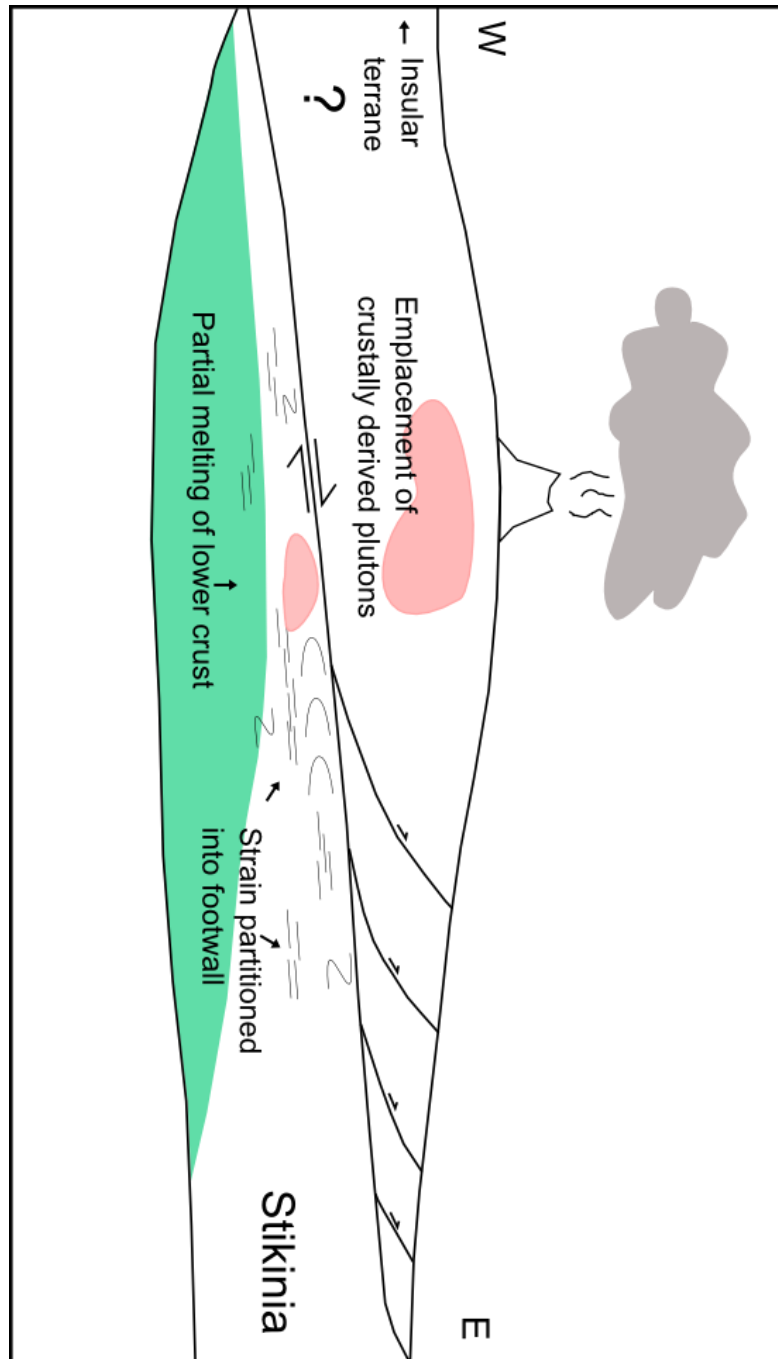


Figure 26: Underthrusting of retroarc material beneath the magmatic arc leads to deformation and partial melting of the underthrust plate. Strain is partitioned into the weak lower crust beneath the main detachment in the form of ductile shear and kilometer scale recumbent folding. The formation of migmatites related to crustal thickening and the emplacement of melt-related plutons occurred contemporaneously with underthrusting.

## 8.6. Zircon data

### 8.6.1. Sample 54

Analysis	U		206Pb		U/Th		206Pb*		±		207Pb*		±		206Pb*		±		error		206Pb*		±		207Pb*		±		206Pb*		±	
	(ppm)	204Pb					207Pb*	(%)	235U*	(%)	238U	(%)	±	corr.	238U*	(Ma)	±	235U	(Ma)	±	207Pb*	(Ma)	±	206Pb*	(Ma)	±	207Pb*	(Ma)	±	206Pb*	(Ma)	±
14DM54+12um-4C	305	3205	8.9	21.5007	2.1	0.0485	13.5	0.0076	13.3	0.99	48.6	6.5	48.1	6.3	24.1	50.1																
14DM54+12um-9R <>	459	3884	5.2	21.1158	1.6	0.0502	2.2	0.0077	1.4	0.65	49.4	0.7	49.7	1.1	67.3	39.2																
14DM54+12um-11R <>	408	3054	5.5	18.9870	13.8	0.0562	14.4	0.0077	4.3	0.30	49.7	2.1	55.5	7.8	314.5	314.8																
14DM54+12um-13R <>	334	3019	12.6	21.0004	1.4	0.0519	2.5	0.0079	2.2	0.85	50.7	1.1	51.3	1.3	80.3	32.3																
14DM54+12um-6R <>	464	5722	32.7	21.1156	1.3	0.0524	3.0	0.0080	2.7	0.89	51.5	1.4	51.8	1.5	67.3	31.9																
14DM54+12um-29C <>	608	6313	61.7	21.1749	1.7	0.0529	2.9	0.0081	2.3	0.80	52.1	1.2	52.3	1.5	60.7	40.9																
14DM54+12um-32C <>	879	13229	5.2	21.0849	1.2	0.0771	2.0	0.0118	1.6	0.79	75.6	1.2	75.4	1.5	70.8	29.1																
14DM54+12um-42C <>	163	7102	22.1	20.3787	1.6	0.0807	2.6	0.0119	2.0	0.79	76.4	1.5	78.8	2.0	151.2	37.5																
14DM54+12um-3C <>	79	962	12.6	21.8841	6.5	0.0802	14.7	0.0127	13.2	0.90	81.5	10.7	78.3	11.1	-18.4	157.6																
14DM54+12um-61C <>	150	4115	3.5	20.1865	2.4	0.1102	7.7	0.0161	7.3	0.95	103.2	7.5	106.1	7.8	173.4	56.9																
14DM54+12um-50C <>	37	1274	6.2	19.8942	2.7	0.1162	9.7	0.0168	9.3	0.96	107.2	9.9	111.7	10.3	207.3	62.9																
14DM54+12um-34C <>	434	9742	2.8	20.1401	1.0	0.1226	4.5	0.0179	4.4	0.98	114.5	5.0	117.5	5.0	178.7	22.6																
14DM54+12um-60C <>	590	10732	4.5	19.8948	1.6	0.1586	2.1	0.0229	1.3	0.63	145.9	1.9	149.5	3.0	207.2	38.3																
14DM54+12um-4R <>	149	4784	1.9	19.8298	1.1	0.1608	2.3	0.0231	2.0	0.87	147.4	2.9	151.4	3.2	214.8	25.8																
14DM54+12um-72C <>	2038	31468	8.9	19.7969	0.8	0.1772	3.8	0.0254	3.7	0.98	162.0	6.0	165.7	5.8	218.7	18.1																
14DM54+12um-11C <>	141	6755	2.4	19.8741	1.9	0.1780	2.5	0.0257	1.5	0.61	163.3	2.4	166.3	3.8	209.6	44.9																
14DM54+12um-49C <>	116	5340	2.4	18.0172	33.1	0.2035	35.9	0.0266	13.8	0.38	169.2	23.0	188.1	61.7	432.5	757.3																
14DM54+12um-53C <>	263	13360	2.8	20.0483	1.2	0.1839	1.6	0.0267	1.0	0.63	170.1	1.7	171.4	2.5	189.4	28.6																
14DM54+12um-63C <>	69	2416	2.2	20.5424	1.1	0.1828	2.6	0.0272	2.4	0.92	173.2	4.1	170.4	4.1	132.5	24.8																
14DM54+12um-36C <>	79	3657	2.3	19.8100	1.6	0.1931	3.8	0.0277	3.5	0.91	176.4	6.1	179.3	6.3	217.1	37.6																
14DM54+12um-39C <>	121	3208	2.0	20.6593	1.2	0.1863	4.2	0.0279	4.0	0.95	177.5	7.0	173.4	6.6	119.1	29.3																
14DM54+12um-2R <>	169	4568	1.6	20.3580	1.2	0.1904	1.4	0.0281	0.8	0.58	178.8	1.5	177.0	2.3	153.6	27.6																
14DM54+12um-48C <>	100	6494	2.9	19.7653	2.6	0.1970	4.7	0.0282	3.9	0.83	179.5	6.9	182.6	7.8	222.4	60.7																
14DM54+12um-31C <>	127	4789	2.2	20.1095	1.5	0.1938	4.7	0.0283	4.4	0.94	179.7	7.9	179.9	7.7	182.3	35.9																
14DM54+12um-8C <>	285	9125	4.2	19.7974	1.5	0.1971	9.4	0.0283	9.3	0.99	179.9	16.5	182.6	15.7	218.6	34.2																



Analysis	U (ppm)	<sup>206</sup> Pb <sup>204</sup> Pb	U/Th	<sup>206</sup> Pb* <sup>207</sup> Pb*	± (%)	<sup>207</sup> Pb* <sup>235</sup> U*	± (%)	<sup>206</sup> Pb* <sup>238</sup> U	± (%)	error corr.	<sup>206</sup> Pb* <sup>238</sup> U*	± (Ma)	<sup>207</sup> Pb* <sup>235</sup> U	± (Ma)	<sup>206</sup> Pb* <sup>207</sup> Pb*	± (Ma)
<sup>14</sup> DM54+12um-69C <>	408	12088	0.8	20.0675	1.4	0.1953	3.0	0.0284	2.7	0.88	180.7	4.8	181.2	5.0	187.1	33.3
<sup>14</sup> DM54+12um-3C <>	121	4149	1.3	20.3317	0.9	0.1935	2.0	0.0285	1.8	0.90	181.4	3.3	179.6	3.4	156.6	20.9
<sup>14</sup> DM54+12um-67C <>	315	10862	0.8	20.1114	0.9	0.1956	2.2	0.0285	2.0	0.92	181.4	3.7	181.4	3.7	182.0	20.5
<sup>14</sup> DM54+12um-7C <>	67	2557	1.3	20.7216	2.3	0.1907	5.6	0.0287	5.1	0.92	182.1	9.2	177.2	9.1	112.0	53.3
<sup>14</sup> DM54+12um-35C <>	140	5663	1.5	20.4005	2.2	0.1941	2.6	0.0287	1.4	0.53	182.5	2.5	180.1	4.3	148.7	52.2
<sup>14</sup> DM54+12um-46C <>	2007	31845	9.7	19.6102	2.1	0.2024	2.5	0.0288	1.4	0.56	182.9	2.5	187.1	4.3	240.6	47.5
<sup>14</sup> DM54+12um-59C <>	344	8519	1.2	20.2789	0.8	0.1960	2.5	0.0288	2.4	0.95	183.2	4.3	181.7	4.1	162.7	18.0
<sup>14</sup> DM54+12um-44C <>	113	3608	1.3	20.2342	2.7	0.1974	3.7	0.0290	2.6	0.70	184.1	4.8	183.0	6.3	167.8	62.0
<sup>14</sup> DM54+12um-38C <>	65	2145	2.6	20.6140	1.7	0.1952	3.1	0.0292	2.6	0.84	185.4	4.8	181.0	5.2	124.2	40.7
<sup>14</sup> DM54+12um-58C <>	251	10308	1.2	19.9353	1.4	0.2020	2.6	0.0292	2.2	0.85	185.5	4.1	186.8	4.5	202.5	32.2
<sup>14</sup> DM54+12um-15C <>	218	4855	2.7	19.8333	3.6	0.2032	3.7	0.0292	1.1	0.30	185.7	2.1	187.8	6.4	214.4	82.8
<sup>14</sup> DM54+12um-33C <>	872	27876	1.6	19.9251	0.6	0.2025	2.0	0.0293	1.9	0.95	186.0	3.4	187.3	3.4	203.7	13.6
<sup>14</sup> DM54+12um-2C <>	76	1948	1.7	21.1624	1.1	0.1912	2.5	0.0293	2.2	0.89	186.4	4.1	177.6	4.1	62.1	27.3
<sup>14</sup> DM54+12um-51C <>	106	4600	1.4	20.3603	1.8	0.1987	2.2	0.0293	1.3	0.60	186.5	2.4	184.1	3.7	153.3	41.3
<sup>14</sup> DM54+12um-21C <>	214	7300	2.8	20.1245	1.1	0.2012	2.3	0.0294	2.1	0.89	186.5	3.8	186.1	4.0	180.5	25.4
<sup>14</sup> DM54+12um-10C <>	219	10213	0.9	19.7721	0.8	0.2050	2.3	0.0294	2.2	0.94	186.8	4.0	189.4	4.0	221.5	17.9
<sup>14</sup> DM54+12um-26C <>	124	5432	1.5	20.1804	1.7	0.2014	2.9	0.0295	2.3	0.80	187.3	4.2	186.3	4.9	174.1	39.6
<sup>14</sup> DM54+12um-70C <>	176	5382	1.3	19.9177	1.5	0.2041	3.6	0.0295	3.3	0.90	187.3	6.0	188.6	6.2	204.6	35.7
<sup>14</sup> DM54+12um-64C <>	60	2532	2.4	20.1612	1.9	0.2017	3.1	0.0295	2.4	0.79	187.4	4.5	186.6	5.2	176.3	43.7
<sup>14</sup> DM54+12um-14C <>	77	2595	1.7	19.8815	2.0	0.2048	2.8	0.0295	2.0	0.71	187.6	3.6	189.2	4.8	208.8	45.4
<sup>14</sup> DM54+12um-13C <>	81	3587	1.6	19.6194	1.8	0.2079	2.8	0.0296	2.2	0.77	187.9	4.1	191.7	5.0	239.5	41.8
<sup>14</sup> DM54+12um-28C <>	289	20774	1.8	19.7187	1.3	0.2073	2.7	0.0296	2.4	0.88	188.3	4.4	191.3	4.7	227.8	29.4
<sup>14</sup> DM54+12um-57C <>	395	16258	1.3	20.1179	0.8	0.2035	2.4	0.0297	2.3	0.94	188.6	4.2	188.1	4.1	181.3	18.3
<sup>14</sup> DM54+12um-6C <>	116	4135	1.7	20.2377	1.3	0.2026	1.7	0.0297	1.0	0.60	188.9	1.9	187.3	2.9	167.4	31.4
<sup>14</sup> DM54+12um-55C <>	131	3725	2.9	20.6192	1.4	0.1990	2.7	0.0298	2.4	0.86	189.0	4.4	184.2	4.6	123.6	32.4
<sup>14</sup> DM54+12um-19C <>	57	1682	1.7	20.6206	3.5	0.1991	5.0	0.0298	3.6	0.72	189.2	6.8	184.4	8.5	123.5	81.7
<sup>14</sup> DM54+12um-56C <>	180	6974	2.4	20.4006	1.9	0.2015	3.2	0.0298	2.5	0.80	189.4	4.7	186.4	5.4	148.7	45.1
<sup>14</sup> DM54+12um-66C <>	194	5830	1.2	20.0265	1.3	0.2055	2.4	0.0299	2.1	0.85	189.6	3.8	189.8	4.2	191.9	29.3
<sup>14</sup> DM54+12um-5C <>	399	17809	1.2	19.9196	1.1	0.2071	2.5	0.0299	2.2	0.90	190.0	4.2	191.1	4.3	204.3	25.0

Analysis	U (ppm)	<sup>206</sup> Pb 204Pb	U/Th	<sup>206</sup> Pb* 207Pb*	± (%)	<sup>207</sup> Pb* 235U*	± (%)	<sup>206</sup> Pb* 238U	± (%)	error corr.	<sup>206</sup> Pb* 238U*	± (Ma)	<sup>207</sup> Pb* 235U	± (Ma)	<sup>206</sup> Pb* 207Pb*	± (Ma)
14DM54+12um-62C <>	99	2612	1.7	20.2486	1.7	0.2039	2.0	0.0299	1.0	0.52	190.2	1.9	188.4	3.4	166.2	39.0
14DM54+12um-71C <>	192	6196	1.0	20.1553	1.8	0.2054	3.1	0.0300	2.6	0.83	190.7	4.8	189.6	5.4	177.0	40.9
14DM54+12um-52C <>	92	4136	3.0	20.3505	1.3	0.2034	3.9	0.0300	3.6	0.94	190.7	6.8	188.0	6.6	154.4	29.8
14DM54+12um-23C <>	111	5273	1.3	19.9529	1.2	0.2076	2.3	0.0300	2.0	0.87	190.8	3.8	191.5	4.1	200.5	26.9
14DM54+12um-27C <>	128	3386	1.6	20.3806	1.5	0.2033	3.3	0.0300	3.0	0.90	190.8	5.6	187.9	5.7	151.0	34.3
14DM54+12um-37C <>	392	14032	3.2	20.0794	1.0	0.2063	2.5	0.0301	2.2	0.91	190.9	4.2	190.5	4.3	185.8	23.3
14DM54+12um-12C <>	226	11176	2.1	19.7791	1.4	0.2096	2.7	0.0301	2.2	0.84	190.9	4.2	193.2	4.7	220.7	33.2
14DM54+12um-8R <>	55	4070	2.2	19.4308	1.6	0.2143	3.8	0.0302	3.4	0.90	191.8	6.4	197.1	6.7	261.7	37.5
14DM54+12um-1C <>	335	12609	1.7	19.9205	0.9	0.2093	3.3	0.0302	3.2	0.96	192.0	6.0	193.0	5.8	204.2	21.0
14DM54+12um-26R <>	55	1746	2.3	21.6647	4.2	0.1931	4.3	0.0303	1.0	0.24	192.6	2.0	179.2	7.1	5.9	100.7
14DM54+12um-43C <>	95	5100	2.9	19.8734	1.6	0.2109	1.7	0.0304	0.6	0.36	193.0	1.2	194.3	3.1	209.7	37.8
14DM54+12um-40C <>	80	2865	1.3	15.9819	25.7	0.2623	26.5	0.0304	6.6	0.25	193.0	12.6	236.5	56.0	693.7	556.2
14DM54+12um-20C <>	221	7186	2.2	20.1976	1.0	0.2078	4.0	0.0304	3.8	0.97	193.3	7.3	191.7	6.9	172.1	23.8
14DM54+12um-30C <>	160	4519	2.2	20.5153	1.4	0.2046	3.0	0.0304	2.7	0.89	193.3	5.0	189.0	5.1	135.6	31.9
14DM54+12um-1R <>	54	1949	1.8	20.1526	2.6	0.2084	3.9	0.0305	3.0	0.75	193.4	5.6	192.2	6.9	177.3	60.5
14DM54+12um-16C <>	126	2959	2.2	20.4429	2.3	0.2056	2.5	0.0305	1.0	0.40	193.5	1.9	189.8	4.4	143.8	54.1
14DM54+12um-24C <>	167	4741	1.6	20.1121	2.0	0.2093	2.6	0.0305	1.6	0.63	193.8	3.1	192.9	4.6	182.0	46.9
14DM54+12um-18C <>	97	4081	1.6	20.0290	1.9	0.2105	4.4	0.0306	3.9	0.90	194.2	7.5	194.0	7.7	191.6	43.9
14DM54+12um-54C <>	193	19449	1.5	19.9554	1.5	0.2124	3.3	0.0307	2.9	0.89	195.2	5.6	195.5	5.8	200.2	34.8
14DM54+12um-5M <>	96	4443	2.4	20.0056	1.9	0.2120	3.4	0.0308	2.8	0.83	195.3	5.4	195.2	6.0	194.4	44.0
14DM54+12um-22C <>	420	17855	1.5	19.8700	0.7	0.2134	4.5	0.0308	4.4	0.99	195.3	8.5	196.4	8.0	210.1	15.8
14DM54+12um-47C <>	169	9669	1.6	19.9271	0.7	0.2139	1.5	0.0309	1.4	0.90	196.3	2.6	196.8	2.7	203.5	15.5
14DM54+12um-17C <>	73	2513	2.6	20.4831	2.3	0.2091	3.7	0.0311	2.9	0.79	197.2	5.6	192.8	6.5	139.2	53.5
14DM54+12um-45C <>	437	9423	1.1	20.2199	1.2	0.2127	2.3	0.0312	2.0	0.86	198.0	3.8	195.8	4.1	169.5	27.5
14DM54+12um-9C <>	269	13413	0.9	19.9442	1.6	0.2164	1.7	0.0313	0.7	0.40	198.7	1.3	198.9	3.1	201.5	36.3
14DM54+12um-29R <>	103	2675	2.9	20.6730	1.3	0.2098	4.1	0.0314	3.9	0.94	199.6	7.6	193.3	7.2	117.5	31.6
14DM54+12um-25C <>	128	6174	1.2	20.0878	1.1	0.2219	4.0	0.0323	3.8	0.96	205.1	7.7	203.5	7.4	184.8	25.5
14DM54+12um-1M <>	133	6196	3.7	19.9269	3.2	0.2710	4.2	0.0392	2.7	0.65	247.6	6.5	243.5	9.0	203.5	73.7

## 8.6.2. Sample 48

Analysis	U (ppm)	206Pb 204Pb	U/Th	206Pb* 207Pb*	± (%)	207Pb* 235U*	± (%)	206Pb* 238U	± (%)	error corr.	206Pb* 238U*	± (Ma)	207Pb* 235U	± (Ma)	206Pb* 207Pb*	± (Ma)
14DM48-12um-7R <>	525	5252	17.5	21.1135	1.3	0.0454	12.5	0.0069	12.4	0.99	44.6	5.5	45.1	5.5	67.6	31.2
14DM48-12um-2R <>	797	9530	42.0	21.0087	1.1	0.0480	4.2	0.0073	4.1	0.97	47.0	1.9	47.6	2.0	79.4	26.1
14DM48-12um-10R <>	554	41238	35.3	20.3857	1.9	0.0507	10.5	0.0075	10.3	0.98	48.1	4.9	50.2	5.1	150.4	45.2
14DM48-12um-5R <>	1286	8119	41.5	21.1943	1.3	0.0504	2.5	0.0077	2.2	0.85	49.7	1.1	49.9	1.2	58.5	31.5
14DM48-12um-31R <>	2463	24828	42.2	21.2433	0.9	0.0540	2.3	0.0083	2.1	0.92	53.4	1.1	53.4	1.2	53.0	21.1
14DM48-12um-25R <>	263	4958	250.1	20.8519	3.0	0.0581	5.2	0.0088	4.3	0.82	56.4	2.4	57.3	2.9	97.1	70.0
14DM48-12um-6C <>	110	3726	8.0	20.3173	3.5	0.1185	6.9	0.0175	6.0	0.86	111.6	6.6	113.7	7.5	158.3	82.8
14DM48-12um-8C <>	39	1558	3.0	21.0556	3.5	0.1441	11.9	0.0220	11.3	0.95	140.3	15.7	136.7	15.2	74.1	84.3
14DM48-12um-2C <>	270	5704	1.6	17.4593	4.1	0.2261	5.2	0.0286	3.2	0.61	182.0	5.8	207.0	9.8	502.2	91.1
14DM48-12um-31C <>	61	1977	2.4	19.8412	1.5	0.2019	2.2	0.0291	1.6	0.74	184.6	3.0	186.7	3.7	213.5	34.3
14DM48-12um-33C <>	55	2134	2.1	19.8265	3.4	0.2043	3.6	0.0294	1.2	0.35	186.7	2.3	188.8	6.2	215.2	77.9
14DM48-12um-24C <>	48	2262	2.3	19.6990	3.1	0.2073	3.5	0.0296	1.7	0.48	188.1	3.1	191.3	6.1	230.1	71.3
14DM48-12um-4C <>	44	1545	1.8	20.6532	2.3	0.1980	4.1	0.0297	3.4	0.83	188.4	6.3	183.5	6.9	119.8	54.0
14DM48-12um-13C <>	43	2282	2.0	20.2790	4.7	0.2022	4.8	0.0297	1.2	0.24	188.9	2.1	187.0	8.3	162.7	110.0
14DM48-12um-23C <>	32	2096	2.4	19.9104	3.1	0.2061	3.9	0.0298	2.3	0.59	189.0	4.3	190.3	6.7	205.4	72.5
14DM48-12um-22C <>	91	39130	2.8	19.5422	1.9	0.2113	2.1	0.0299	0.9	0.45	190.2	1.7	194.6	3.7	248.6	42.7
14DM48-12um-32C <>	73	1998	4.0	21.0020	2.4	0.1967	4.6	0.0300	3.9	0.86	190.3	7.3	182.4	7.6	80.1	56.0
14DM48-12um-12C <>	79	2957	1.7	20.4102	1.6	0.2028	2.9	0.0300	2.4	0.82	190.7	4.4	187.5	4.9	147.6	38.7
14DM48-12um-7C <>	34	3317	2.4	19.3105	4.6	0.2145	4.7	0.0300	1.3	0.27	190.8	2.5	197.3	8.5	275.9	104.5
14DM48-12um-11C <>	41	1307	2.0	21.5093	2.9	0.1933	3.6	0.0302	2.0	0.57	191.5	3.8	179.4	5.9	23.2	70.5
14DM48-12um-21C <>	56	2723	2.0	20.3239	1.6	0.2047	2.2	0.0302	1.5	0.67	191.6	2.8	189.1	3.8	157.5	37.9
14DM48-12um-9C <>	34	1414	2.6	20.7647	4.3	0.2013	4.6	0.0303	1.7	0.36	192.5	3.1	186.2	7.9	107.1	102.2
14DM48-12um-3C <>	494	17481	1.3	20.0698	0.8	0.2087	2.1	0.0304	1.9	0.92	192.9	3.6	192.5	3.6	186.9	19.4
14DM48-12um-5C <>	444	14953	2.7	20.0282	1.1	0.2093	1.8	0.0304	1.5	0.80	193.1	2.8	193.0	3.2	191.7	25.3
14DM48-12um-20C <>	55	2168	1.7	20.5605	2.7	0.2042	3.3	0.0304	1.9	0.58	193.4	3.6	188.7	5.7	130.4	62.9

Analysis	U	206Pb	U/Th	206Pb* 207Pb*	±	207Pb* 235U*	±	206Pb* 238U	±	error corr.	206Pb* 238U*	±	207Pb* 235U	±	206Pb* 207Pb*	±
	(ppm)	204Pb		(%)	(%)	(%)	(%)		(%)		(Ma)	(Ma)	(Ma)	(Ma)	(Ma)	(Ma)
14DM48-12um-26C >	593	16488	1.0	19.8700	1.3	0.2118	2.7	0.0305	2.4	0.89	193.8	4.6	195.1	4.9	210.1	29.2
14DM48-12um-1R >	101	5191	1.6	19.9958	1.7	0.2106	5.1	0.0305	4.8	0.95	193.9	9.2	194.0	9.0	195.5	38.5
14DM48-12um-19C >	65	2626	2.8	20.1978	2.6	0.2090	2.9	0.0306	1.3	0.45	194.4	2.5	192.7	5.2	172.0	61.5
14DM48-12um-18C >	325	25365	1.7	19.8888	0.5	0.2133	3.0	0.0308	3.0	0.99	195.3	5.7	196.3	5.4	207.9	12.0
14DM48-12um-15C >	180	8934	1.9	19.9520	1.5	0.2128	2.5	0.0308	2.0	0.80	195.5	3.8	195.9	4.4	200.6	34.8
14DM48-12um-17C >	38	1711	2.1	20.3235	2.5	0.2095	4.8	0.0309	4.0	0.85	196.1	7.8	193.1	8.4	157.6	59.2
14DM48-12um-14C >	149	6950	1.1	20.0973	1.2	0.2120	2.0	0.0309	1.6	0.80	196.2	3.2	195.2	3.6	183.7	28.4
14DM48-12um-27C >	30	925	2.2	22.0512	4.3	0.1950	4.5	0.0312	1.3	0.29	197.9	2.6	180.9	7.5	-36.8	105.3
14DM48-12um-25C >	102	3374	5.0	20.4518	2.1	0.2119	3.4	0.0314	2.7	0.80	199.5	5.3	195.2	6.0	142.8	48.3
14DM48-12um-29C >	94	3441	1.4	20.0706	1.2	0.2163	3.5	0.0315	3.3	0.94	199.9	6.4	198.9	6.3	186.8	27.5
14DM48-12um-28C >	580	33392	1.7	19.8975	0.7	0.2211	1.0	0.0319	0.7	0.70	202.5	1.4	202.8	1.8	206.9	16.4
14DM48-12um-1C >	96	3116	1.7	19.8375	1.7	0.2220	3.8	0.0319	3.3	0.89	202.7	6.7	203.6	6.9	214.0	40.3
14DM48-12um-18R >	210	10451	1.4	19.9005	1.1	0.2226	2.3	0.0321	2.1	0.89	203.9	4.2	204.1	4.3	206.6	24.6

### 8.6.3. Sample 26

Analysis	U (ppm)	<sup>206</sup> Pb (204Pb)	U/Th	<sup>206</sup> Pb* (207Pb*)	± (%)	<sup>207</sup> Pb* (235U*)	± (%)	<sup>206</sup> Pb* (238U)	± (%)	error corr.	<sup>206</sup> Pb* (238U*)	± (Ma)	<sup>207</sup> Pb* (235U)	± (Ma)	<sup>206</sup> Pb* (207Pb*)	± (Ma)
<sup>14</sup> DM26-12um-3R >	6161	32009	0.7	20.0385	4.0	0.0688	8.7	0.0100	7.7	0.89	64.1	4.9	67.6	5.7	190.5	92.3
<sup>14</sup> DM26-14R >	1365	75065	8.2	20.6593	4.1	0.0774	7.4	0.0116	6.1	0.83	74.3	4.5	75.7	5.4	119.1	97.4
<sup>14</sup> DM26-12um-10R >	2417	28940	4.6	20.7827	0.6	0.0791	2.4	0.0119	2.3	0.97	76.4	1.8	77.3	1.8	105.0	13.0
<sup>14</sup> DM26-3 >	135	2882	3.7	9.2978	349.7	0.1773	349.7	0.0120	7.3	0.02	76.6	5.6	165.7	594.5	1758.3	959.1
<sup>14</sup> DM26-4R >	1920	66403	23.7	21.0013	4.8	0.0787	4.9	0.0120	0.9	0.17	76.8	0.7	76.9	3.6	80.2	115.0
<sup>14</sup> DM26-2R >	2862	3109	3.2	19.7995	5.0	0.0835	8.2	0.0120	6.5	0.79	76.8	4.9	81.4	6.4	218.4	115.2
<sup>14</sup> DM26-12um-6R >	470	6070	158.6	20.9802	1.5	0.0804	3.3	0.0122	2.9	0.89	78.4	2.3	78.5	2.5	82.6	36.2
<sup>14</sup> DM26-12um-17R >	1481	15482	1.9	21.0136	0.7	0.0803	1.8	0.0122	1.7	0.93	78.4	1.3	78.4	1.4	78.8	16.4
<sup>14</sup> DM26-7R >	833	15296	4.4	21.8552	8.2	0.0773	8.4	0.0123	1.7	0.20	78.5	1.3	75.6	6.1	-15.2	198.2
<sup>14</sup> DM26-12R >	1987	20204	1.9	20.6153	3.9	0.0831	4.2	0.0124	1.6	0.38	79.6	1.3	81.1	3.3	124.1	92.2
<sup>14</sup> DM26-12um-24R >	920	32568	2.7	20.7145	1.4	0.0843	1.9	0.0127	1.3	0.68	81.1	1.0	82.2	1.5	112.8	32.1
<sup>14</sup> DM26-12um-1R2 >	951	15919	4.1	20.5660	1.0	0.0851	3.4	0.0127	3.3	0.96	81.3	2.6	83.0	2.7	129.7	23.7
<sup>14</sup> DM26-5M >	1968	83571	1.7	20.7058	3.5	0.0850	3.9	0.0128	1.8	0.46	81.8	1.5	82.8	3.1	113.8	82.3
<sup>14</sup> DM26-12um-25R >	2320	37730	2.1	20.9842	0.5	0.0871	1.3	0.0133	1.3	0.93	84.9	1.1	84.8	1.1	82.1	12.0
<sup>14</sup> DM26-12um-21R >	961	15644	9.6	19.4322	5.3	0.0950	5.9	0.0134	2.5	0.43	85.7	2.2	92.1	5.2	261.5	122.4
<sup>14</sup> DM26-12um-19R >	944	10651	2.4	20.7981	1.7	0.0910	2.3	0.0137	1.7	0.71	87.9	1.5	88.4	2.0	103.3	39.1
<sup>14</sup> DM26-1R >	454	8436	5.6	24.6029	20.8	0.0788	21.8	0.0141	6.5	0.30	90.0	5.8	77.0	16.2	-309.8	538.4
<sup>14</sup> DM26-19 >	6404	6919	0.5	20.2680	1.6	0.1058	13.9	0.0156	13.8	0.99	99.5	13.7	102.1	13.6	163.9	38.4
<sup>14</sup> DM26-11R >	608	19405	3.0	20.1217	7.1	0.1103	7.8	0.0161	3.3	0.42	103.0	3.3	106.3	7.9	180.9	166.1
<sup>14</sup> DM26-23 >	2086	8027	5.6	19.7389	3.5	0.1856	4.8	0.0266	3.3	0.68	169.1	5.5	172.9	7.6	225.4	81.3
<sup>14</sup> DM26-22 >	127	5836	4.4	21.7025	23.9	0.1743	24.3	0.0274	4.8	0.20	174.4	8.2	163.1	36.7	1.7	582.0
<sup>14</sup> DM26-18 >	693	27428	1.2	20.6585	5.2	0.1841	6.1	0.0276	3.2	0.52	175.4	5.5	171.6	9.6	119.2	122.8
<sup>14</sup> DM26-20 >	152	9163	2.2	22.9472	18.2	0.1699	18.5	0.0283	3.5	0.19	179.7	6.2	159.3	27.3	-134.4	452.7
<sup>14</sup> DM26-14 >	133	6642	2.1	22.0130	24.6	0.1799	27.8	0.0287	13.0	0.47	182.6	23.4	168.0	43.1	-32.6	604.9
<sup>14</sup> DM26-12um-26 >	1455	50568	0.8	19.9309	0.6	0.2003	3.7	0.0289	3.6	0.99	184.0	6.5	185.3	6.2	203.1	14.3
<sup>14</sup> DM26-13 >	180	9233	1.9	21.7712	21.6	0.2014	21.8	0.0318	2.4	0.11	201.8	4.8	186.3	37.1	-5.9	527.5

Analysis	U (ppm)	<sup>206</sup> Pb 204Pb	U/Th	<sup>206</sup> Pb* 207Pb*	± (%)	<sup>207</sup> Pb* 235U*	± (%)	<sup>206</sup> Pb* 238U	± (%)	error corr.	<sup>206</sup> Pb* 238U*	± (Ma)	<sup>207</sup> Pb* 235U	± (Ma)	<sup>206</sup> Pb* 207Pb*	± (Ma)
<sup>14</sup> DM26-12um-9R <>	129	7330	2.0	19.8037	1.9	0.2226	3.4	0.0320	2.8	0.83	202.9	5.7	204.1	6.3	217.8	44.6
<sup>14</sup> DM26-8 <>	106	2618	1.5	24.3137	22.0	0.1824	22.7	0.0322	5.5	0.24	204.1	11.0	170.1	35.6	-279.6	566.1
<sup>14</sup> DM26-9 <>	182	11127	1.5	18.9273	6.5	0.2350	6.6	0.0323	1.3	0.20	204.6	2.7	214.3	12.8	321.7	147.5
<sup>14</sup> DM26-6 <>	194	2637	1.7	19.3051	18.1	0.2316	18.4	0.0324	3.5	0.19	205.7	7.2	211.5	35.2	276.6	416.7
<sup>14</sup> DM26-21 <>	129	10124	1.7	24.8039	19.1	0.1807	19.5	0.0325	3.9	0.20	206.2	8.0	168.7	30.3	-330.6	495.0
<sup>14</sup> DM26-7 <>	212	18853	1.7	18.9153	12.7	0.2372	12.9	0.0325	2.1	0.16	206.4	4.2	216.1	25.1	323.1	290.0
<sup>14</sup> DM26-16 <>	240	21082	1.7	21.1826	8.3	0.2129	8.6	0.0327	2.3	0.26	207.5	4.6	196.0	15.3	59.8	197.7
<sup>14</sup> DM26-24 <>	138	7225	1.9	19.8206	12.3	0.2322	14.1	0.0334	6.8	0.48	211.6	14.1	212.0	27.0	215.9	286.9
<sup>14</sup> DM26-15 <>	378	45925	1.8	20.6326	8.8	0.2250	9.1	0.0337	2.5	0.27	213.4	5.3	206.0	17.0	122.1	207.3
<sup>14</sup> DM26-12um-27 <>	356	16459	1.3	19.5923	0.8	0.2371	2.5	0.0337	2.3	0.94	213.6	4.9	216.0	4.8	242.6	19.1
<sup>14</sup> DM26-12um-20R <>	894	15302	1.9	17.6300	10.3	0.2638	14.8	0.0337	10.6	0.72	213.9	22.3	237.8	31.4	480.7	228.7
<sup>14</sup> DM26-10 <>	715	32436	1.0	19.7638	5.1	0.2355	5.6	0.0338	2.3	0.42	214.0	4.9	214.7	10.8	222.5	117.7
<sup>14</sup> DM26-4 <>	35	2538	1.7	6.8079	193.3	0.7419	193.5	0.0366	9.3	0.05	231.9	21.2	563.5	1187.9	2310.0	99.4
<sup>14</sup> DM26-2 <>	34	2737	3.6	18.3145	118.6	0.3304	118.8	0.0439	6.7	0.06	276.9	18.2	289.9	308.8	395.9	881.1

## 8.6.4. Sample 45

Analysis	U		U/Th	206Pb*		±	207Pb*	±	206Pb*	±	error	206Pb*	±	207Pb*	±	206Pb*	±
	(ppm)	204Pb		(%)	235U*		(%)	238U		(%)	corr.	238U*		(Ma)		(Ma)	
14DM45-R34 <>	587	9967	7.6	21.6943	14.4	0.0759	14.9	0.0119	4.1	0.27		76.5	3.1	74.3	10.7	2.6	347.3
14DM45-23 <>	548	17734	7.5	21.4845	12.3	0.0781	13.3	0.0122	5.2	0.39		78.0	4.0	76.3	9.8	26.0	295.7
14DM45-37 <>	380	19367	7.7	19.7520	10.7	0.0851	13.6	0.0122	8.5	0.62		78.1	6.6	82.9	10.9	223.9	247.0
14DM45-21R <>	772	19116	6.2	21.9817	10.7	0.0766	11.0	0.0122	2.5	0.23		78.2	2.0	74.9	7.9	-29.2	259.9
14DM45-12um-17R <>	416	10342	3.0	20.3926	0.9	0.0826	1.7	0.0122	1.4	0.83		78.3	1.1	80.6	1.3	149.6	22.2
14DM45-35 <>	369	26401	17.4	24.7318	22.6	0.0683	22.8	0.0122	3.0	0.13		78.5	2.4	67.0	14.8	-323.2	585.8
14DM45-24M <>	810	29780	5.2	21.2417	10.4	0.0799	10.5	0.0123	1.8	0.18		78.9	1.4	78.0	7.9	53.1	247.8
14DM45-32 <>	772	13212	8.0	21.1491	1.9	0.0802	2.3	0.0123	1.4	0.61		78.9	1.1	78.4	1.8	63.6	44.3
14DM45-20M <>	535	13904	6.5	19.9869	11.4	0.0850	12.1	0.0123	4.1	0.34		78.9	3.2	82.8	9.6	196.5	265.9
14DM45-29 <>	305	9032	11.6	21.4002	27.7	0.0797	28.1	0.0124	4.7	0.17		79.2	3.7	77.9	21.0	35.3	673.5
14DM45-19M <>	707	22439	5.3	19.9638	4.3	0.0856	4.6	0.0124	1.6	0.36		79.4	1.3	83.4	3.7	199.2	99.7
14DM45-12um-23RR <>	3472	36975	8.2	20.7286	1.1	0.0824	2.3	0.0124	2.1	0.89		79.4	1.6	80.4	1.8	111.2	24.9
14DM45-27 <>	470	18953	3.8	21.0757	9.9	0.0811	10.4	0.0124	3.2	0.31		79.4	2.5	79.2	7.9	71.9	235.4
14DM45-28M <>	563	14405	6.5	21.7910	12.7	0.0784	12.7	0.0124	1.2	0.09		79.4	0.9	76.7	9.4	-8.1	306.7
14DM45-13 <>	784	29189	6.7	21.2345	6.1	0.0806	6.3	0.0124	1.4	0.23		79.5	1.1	78.7	4.8	53.9	146.8
14DM45-2 <>	425	10765	6.7	24.6783	18.0	0.0694	18.2	0.0124	2.4	0.13		79.6	1.9	68.1	12.0	-317.6	465.8
14DM45-33 <>	560	27382	11.0	22.1305	14.8	0.0776	15.0	0.0125	2.7	0.18		79.8	2.1	75.9	11.0	-45.6	361.0
14DM45-22 <>	716	25065	6.6	19.8940	6.5	0.0864	6.8	0.0125	1.8	0.27		79.8	1.4	84.1	5.5	207.3	151.2
14DM45-3 <>	403	25460	8.4	20.5679	18.2	0.0837	18.4	0.0125	2.8	0.15		80.0	2.3	81.6	14.4	129.5	430.1
14DM45-15 <>	238	9206	3.1	24.6762	27.5	0.0699	27.9	0.0125	4.3	0.15		80.2	3.4	68.6	18.5	-317.4	717.5
14DM45-30M <>	448	25975	10.5	24.6363	18.1	0.0701	18.4	0.0125	3.3	0.18		80.2	2.6	68.8	12.2	-313.2	466.0
14DM45-12M <>	768	21960	7.9	21.4209	6.7	0.0806	7.0	0.0125	1.9	0.27		80.2	1.5	78.7	5.3	33.1	161.1
14DM45-11M <>	600	13259	7.1	20.0753	7.1	0.0862	7.5	0.0126	2.4	0.32		80.4	1.9	84.0	6.0	186.2	165.0
14DM45-10M <>	483	13025	7.0	19.8966	9.9	0.0870	10.1	0.0126	1.7	0.17		80.4	1.4	84.7	8.2	207.0	231.0
14DM45-16 <>	579	18491	10.2	20.3988	15.3	0.0849	15.6	0.0126	2.8	0.18		80.5	2.2	82.8	12.4	148.9	360.6
14DM45-4 <>	705	23000	4.9	20.8569	5.8	0.0832	6.0	0.0126	1.3	0.22		80.6	1.0	81.1	4.6	96.6	137.7

Analysis	U (ppm)	<sup>206</sup> Pb 204Pb	U/Th	<sup>206</sup> Pb* 207Pb*	± (%)	<sup>207</sup> Pb* 235U*	± (%)	<sup>206</sup> Pb* 238U	± (%)	error corr.	<sup>206</sup> Pb* 238U*	± (Ma)	<sup>207</sup> Pb* 235U	± (Ma)	<sup>206</sup> Pb* 207Pb*	± (Ma)
14DM45-21 <>	587	37043	13.1	21.1133	9.2	0.0823	9.7	0.0126	3.1	0.32	80.7	2.5	80.3	7.5	67.6	218.6
14DM45-8M <>	647	28280	6.5	21.3264	8.2	0.0814	8.7	0.0126	2.9	0.33	80.7	2.3	79.5	6.7	43.6	197.4
14DM45-6M <>	629	40155	5.0	19.9850	10.5	0.0871	10.6	0.0126	2.0	0.19	80.9	1.6	84.8	8.7	196.8	243.6
14DM45-5M <>	852	27991	3.8	21.4748	6.1	0.0811	6.4	0.0126	2.0	0.31	80.9	1.6	79.2	4.9	27.0	146.1
14DM45-31 <>	434	8482	3.1	20.5238	8.3	0.0849	8.6	0.0126	2.1	0.25	80.9	1.7	82.7	6.8	134.5	195.6
14DM45-36 <>	375	9850	14.0	22.5176	23.0	0.0776	23.3	0.0127	4.0	0.17	81.2	3.2	75.9	17.0	-87.9	568.9
14DM45-18M <>	396	24952	5.5	22.8690	14.0	0.0772	14.8	0.0128	5.0	0.34	82.0	4.1	75.5	10.8	-126.0	346.0
14DM45-9M <>	437	14851	6.5	21.1295	14.3	0.0836	14.4	0.0128	1.6	0.11	82.1	1.3	81.6	11.3	65.8	341.8
14DM45-12um-6R <>	370	5005	8.1	20.7781	2.1	0.0857	2.5	0.0129	1.3	0.53	82.7	1.1	83.5	2.0	105.5	50.0
14DM45-12um-23R <>	2441	68015	7.8	20.7907	0.6	0.0866	2.6	0.0131	2.5	0.97	83.6	2.1	84.3	2.1	104.1	14.7
14DM45-12um-1 <>	175	3150	27.0	20.9034	1.1	0.0862	2.2	0.0131	1.9	0.87	83.7	1.6	83.9	1.8	91.3	25.5
14DM45-12um-1R <>	1372	19449	10.0	20.6829	0.9	0.0876	2.4	0.0131	2.2	0.92	84.1	1.8	85.3	1.9	116.4	22.0
14DM45-12um-3R <>	2753	41705	8.8	20.9311	0.7	0.0866	4.4	0.0131	4.4	0.99	84.2	3.7	84.3	3.6	88.2	17.3
14DM45-14R <>	1130	48183	10.2	21.9749	5.3	0.0830	7.7	0.0132	5.6	0.73	84.7	4.7	81.0	6.0	-28.4	127.6
14DM45-26M <>	954	22174	4.1	21.1003	6.4	0.0868	6.9	0.0133	2.5	0.36	85.1	2.1	84.5	5.6	69.1	153.1
14DM45-15R <>	846	41889	7.8	20.6112	5.4	0.0905	5.7	0.0135	1.9	0.34	86.6	1.7	88.0	4.8	124.6	126.7
14DM45-12um-21R2 <>	283	5563	7.1	20.8940	2.0	0.0905	8.3	0.0137	8.0	0.97	87.8	7.0	88.0	7.0	92.4	47.9
14DM45-12um-4R <>	480	5770	18.8	20.2278	4.7	0.0992	4.9	0.0146	1.6	0.32	93.2	1.4	96.1	4.5	168.6	109.2
14DM45-12 <>	683	6285	12.9	20.0238	11.2	0.1091	11.6	0.0158	3.1	0.26	101.4	3.1	105.2	11.6	192.3	261.3
14DM45-25M <>	419	12607	3.5	22.3232	15.1	0.1017	15.3	0.0165	2.5	0.17	105.3	2.7	98.4	14.3	-66.7	370.0
14DM45-10 <>	104	5721	2.5	27.2858	54.6	0.1146	55.6	0.0227	10.6	0.19	144.5	15.2	110.1	58.1	-582.3	1582.3
14DM45-11 <>	125	2658	2.6	20.9844	24.6	0.1874	25.4	0.0285	6.5	0.26	181.2	11.6	174.4	40.8	82.1	591.2
14DM45-6 <>	480	21468	1.6	20.1920	3.0	0.2014	3.7	0.0295	2.1	0.56	187.4	3.8	186.3	6.3	172.7	71.2
14DM45-5 <>	90	5174	2.2	19.9925	24.2	0.2078	26.0	0.0301	9.6	0.37	191.3	18.1	191.7	45.5	195.9	569.1
14DM45-24 <>	205	15835	1.5	19.9830	11.2	0.2080	12.7	0.0301	6.1	0.48	191.4	11.5	191.8	22.2	197.0	259.8
14DM45-38 <>	1675	35540	0.9	19.4875	3.6	0.2174	8.6	0.0307	7.8	0.91	195.1	15.0	199.8	15.5	255.0	82.0
14DM45-14 <>	483	51143	2.4	21.1283	5.7	0.2011	7.8	0.0308	5.3	0.68	195.7	10.2	186.1	13.3	65.9	136.7
14DM45-20 <>	1894	189847	0.5	19.6200	1.7	0.2186	2.7	0.0311	2.0	0.76	197.4	4.0	200.7	4.9	239.4	40.0



Analysis	U	206Pb	U/Th	206Pb*	±	207Pb*	±	206Pb*	±	error	206Pb*	±	207Pb*	±	206Pb*	±
	(ppm)	204Pb		207Pb*	(%)	235U*	(%)	238U	(%)	corr.	238U*	(Ma)	235U	(Ma)	207Pb*	(Ma)
14DM45-26 <>	1591	18932	0.4	19.7090	1.8	0.2181	4.9	0.0312	4.6	0.93	197.9	9.0	200.3	9.0	228.9	41.0
14DM45-30 <>	60	3445	1.6	24.5886	47.9	0.1792	48.6	0.0320	8.7	0.18	202.8	17.3	167.4	75.2	-308.3	1290.6
14DM45-18 <>	267	27698	1.6	20.5028	7.4	0.2155	7.8	0.0320	2.4	0.31	203.4	4.8	198.2	14.0	137.0	174.2
14DM45-9 <>	171	14671	1.5	19.3892	12.3	0.2337	12.7	0.0329	3.2	0.25	208.5	6.5	213.3	24.5	266.6	284.1
14DM45-17 <>	361	21636	2.2	20.6956	13.1	0.2202	13.2	0.0331	2.0	0.15	209.6	4.0	202.1	24.3	114.9	310.1
14DM45-19 <>	257	16228	1.3	20.5279	9.1	0.2255	9.3	0.0336	1.7	0.18	212.8	3.5	206.4	17.4	134.1	215.2
14DM45-8 <>	138	14067	1.7	18.9293	14.0	0.2484	14.3	0.0341	2.7	0.19	216.2	5.7	225.3	28.8	321.4	319.6
14DM45-28 <>	202	20535	2.2	20.8452	11.8	0.2276	12.1	0.0344	2.7	0.22	218.1	5.8	208.2	22.8	97.9	280.3